

**DETERMINATION OF PROPERTIES OF VISCOELASTIC MATERIALS BY
NANOINDENTATION**

Arkadz Fatseyeu

A Thesis
in
The Department
of
Mechanical and Industrial Engineering

Presented in Partial Fulfilment of the Requirements
for the Degree of Master of Applied Science (Mechanical Engineering) at
Concordia University
Montreal, Quebec, Canada

October 2005

© Arkadz Fatseyeu, 2005



Library and
Archives Canada

Bibliothèque et
Archives Canada

Published Heritage
Branch

Direction du
Patrimoine de l'édition

395 Wellington Street
Ottawa ON K1A 0N4
Canada

395, rue Wellington
Ottawa ON K1A 0N4
Canada

Your file Votre référence

ISBN: 978-0-494-20759-8

Our file Notre référence

ISBN: 978-0-494-20759-8

NOTICE:

The author has granted a non-exclusive license allowing Library and Archives Canada to reproduce, publish, archive, preserve, conserve, communicate to the public by telecommunication or on the Internet, loan, distribute and sell theses worldwide, for commercial or non-commercial purposes, in microform, paper, electronic and/or any other formats.

The author retains copyright ownership and moral rights in this thesis. Neither the thesis nor substantial extracts from it may be printed or otherwise reproduced without the author's permission.

AVIS:

L'auteur a accordé une licence non exclusive permettant à la Bibliothèque et Archives Canada de reproduire, publier, archiver, sauvegarder, conserver, transmettre au public par télécommunication ou par l'Internet, prêter, distribuer et vendre des thèses partout dans le monde, à des fins commerciales ou autres, sur support microforme, papier, électronique et/ou autres formats.

L'auteur conserve la propriété du droit d'auteur et des droits moraux qui protègent cette thèse. Ni la thèse ni des extraits substantiels de celle-ci ne doivent être imprimés ou autrement reproduits sans son autorisation.

In compliance with the Canadian Privacy Act some supporting forms may have been removed from this thesis.

Conformément à la loi canadienne sur la protection de la vie privée, quelques formulaires secondaires ont été enlevés de cette thèse.

While these forms may be included in the document page count, their removal does not represent any loss of content from the thesis.

Bien que ces formulaires aient inclus dans la pagination, il n'y aura aucun contenu manquant.


Canada

ABSTRACT

**DETERMINATION OF PROPERTIES OF VISCOELASTIC MATERIALS BY
NANOINDENTATION.**

Arkadz Fatseyeu.

The purpose of this work was to explore the possibility of measuring properties of viscoelastic materials by nanoindentation. Indentation is not a common method for determining properties of viscoelastic materials and nanoindentation is a very new, state-of-the art technology. Therefore, this research is one of very few works in this area.

This study includes nanoindentation experiments on viscoelastic materials, determining bulk properties of the same materials by conventional rheological techniques, suggesting of physical models to measure properties of viscoelastic solids and viscoelastic liquids by nanoindentation and numerical simulations of the nanoindentation process. The experimental part includes nanoindentation tests of viscoelastic solids and viscoelastic liquids and comparing measured local properties with the bulk ones. The bulk properties were measured with SAOS and Torsion tests. For this investigation polybutadiene was selected as an example of a viscoelastic liquid and silicon cross-linked rubber as a viscoelastic solid. It was found that the local properties of solid polymers vary widely. However, by averaging data collected from various locations, the bulk properties can be determined accurately for the viscoelastic solids.

For the physical modeling we validated the Sneddon & Sakai model of indentation of viscoelastic solids and suggested a model for the indentation of viscoelastic liquids, based on Stoke's theory of a potential flow around a sphere. Also nanoindentation of a viscous liquid was simulated using the FLUENT commercial code. It was found that for the indentation of viscoelastic materials with dominantly viscous properties, the indentation model developed from Stoke's theory gives

realistic values for shear forces, but predicts a smaller than actual compression force, acting on the surface of the indenter.

The comparison of the results of the mentioned above different approaches allowed us to draw conclusions about the advantages and limitation of the technology and theoretical analysis of nanoindentation and its application in rheometry. It was shown that nanoindentation can be successfully used for investigation of viscoelastic materials. Because of its unique abilities nanoindentation will become an irreplaceable tool in such areas as the testing of thin films, study of materials in a transient states, and biomedical research.

However, there are number of technical and theoretical issues that need to be addressed. We outlined issues that need to be resolved and suggested direction for further research and development. Among them are: selection of a proper model to simulate behavior of particular viscoelastic material, further improvement of indentation control and data acquisition system, manufacturing new indenters of optimum shape and material.

DEDICATIONS.

To my Mom and Dad.

ACKNOWLEDGEMENTS

I'd like to express my most sincere gratitude to Dr. Wood-Adams, my advisor, for her guidance, inspiration and irrefutable help with both science and administrative issues. She was also tireless with the numerous revisions of this document.

I would like to thank Dr.Ali Dolatabadi, Dr.Ramin Sedaghati, Dr.John Dealy, my thesis committee members.

I want to acknowledge the Taiho Kogyo Tribology Research Foundation for funding this project.

Finally, I want to thank each and every of colleagues and friends Wang Heng, Chunxia He, Luminita Ionesky, Youri Youriev, Kaveh Mohammed and Shahin Gomeshi for help, shearing their expertise and just for being nice people to work with.

Table of Contents

Abstract.....	iii
Dedication	v
Acknowledgements	vi
Table of Contents	vii
List of Figures.....	xii
List of Tables	xvii
List of Nomenclature	xvii
 CHAPTER 1. Introduction	 1
1.1 Viscoelasticity.....	1
1.2 Objective and Research Methodology.....	3
1.2.1 Experimental part.....	3
1.2.2 Physical modeling.....	4
1.2.3 Numerical Simulation	5
1.3 Results and discussions.....	6
 CHAPTER 2. Theory and background.	 7
2.1 Origin of Traditional Indentation Method.....	7
2.2 Indentation of Viscoelastic Materials.....	9
2.3 Nanoindentation.....	10
2.3.1 Advantages of nanoindentation method.	11
2.3.2 Disadvantages of nanoindentation method.....	11

2.4 Viscoelastic material function.....	12
2.4.1 Harmonic Oscillatory Response.	13
2.5 Rheological models.....	15
2.5.1 Voight model.....	16
2.5.2 Maxwell model.	16
2.5.3 Generalized Maxwell Model	18
2.6 Creep Compliance.....	20
CHAPTER 3. Experimental research	22
3.1 Bulk Rheometry.	22
3.2 Nanoindentation.	24
3.2.1 Instrument.	24
3.2.2 Transducer.....	25
3.2.3 Operation modes.	26
3.3 Contact force microscopy (CFM)	27
3.4 Container for viscoelastic liquids	28
3.5 Indenters	28
3.5.1 Determination of the shape of an indenter	29
3.6 Investigation of polybutadiene: Viscoelastic liquid	34
3.6.1 Polybutadiene chemical structure	34
3.6.2 Physical properties of Polybutadiene	36
3.6.3 Bulk Rheological properties of the Polybutadiene.....	36
3.6.4 Nanoindentation of the Polybutadiene with a spherical indenter	38
3.6.5 Nanoindentation of Polybutadiene with conical indenter	41

3.7. Investigation of cross-linked silicone rubber	47
3.7.1 Sample preparation	48
3.7.2 Torsion tests on the cross-linked silicon rubber.....	49
3.7.3 Temperature effect on material functions	51
3.7.4 Nanoindentation of the silicon rubber	55
3.7.5 Step-stress Creep test.....	55
CHAPTER 4 Physical models for nanoindentation of viscoelastic materials	62
4.1 Stoke's theory of creeping flow.....	62
4.2 Indentation of liquids.....	65
4.1.3. Surface tension force.....	73
4.1.4. Buoyancy force	75
4.2 Stokes theory approach in the modeling of AFM tapping mode.....	75
4.3 Indentation of viscoelastic solids	80
4.4 Combining approaches for viscoelastic	
liquids and viscoelastic solids	82
CHAPTER 5. Numerical simulation of viscous flow around an indenter	83
5.1 Objectives of the numerical simulation.....	83
5.2 Modeling of the Stoke's problem.....	83
5.3 Problem formulation	85
5.4 Modeling of the indentation	93
5.5 Mesh independence.....	97
5.6 Contact Depth during an indentation	98

5.7 Results of modeling	100
CHAPTER 6. Comparison of results and discussion	105
6.1 Introduction	105
6.2 Comparison of theoretical modeling and numerical simulations	105
6.3 Comparison of experimental data with theoretical model	113
6.3.1 Mode based on the Stoke's theory	114
6.3.2 Combined indentation model	115
6.4 Comparison of experiment data for viscoelastic solid with model	117
CHAPTER 7. Conclusions	120
CHAPTER 8. Contributions	122
CHAPTER 9. Future work	124
REFERENCES	128

List of Figures

Fig.1.1 Deformation imposed in step shear strain.	2
Fig.1.2 Behavior of materials under Step strain.	2
Fig. 2.1 Contact depth of an indentation.....	8
Fig. 2.2 Loss and storage modulus.....	14
Fig. 2.3 Voight element.	16
Fig. 2.4 Maxwell element.	16
Fig. 2.5 Response of a Maxwell element to a step-strain	17
Fig. 2.6 Generalized Maxwell model.	18
Fig. 2.7 Spectrum function	20
Fig. 2.8 Creep test	21
Fig. 3.1 Principle of rotational rheometer.	22
Fig. 3.2 Torsion test.....	23
Fig. 3.3 Nanoindentation unit - Hysitron Triboscope , mounted on Multimode AFM platform (model MMAFM-2)	24
Fig. 3.4 Electrostatic Transducer.	25
Fig. 3.5 Contact Force Microscope mode.....	27
Fig. 3.6 Container for liquid materials.....	28
Fig. 3.7 Indenter geometries.....	29
Fig. 3.8 Projected area of an indenter	30
Fig. 3.9 Conical tip, dulled by sphere	31
Fig. 3.10 Triangle Load-Time curve.....	32
Fig. 3.11 depth of indentation vs. indentation load	33

Fig. 3.12 Estimated radius of curvature for a spherical tip	33
Fig. 3.13 Indenter geometry (not to scale)	34
Fig. 3.14 Isomers of Polybutadiene.....	36
Fig.3.15 Bulk Complex viscosity, T=25°C.....	37
Fig.3.16 Relaxation spectrum of the Polybutadiene.....	38
Fig.3.17 Cone-shaped indenter with Spherical tip.....	38
Fig. 3.18 Spherical Indenter, R=8 mm Indentation rate – 4.5 $\mu\text{m/s}$	40
Fig. 3.19 Force vs. time curves for indentation rates 4.5, 2, 1, 0.5 $\mu\text{m/s}$. Polybutadiene	42
Fig. 3.20 Average force responses of polybutadiene for various indentation rates 4.5, 2, 1, 0.5 $\mu\text{m/s}$. Error bars represent standard deviations	43
Fig. 3.21 Superposed load-time data for various indentation rates	45
Fig.3.22 Superposing coefficient vs. Indentation rate.....	45
Fig. 3.23 Indentation of polybutadiene	46
Fig. 3.24 Normalized force for indentation of polybutadiene	47
Fig.3.25 General chemical structure of a silicon Rubber.	48
Fig 3.26 Torsion clamp	49
Fig. 3.27 Strain sweep torsion test at frequency $\omega=10\text{ Hz}$	50
Fig. 3.28 Results of the frequency sweep at 25°C, cross-linked silicone rubber.....	51
Fig. 3.29 Master curves for loss modulus and storage modulus at $T_0=25\text{C}$.....	53
Fig. 3.30 Modulus shift factor (b_T)	54
Fig. 3.31 Time scale shift factor(a_T).....	54
Fig. 3.32 Load-time curve for the creep test.....	55

Fig. 3.33 Series of creep tests at a force of $100\mu\text{N}$	56
Fig. 3.34 Depth-time curves for repeated indentations	57
Fig 3.35 Cone geometry	58
Fig. 3.36 Creep compliance for different step-stress values.....	59
Fig. 3.37 Creep compliance for different indentation force	60
Fig.4.1 Ideal flow around a sphere.	64
Fig. 4.2 Flow around spherical indenter	67
Fig. 4.3 Spherical system of coordinates	68
Fig. 4.4 Indentation geometry	69
Fig. 4.5 Deformation of interface boundary during indentation	72
Fig. 4.6 Surface tension forces.....	74
Fig. 4.7 Portion of the indenter, submerged in a polymer.....	76
Fig. 4.8 Forces in Polybutadiene indentation from Stoke's theory	
$R=8\mu\text{m}$, $V=4.5\mu\text{m/s}$, $\mu=37000\text{ Pa}\cdot\text{s}$.....	77
Fig. 4.9 Taping mode of AFM	78
Fig. 5.1 Model geometry for flow around a sphere	85
Fig. 5.2 Problem set-up for creeping flow around a sphere	86
Fig. 5.3 Velocity magnitude ratio as a function of θ for fixed r/R ratio.....	87
Fig. 5.4 2D problem formulation and boundary conditions in cylindrical	
system of coordinates	89
Fig. 5.5 Velocity magnitude isolines for modeled creeping flow around a sphere.....	87
Fig. 5.6 Velocity vector field for modeled creeping flow around a sphere.....	90

Fig. 5.7 Particles path lines Velocity vector field for modeled creeping

flow around a sphere	90
Fig.5.8 Selected lines for velocity profile comparison.....	91
Fig 5.9 Comparison at 45 degrees.....	91
Fig 5.10 Comparison at 0 degrees.....	91
Fig. 5.12 Vortex formation in an indentation simulation	94
Fig.5.13 Results of simulations: Forces acting on indenter.	
Symbols are results of simulations with air viscosity	
set to 0.001 Pa·s and line those with air viscosity set to 0.01 Pa·s	95
Fig. 5.14 Phase profile at 0.62715 sec of indentation	96
Fig. 5.15 Particle pathlines	96
Fig.5.16 Comparison of simulation results with original and coarsened mesh.	
Symbols represent results from coarse mesh and line represent results	
from fine mesh. $R=8\mu\text{m}$, $V=4.5\mu\text{m/s}$, $\mu=37000\text{ Pa}\cdot\text{s}$	97
Fig.5.17 Interface distortion during indentation.....	98
Fig. 5.18 Contact depth/indentation depth ratio for viscous liquid indentation	101
Fig.5.20 Indentation with parameters: $\mu=3700\text{ Pa}\cdot\text{s}$ $R=8\mu\text{m}$ $V=4.5\mu\text{m/s}$.....	101
Fig.5.21 Indentation with parameters: $\mu=37000\text{ Pa}\cdot\text{s}$ $R=8\mu\text{m}$ $V=2\mu\text{m/s}$.....	102
Fig.5.22 Indentation with parameters: $\mu=37000\text{ Pa}\cdot\text{s}$ $R=20\mu\text{m}$ $V=4.5\mu\text{m/s}$.....	102
Fig. 5.23 Compression force curve for different viscosities.....	103
Fig. 5.24 Shear force change for different viscosities.....	104
Fig. 6.1 Results of physical and numerical modeling of	
a nanoindentation of Newtonian fluid.....	107

Fig. 6.2 Starting position of the indenter for numerical modeling of indentation process.	108
Fig. 6.3 Control point for an indentation with a spherical indenter	107
Fig. 6.4 Velocity at the control point from Stoke's theory and numerical simulation	110
Fig. 6.5 Fictitious sphere.....	111
Fig. 6.6 Velocity at the control point from modified Stoke's approach and numerical simulation.....	111
Fig. 6.7 Deviation in predicted shear force	112
Fig. 6.8 Suggested indenter shape.....	113
Fig. 6.9 Fit of experimental data VS model based on the Stoke's solution for indentation of polybutadiene	115
Fig. 6.10 Fit of experimental and theory predicted forces for indentation of polybutadiene	116
Fig. 6.11 Creep test of indentation of cross-linked silicone rubber with 30μn force .	118
Fig. 6.12 Fitting of experimental data with Voight element model	119
Fig. 9.1 Combined a linear and a harmonic load function.....	126
Fig. 9.2 Elongation flow test	127

List of Tables

Table 3-1 Container specs.....	28
Table 4-1 Experimental materials	35
Table 5-1 Parameters for simulation.....	92

List of Nomenclature

A	area
a_T	time scale shift factor
b_T	modulus shift factor.
D	tensile compliance
C, n	coefficients, depending on the geometry of the indenter
E	tensile modulus
E_a	activation energy (J/mol)
F	force
G	shear modulus.
G'	storage modulus
G''	loss modulus
H	spectrum function
h	indentation depth
J	shear compliance
P	load
R	tip radius
Re	Reynolds number
t	time
V_{IND}	indentation velocity
α, β	angles
ε	tensile strain
ν	Poisson's ratio
η	viscosity
γ	shear strain
η	complex viscosity
γ	surface energy
ρ	density
λ	relaxation time
τ	retardation time
σ	stress
v	velocity
θ	angle from the z-axis
ω	frequency

1. Introduction

The purpose of this work is to investigate the possibility of determining the material functions of viscoelastic materials by nanoindentation. Nanoindentation is a modern state-of-the art testing technique that has been developed from the traditional indentation techniques in the last decade. By definition, the nanoindentation test assumes the use of indenters of a very small size. The use of these small sized indenters requires one to overcome a number of technical difficulties and continued scientific research is necessary. Because of this, nanoindentation has remained a qualitative method up until only a few years ago. Therefore, the Hysitron Triboscope, the nanoindentation unit used in this work, is one of the first experimental units suitable for quantitative measurements. Until now the area of its application has lied mostly in the area of testing solid materials with a relatively high modulus.

1.1 Viscoelasticity.

Our research focuses on the application of nanoindentation for the measurement of properties of both viscoelastic liquids and solids that may have complex properties. The concept of viscoelasticity can be demonstrated by a simple example. If a sample of a material is subjected to step shear strain (Figure 1.1), the mechanical response of this material depends on its properties (Figure 1.2).

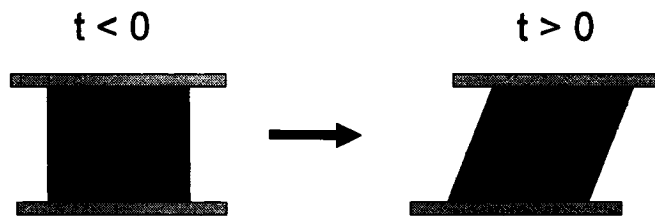


Fig.1.1 Deformation imposed in step shear strain.

Such, a Newtonian fluid will have a short stress spike which relaxes when the plate stops moving, a simple elastic material will hold a constant stress as long as the strain is maintained. Viscoelastic liquids hold stress for a more or less long period of time but eventually relax completely. In the case of viscoelastic solids the stress reduces to a non-zero value which is held infinitely.

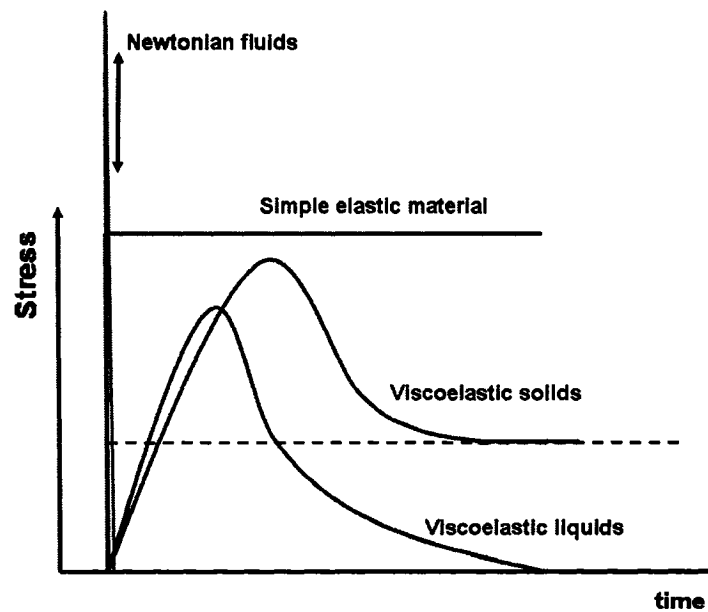


Fig.1.2 Behavior of materials under Step strain.

1.2 Objective and Research Methodology.

The goal of our work is to develop methods to measure rheological properties of viscoelastic materials using nanoindentation. In order to reach this goal we conducted experimental research using nanoindentation and conventional rheological measurement techniques, suggested physical models of indentation for viscoelastic liquids and solids and performed numerical simulation of indentation. Therefore, the research consists of three related parts: the experimental part, physical modeling, and numerical simulations. In the following sections we introduce these parts and summarize the organization of this thesis.

1.2.1 Experimental part.

Tests were conducted on a viscoelastic solid and a viscoelastic liquid. The first step was to choose appropriate materials for the investigation. Ideal materials should possess distinct viscoelastic liquid and viscoelastic solid properties under normal conditions, be amorphous, stable without significant aging or deterioration, and non-wetting towards the material of the indenter. Based on these requirements, two materials were selected: polybutadiene, which is a viscoelastic liquid and a cross-linked silicon rubber, which is a viscoelastic solid. Bulk mechanical properties of the viscoelastic materials were measured by conventional rheometry techniques and DMA torsion tests. After that, local properties were investigated by nanoindentation. Nanoindentation tests included closed loop controlled force and control rate indentations. This part of the work is described in Chapter 3.

1.2.2 Physical modeling.

The theoretical part is devoted to formulating a physical model of nanoindentation. Formulation of a physical model is an essential step toward the understanding of the real physical process. A physical model allows us to predict behavior of the investigated material under various conditions. In addition, it makes it possible to solve the “reverse problem” – by proper selection of parameters of the model, one can fit the experimental data, then for an accurate model these parameters are in accordance with actual physical properties of the investigated material. In the case of the nanoindentation of viscoelastic materials, the creation of such a model is especially challenging because the different physical behavior of viscoelastic solids and viscoelastic liquids require that different physical phenomena are considered.

In some recent works the model of the indentation of viscoelastic solids it has applied to and experimentally tested on some materials by Sakai et. al [1-6]. Theoretical background was formulated by Sneddon[7,10] and Ting[13]. These models consider only the compression (normal to the surface of the indenter) force, since they were based on the work of Hertz and Love on the indentation of elastic solids¹ and do not consider the possibility of flow of the tested material.

For viscoelastic liquids, various forces acting on the indenter during indentation need to be considered. These forces include: shear forces, compression forces, surface tension and buoyancy. The expressions for shear and compression forces as a function of time or a depth for the constant rate indentation were derived from Stoke’s theory of the

¹ *The solution for indentation of elastic solid materials with a spherical indenter was obtained by H.R.Hertz in 1889 (History of the Theory of Elasticity, 2, 237, Cambridge University Press, 1893) and the solution for indentation with a conical indenter was obtained by A.E.Love in 1939 (Quart. J. Math 10, 161, 1939).*

Creeping Flow around a sphere. For viscoelastic liquids such as polybutadiene, we combine those two approaches and estimate normal forces based on the Sakai's expressions and shear forces based on the Stoke's flow theory. This part of the work is described in Chapter 4.

1.2.3 Numerical Simulation.

In parallel with experiment, the process of indentation in a Newtonian liquid was modeled numerically using the commercial software FLUENT, which applies the finite volume method. Despite the fact that numerical simulation does not offer a simple equation that describes a physical process, has the potential to be an accurate representation of a real process. Also it allows us to conduct numerical experiments for conditions beyond the range of available experiment settings. In our case it can be for indentation with indenters of special shape and various indentation rates. A significant benefit of the numerical model is that it shows behavior of the tested material in an extended region, while the above mentioned physical models focus on the processes in close proximity to the surface of the indenter.

The first step was the proper problem formulation. At this step the geometry of problem, meshing and boundary conditions were set up using the commercial mesh generator Gambit. Next, steady Stoke's flow around a fully submerged sphere was modeled. Similarity of the results of this simulation with the analytical solution for ideal creeping flow validated the problem set up and showed similarity of this flow to the ideal one. Lastly, dynamic indentation was simulated using two-phase unsteady flow model. One phase had properties of the tested material and another represented the ambient air.

Since the hardness of the diamond indenter is much higher than the hardness of the tested material, it was considered to be an impenetrable boundary rather than by introduction of the third phase. This part of the work is described in the Chapter 5.

1.3 Results and discussions.

In Chapter 6 results of different approaches to the solution are discussed. Suggested techniques for the determination of material functions by nanoindentation test are developed and possible modifications to the nanoindentation unit to create a more suitable configuration for the investigation of viscoelastic materials are proposed.

2. Theory and background.

Nanoindentation is one of the most recent techniques for material testing, the full potential of which has yet to be realized. Developed from traditional indentation, there have been two significant advances: small (nanoscale) size of indenters and computer-based data acquisition and control systems. These developments broaden prospective applications in addition to providing the possibility of measuring local steady-state and transient properties.

Although applied mostly in the study of solid materials, the nanoindentation method has high potential in testing other types of materials including both solid and liquid polymers with complex viscoelastic properties. In this work we try to develop this potential. Numerical simulation of nanoindentation, perfection of experimental techniques and correct interpretation of experimental are still challenging and there is significant scientific interest in measuring local viscoelastic properties of materials.

2.1 Origin of Traditional Indentation Method.

The idea of testing materials by indentation was first suggested by Hertz in 1881. For plastic materials he proposed to find hardness from the shape of the indenter, the load and the area of the imprint. Though not all of his ideas were implemented directly, the principle of testing solid materials by indenting with a specially shaped indenter, made of a much harder material, was applied and further developed.

Brinelle suggested in 1900 a method of determining the hardness of solid bodies after

indentation with a spherical indenter, from the load and projected area. In 1909 Meyer confirmed that it is valid to relate a load to a *projected area* of the imprint rather than the whole area of imprint. He also showed that for most symmetric indenters, test results can be normalized by using only two geometrical coefficients - g and γ :

$$\bar{\sigma} = \frac{P\gamma^2}{gh^2} \quad (2.1)$$

where:

$\bar{\sigma}$ is averaged stress, Pa

h the depth of indentation, m

γ is a factor which relates the total penetration depth (h) to the contact depth (h_c)

g is a geometrical factor which relates the total penetration depth (h) to projected area of indentation (A), $A = gh_c^2$ (m²), where h_c – contact depth of indentation (see Figure 2.1).

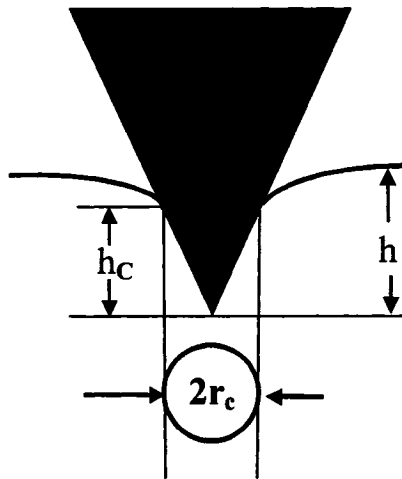


Fig. 2.1 Contact depth of an indentation

Two standard shapes of indenters used in this research – spherical and pyramidal were suggested by Brinelle and Berkovich in the beginning of the last century. We can say that by the 1950's the traditional indentation test techniques were established and basic indenters were classified by shape and type of material. Standard indenters include the Brinelle (spherically shaped indenter), the Vickers, the Knoop (four edge symmetric pyramids), and the Berkovich (trigonal pyramid with an inclined face angle 24.7 degrees).

2.2 Indentation of Viscoelastic Materials.

Radok [9,11] produced another noticeable development in this area between 1947-1960. He suggested the governing equations for the indentation of solid viscoelastic materials. In his approach for viscoelastic materials, the relaxation modulus, $E(t)$ is used instead of Young's modulus E . However, in the case of indentation we deal with a complex deformation, where material under indenter experiences influence of the material around it, therefore, one can observe higher effective modulus, which is related to the material properties through the Poisson ratio (ν):

$$E_{eff} = \frac{E}{1 - \nu^2} \quad (2.2)$$

For incompressible materials $\nu=0.5$.

At each moment of indentation, the stress increment $d\bar{\sigma}(t)$ depends on the history of deformation by using the relaxation modulus at the time t by using the time t' when the displacement $d\bar{\varepsilon}$ occurred.

$$d\bar{\sigma}(t) = \frac{E(t-t')}{1-\nu^2} d\bar{\epsilon}(t') \quad (2.3)$$

where $d\bar{\epsilon}(t)$ is an infinitesimal strain. When indentation is conducted with a constant speed v_{ind} , the indentation force $P(t)$ can be expressed in terms of time and indentation speed.

$$P(t) = Cn v_{ind} \int_0^t E(t-t')(t')^{n-1} dt' \quad (2.4)$$

where C, n are coefficients that depend on geometry of an indenter.

Sakai et. al [1-6] were one of the first researchers who conducted extensive experimental research and applied this theory in practice.

2.3 Nanoindentation.

The latest significant step in the development of the indentation technique was made by the introduction of nano-scale indenters, combined with computer-based control and data acquisition. Nanoindenters ultimately are the smallest indentation probes available today. Possible benefits of this approach are impressive such as small indenter driving force, which removes need for a slow and bulky hydraulic press, measuring local properties or testing small-sized objects, measuring properties of powders, coatings, even living cells or high speed indentation for investigating materials in the transient state.

2.3.1 Advantages of nanoindentation method.

The use of a computer for control and data acquisition allows us to conduct dynamic indentation tests, in addition to immediate application of complex mathematical apparatus for the interpretation of obtained experimental data. It brings nanoindentation to a qualitatively new level. Nanoindentation offers a number of advantages over traditional rheological measurement techniques: it takes much shorter time compared to some traditional rheological tests, it can be done on very small samples, and it is not very sensitive to sample shape. Also it allows us to measure local properties and, therefore, detect property variations and structural features.

2.3.2 Disadvantages of nanoindentation method.

Such small size of parts and applied forces make the nanoindentation technique extremely susceptible to various physical phenomena that do not have much impact on traditional macro-scale indentation. For instance surface forces, electrostatic, magnetic and Van-der-Vaals interactions, condensation of the atmospheric moisture and surface contamination of any kind can influence the measurement results. Also nanoindentation is sensitive to mechanical vibrations including acoustic noises.

Those technical problems were so overwhelming that for almost a decade nanoindentation was only applicable for qualitative measurements and relative comparison. From the mid 1990's nanoindentation technology progressed enough for quantitative measurements. Now nanoindentation tools are manufactured commercially. However, so far reliable

results are achieved only for measuring of mechanical properties of solid bodies. Also when indentation is applied on a polymer, the size of the indent will be comparable with the size of long-chain polymer molecules, therefore a large difference between local and bulk properties can be observed. Also, interpretation of the indentation tests imposes a scientific challenge because of the complex three-dimensional deformation. Only recently a number of paper has been published on application of nanoindentation and AFM(Atomic force Microscopy) for measuring of properties of viscoelastic materials. The most perspective directions in application of nanoindentation are: measuring properties of viscoelastic materials [21], particularly melt polymers[20],[22],[30], investigation of thin films [28], and perspectives for applications of method in medical studies.

2.4 Viscoelastic material function.

By definition, viscoelastic materials exhibit both viscous and elastic properties. In this class, materials vary from *viscous solids*, such as cross-linked rubber, which are more elastic than viscous, to *elastic liquids*, such as molten polymers and polymer solutions, which are more viscous than elastic. To understand the viscoelastic mechanical behavior of these materials requires an extensive set of parameters. Those parameters are called ***Material Functions***. Primary material functions relate stress and strain rate responses of a material in specific flows or deformations.

2.4.1 Harmonic Oscillatory Response.

The SAOS technique theory presented here is a compilation of the following books: Melt Rheology and its role in plastics processing by J.M.Dealy[41], Engineering rheology[40] by T.I.Roger, Understanding Rheology by F.Morrison[39].

SAOS (Small Amplitude Oscillatory Shear) is one of the most common testing procedures which involves subjecting the material to a harmonic shear strain. This principle lays in the basis of various rheometers and DMA (Dynamic Mechanical Analyzers) units. Shearing strain is given by a *sine* function of time:

$$\gamma(t) = \gamma_0 \sin(\omega t) \quad (2.5)$$

where γ_0 is the strain amplitude and ω is the frequency. Also by simple differentiation, we find the shear rate as function of time:

$$\dot{\gamma}(t) = \gamma_0 \omega \cos(\omega t) = \dot{\gamma}_0 \cos(\omega t) \quad (2.6)$$

where $\dot{\gamma}_0$ is the shear rate amplitude.

Then stress is also a sine function of time and has the same frequency as the strain:

$$\sigma(t) = \sigma_0 \sin(\omega t + \delta) \quad (2.7)$$

where σ_0 is stress amplitude and δ - is the phase shift.

If the material is purely elastic, the shear stress will be in-phase with the shear strain and $\delta = 0$:

$$\sigma(t) = \sigma_0 \sin(\omega t) \quad (2.8)$$

At the same time, for a purely viscous fluid the stress will be proportional to the strain rate:

$$\sigma(t) = \sigma_0 \cos(\omega t) = \sigma_0 \sin(\omega t + 90^\circ) \quad (2.9)$$

For viscoelastic materials, the phase shift will be in between 0° and 90° . Therefore, the ratio between elastic and viscous properties can be characterized by the angle of the phase shift δ . Following the same idea, the total stress can be split in two components - σ' and σ'' , where $\sigma' = \sigma_0 \cdot \cos \delta$ represents the elastic component and $\sigma'' = \sigma_0 \cdot \sin \delta$ – the viscous one.

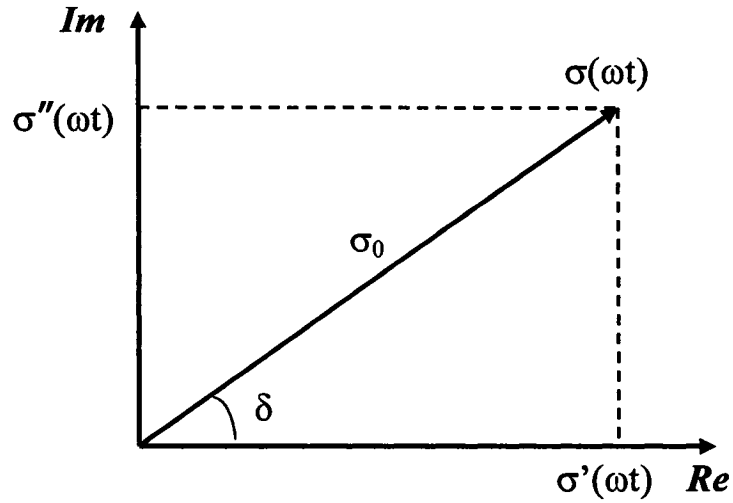


Fig. 2.2 Loss and storage modulus.

Several important material functions can be defined from the relations between σ' and σ'' . Probably the most commonly used of them are the **Storage modulus** (G') and the **Loss modulus** (G''). The **Storage modulus** (G') represents the elastic characteristic

of the material. It is related to the "in-phase" component σ' and indicates the amount of the elastic energy, stored during deformation which can be recovered.

$$G' = \frac{\sigma'}{\gamma_0} = \frac{\sigma_0 (\cos \delta)}{\gamma_0} \quad (2.10)$$

The Loss modulus (G''), represents the viscous characteristic, and is related to the dissipated viscous energy.

$$G'' = \frac{\sigma''}{\gamma_0} = \frac{\sigma_0 (\sin \delta)}{\gamma_0} \quad (2.11)$$

Accordingly, for a viscous material the Storage modulus $G' = 0$ and for a purely elastic solid material the Loss modulus $G'' = 0$. For viscoelastic materials, both G' and G'' are nonzero.

2.5 Rheological models.

Because of the large variety of rheological materials and the extremely wide range of properties they exhibit, there is no a general theory that would be able to explain viscoelastic behavior of all materials. Selected models are applied to particular cases. One of the traditional approaches is to simulate viscoelastic behavior by employing more or less complex mechanistic models. Mechanistic models can be formulated by combining a number of springs and dashpots. One of such models is the Voight model.

2.5.1 Voight model.

The Voight mode is based on a Voight element (Figure 2.2), which contains a spring and a dashpot, connected in parallel. This model can be used to simulate behavior of viscoelastic solids, that after a deformation under a stress, completely restore their shape once the stress is removed.

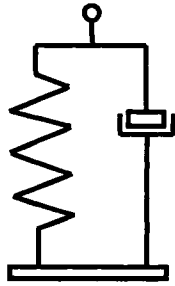


Fig. 2.3 Voight element.

2.5.2 Maxwell model.

One of the most popular mechanistic models applicable for modeling of viscoelastic liquids is the Maxwell model. The base of the Maxwell is a single Maxwell element. It consists of one spring and one dashpot, connected in series.



Fig.2.4 Maxwell element.

This model can be used to simulate the behavior of some viscoelastic liquids. The spring represents the elastic properties and the dash pot – the viscous ones. It is interesting to see

the response to a shear step-strain. The model predicts an exponential decrease of the stress down to zero.

When Maxwell element is subjected to a step-strain, the stress decreases exponentially:

$$\sigma(t) = \sigma_0 \cdot \exp(-t / \lambda) \quad (2.12)$$

where (λ) is relaxation time, time which takes for a viscoelastic liquid to relax down to 37% (e^{-1}) of it's initial value (see Figure 2.4). Or:

$$\sigma(t) = \gamma_0 G(t) \quad (2.13)$$

where the function $G(t)$ is called *shear relaxation modulus*. For a simple Maxwell viscoelastic material shear relaxation modulus under step-strain decays exponentially from it's maximal initial value G_0 .

$$G(t) = G_0 [\exp(-t / \lambda)] \quad (2.14)$$

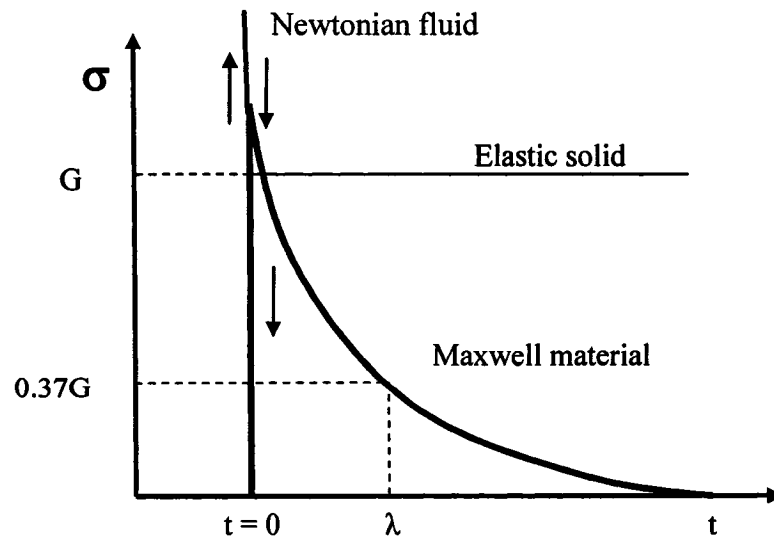


Fig. 2.5 Response of a Maxwell element to a step-strain.

Similarly for a viscoelastic material we also can define the tensile relaxation. The tensile modulus $E(t)$ and the shear modulus $G(t)$ are related through Poisson's ratio:

$$E(t) = 2(1 + \nu)G(t) \quad (2.15)$$

For a Newtonian fluid $E=0$, for an elastic solid $E=\text{constant}$. For Maxwell materials, whose behavior can be modeled by a single Maxwell element, modulus $E(t)$ is:

$$E(t) = E_0 \exp\left(-\frac{t}{\lambda}\right) \quad (2.16)$$

for viscoelastic liquids, and

$$E(t) = E_0 \exp\left(-\frac{t}{\lambda}\right) + E_e \quad (2.17)$$

for viscoelastic solids. The practical application of those relations for the modeling in investigation of viscoelastic materials will be considered in more detail in Chapter 4.

2.5.3 Generalized Maxwell Model.

One of the most useful models for viscoelastic fluids is the generalized Maxwell model. This model can be made to fit data for many real fluids if a suitable distribution of relaxation times is used. The generalized Maxwell model is a parallel arrangement of many Maxwell elements, each with a different spring and dash pot.

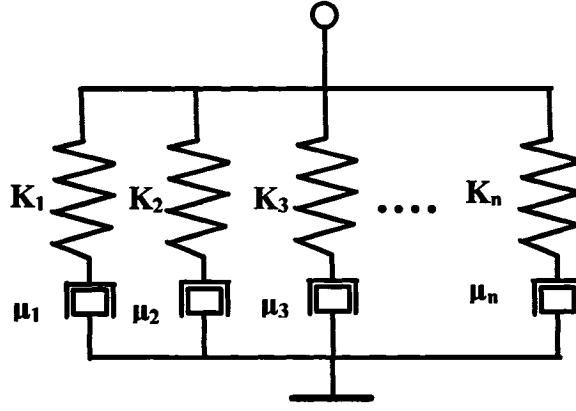


Fig. 2.6 Generalized Maxwell model.

The, response of most materials to step-strain can be described by the generalized Maxwell models with a large enough number of elements. It implies that instead of a single relaxation time, viscoelastic materials have a whole series or distribution of relaxation times. For the generalized Maxwell model, which consists of (N) Maxwell elements, the relaxation modulus is:

$$G(t) = \sum_{i=1}^N G_i [\exp(-t / \lambda_i)] \quad (2.18)$$

In mathematical modeling of material behavior sometimes it is beneficial to use the idea of a generalized Maxwell model with infinite number of elements, which creates continuous relaxation spectrum. Then relaxation modulus can be defined by a function $F(\lambda)$. In this case, instead of a single relaxation time we have a continuous distribution of relaxation times, called relaxation spectrum.

$$G(t) = \int_0^{\infty} F(\lambda) [\exp(-t/\lambda)] d\lambda \quad (2.19)$$

Since in rheology normally all data are plotted in log-log scale, instead of $F(\lambda)$ the spectrum function $H(\lambda)$ (see Figure 2.6) such that $H d(\ln \lambda) = F(\lambda) d\lambda$ is used.

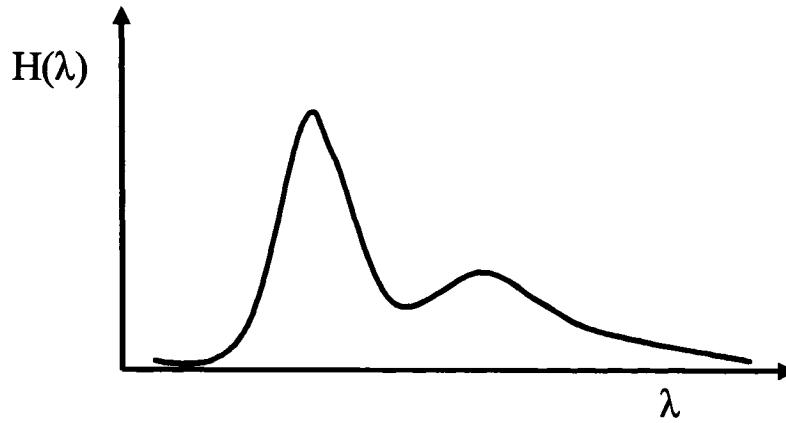


Fig. 2.7 Sketch of a typical spectrum function.

By using the spectrum function we can express the relaxation modulus as:

$$G(t) = \int_{-\infty}^{\infty} H(\lambda) [\exp(-t/\lambda)] d(\ln \lambda) \quad (2.20)$$

The relaxation spectrum function can be found from experimental data. From known relaxation spectrum many material functions of a viscoelastic material can be predicted.

2.6 Creep Compliance.

Creep compliance shows the response of a tested material to an instantaneous step stress with magnitude σ_0 at time t_0 .

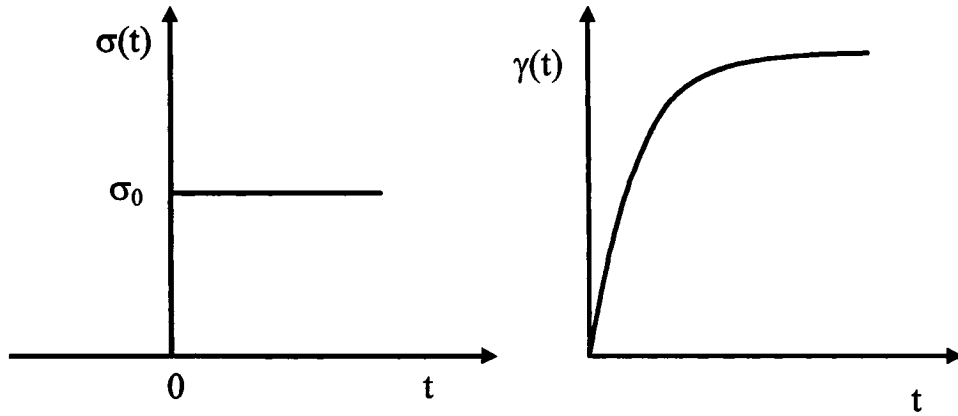


Fig. 2.8 Creep test.

In this case, deformation (strain) of the material is a unique function of time (figure 2.7).

$$\gamma(t) = \sigma_0 \cdot J(t) \quad (2.21)$$

where the function $J(t)$ is called the *Creep compliance*. Or, by rearranging Equation 2.19 the Creep compliance is:

$$J(t) = \frac{\gamma(t)}{\sigma_0} \quad (2.22)$$

The creep compliance is one of the important material functions, necessary to define the behavior of complex viscoelastic materials adequately.

We can summarize that for determining the properties of viscoelastic materials, the most significant characteristics is the time function of response to imposed stresses or strains. Suitable tests can be: oscillatory response, creep stress relaxation, among others.

Chapter 3

Experimental research.

The objective of the experimental part of this research is to measure the mechanical properties of the viscoelastic materials by nanoindentation and to compare them with the properties measured by traditional methods. Also the difference between local properties and bulk properties are of particular interest. Viscoelastic liquids are represented by a polybutadiene and viscoelastic solids by a cross-linked silicon rubber.

3.1 Bulk Rheometry.

Bulk rheometry is the measurement of mechanical properties of material on a large scale. In this work the bulk rheometry was done with a MCR-500 rotational rheometer. The MCR-500 rotational rheometer, manufactured by Physica Co. of Anton Paar is a reliable instrument for basic rheological measurements. With liquid samples the instrument is used in parallel plate configuration (Figure 3.1).

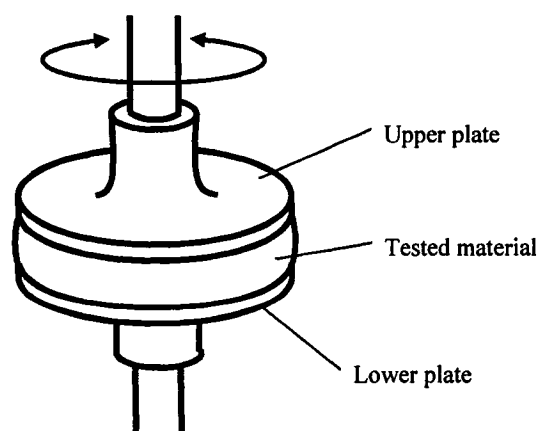


Fig. 3.1 Principle of rotational rheometer.

The rheometer is equipped with an STD-600 Thermo Chamber. The Thermo Chamber is designed to control the test temperatures up to +600°C and to protect the tested sample from harmful environmental conditions [76]. With the MCR-500 rotational rheometer, oscillatory, steady shear, creep and stress relaxation tests can be performed.

The aforementioned tests and rheometer configuration have been developed for viscoelastic liquids, such as molten polymers. It is not possible to characterize a solid material in the plate-plate configuration because of the slip and normal stress effects. Instead the MCR-500 rotational rheometer was adapted to perform torsion (Figure 3.2) tests on solid samples by installing specially designed clamps. Maximum dimensions for samples are: Length: 120mm Width: 15mm Thickness: 4mm. In this work we used the following sample dimensions: 30x11x4 mm

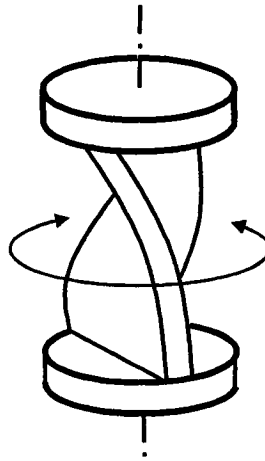


Fig. 3.2 Torsion test.

3.2 Nanoindentation.

3.2.1 Instrument.

Nanoindentation is one of the most recently developed testing techniques. Up until only a few years ago it remained as a qualitative technique. The Hysitron Triboscope is one of the first nanoindentation test units on the market designed for quantitative measurements. The most important parameters are of the indentation force and the measurement of displacement.

Instead of the bulky hydraulic press, typical for conventional indentations, nanoindentation units use other technological means to create the indentation force. Over the last decade various approaches were suggested. Different nanoindentation units have employed mechanical, piezoelectric, electromagnetic and electrostatic forces to produce an indentation load. The electrostatic principle, which was found to be the most promising, is used in the Hysitron Triboscope (Figure 3.3).

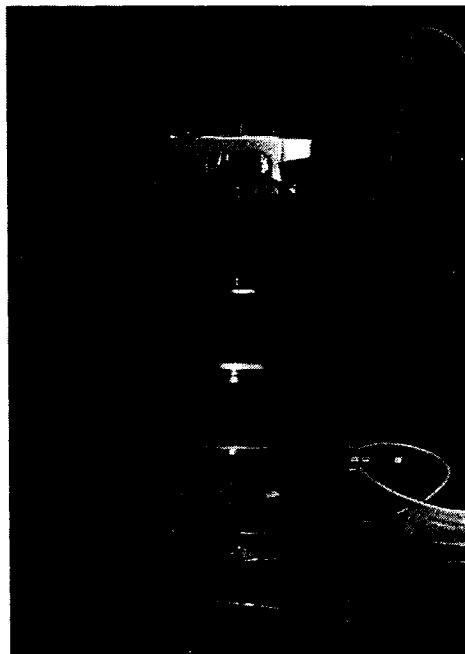


Fig. 3.3 Nanoindentation unit - Hysitron Triboscope , mounted on Multimode AFM platform (model MMAFM-2)

3.2.2 Transducer.

The indentation force builds up in the electrostatic transducer, which is a three plate electrical capacitor [64], [77]. Two outer plates are fixed and the middle one is suspended by flexible membrane. The indenter fixture is attached to the center of the moving plate. This configuration forms two capacitors – one between the top plate and the middle plate and another between the middle plate and the lower plate.

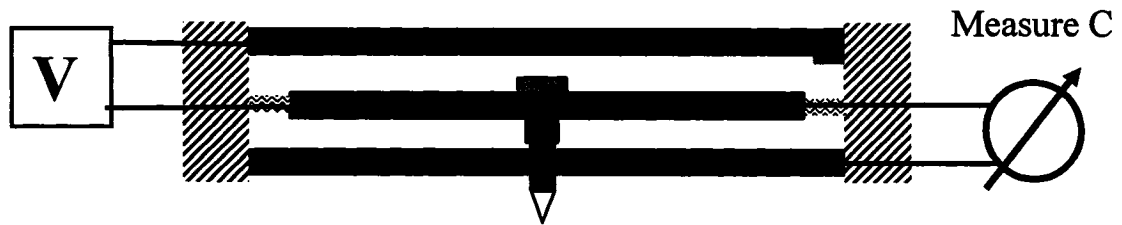


Fig. 3.4 Electrostatic Transducer.

When the voltage (V) is applied between the lower and the center plates, the center plate is moved down by the electrostatic attraction force and this motion is transferred to the indenter. At the same time, the control system measures the capacitance between the top and the center plates, giving the displacement of the center plate.

The capacitance of a parallel plate capacitor, is proportional to the area of these plates and inversely proportional to the distance between them: $C \propto A/d$. In our case the area of the transducer plates is constant, only the distance between top and center plates increases proportionally to the depth of indentation. Therefore, the depth of the indentation is inversely proportional to the measured capacitance: $h \propto 1/C$. This principle allows simultaneous control of the indentation force and measurement of the

displacement. This design offers easy control, accurate displacement measurement, and acceptable time drift and temperature dependency.

3.2.3 Operation modes.

In order to understand how the transducer functions, we consider a force balance. The indentation load which is applied to the sample is the resulting force of the electrostatic force and the spring force of the elastic membrane.

$$F_{INDENTATION} = F_{ELECTROSTATIC} - F_{SPRING} \quad (3.1)$$

The electrostatic force is proportional to the voltage (V), applied to the transducer and the spring force is proportional to the vertical displacement (X) by Hooke's law:

$$F_{INDENTATION} = K_1 V - K_2 X \quad (3.2)$$

As shown in the above equations, the flexible membrane deforms during indentations, creating the spring force directed against the driving electrostatic force. If the instrument is operated in the open loop mode, after proper calibration, the elastic force can be accounted for, but not compensated. Hence, for soft materials, when even a small load can result in a deep indentation, the influence of the resisting spring force makes it practically impossible to set up the desired load curve. Therefore, the open loop mode is suitable only for relatively hard materials, where displacement (X) is very small.

The instrument can also be operated in closed loop mode offering more control over the indentation process. In the closed loop mode a feedback controller compensates for the spring force. In this mode special types of indentation tests are available:

- controlled force indentation: force is set as a function of time and the spring force is compensated.
- controlled displacement: depth of the indentation is set as a function of time.

3.3 Contact force microscopy (CFM).

One of the advanced features of the Hysitron Triboscope is the scanning mode. In the scanning mode the force applied on the indenter is kept to a minimum (Contact force) such that the indenter does not penetrate the sample body, but instead slides on the sample surface. The sample can be moved in the X-Y directions with the piezoelectric scanner of the atomic force microscope (AFM). By using the AFM software the 3D topography of the sample surface can be recovered. This feature is used to check the surface quality and to choose a proper location for indentation. This also allows one to scan the surface and image existing indents in great detail.

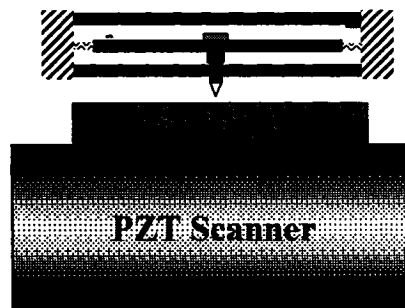


Fig. 3.5 Contact Force Microscope mode.

3.4 Container for viscoelastic liquids.

At room temperature polybutadiene is in the liquid state, therefore it is placed in a specially designed container. The container is made of magnetic iron and is held on the scanner by magnetic force. A schematics of the container is shown below.

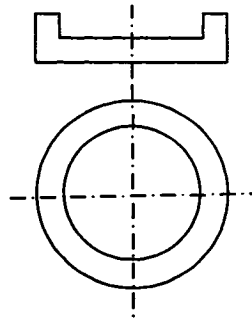


Table 3-1 Container specs.

Diameter	8 mm
Height	2 mm
Depth of machining	1 mm
Wall thickness	1 mm

Fig. 3.6 Container for liquid materials.

3.5 Indenters.

Various indenters, including most of the standard ones: Brinelle, Berkovich, Vickers and Knoop are manufactured by Hysitron Inc. in micro- and nanoscopical sizes. Usually indenters are manufactured from the hardest materials. The traditional material for indenters is polished diamond.

Three indenters were used in this research:

- (1) Conical indenter $\alpha = 90$ degrees, tip radius $R = 426$ nm.
- (2) Conical indenter $\alpha = 90$ degrees, tip radius $R = 8$ μ m.
- (3) Pyramidal Berkovich indenter $\beta = 22.4$ degrees, tip radius $R = 20$ nm.

See Figure 3.7 for indenter geometries.

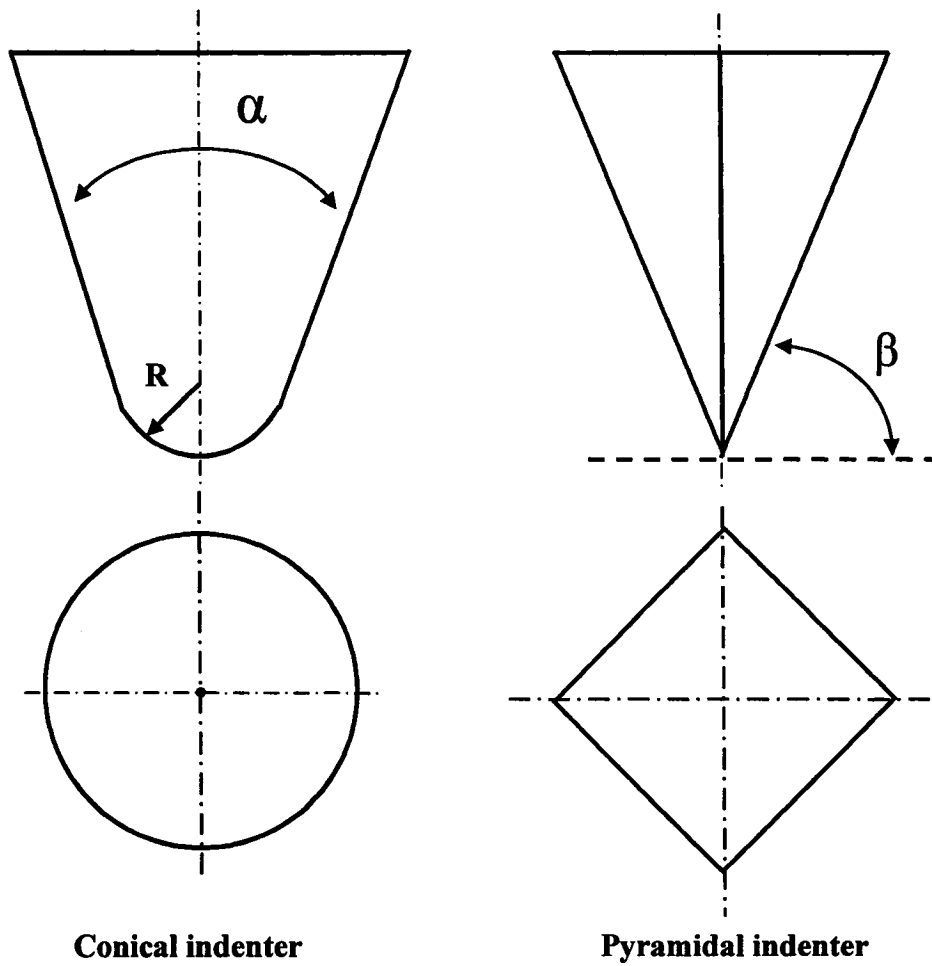


Fig. 3.7 Indenter geometries.

3.5.1 Determination of the shape of an indenter.

In traditional indentation the main measured parameter is the size of the indentation imprint, made with a known indentation force. For nanoindentation to measure the exact size of the imprint would be extremely difficult even on a plastic material and impossible on a viscoelastic one. Instead, the two experimental parameters are the current indentation force and the current depth of the indentation. In order to

determine the shape of an imprint from the depth of an indent, one needs to know precisely the shape of the indenter. In addition, to manufacture a nanotip of a perfect geometrical shape, like a cone or a sphere, is a difficult technical task by itself. Because of that, the shape of each tip needs to be determined individually.

Opportunely, Meyer's similarity principle appears to be also applicable to nanoindentation. According to this principle, the indentation load should be related to the projected area of the indent A_c (Figure 3.8). Thus, it is necessary only to establish the cross-section area as a function of depth.

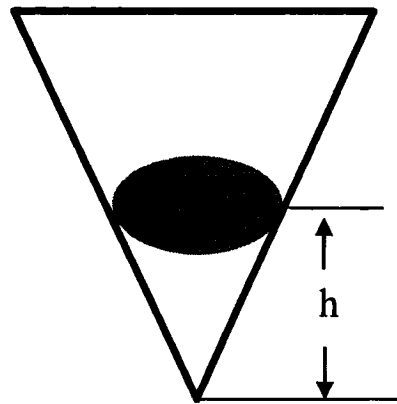


Fig. 3.8 Projected area of an indenter.

In this research we used a 90° degrees conical indenter, dulled by a sphere. The image of it, taken with scanning electron microscope, is shown in Figure 3.9. Since it is technically impossible to manufacture an indenter of a perfect conical shape, all such indenters are dulled with a sphere.

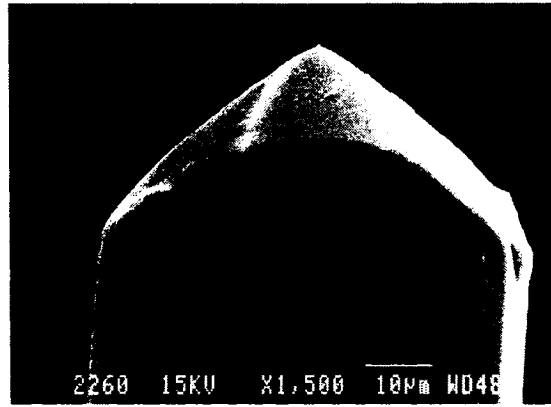


Fig. 3.9 Conical tip, dulled by sphere.

In order to establish the radius of this sphere, we conducted indentations on fused quartz. For a small depth of indentation, within the elastic region, the radius of a spherical indenter can be determined from the following equation [1, 2]:

$$R = \frac{9}{16} \cdot \left(\frac{P}{E} \right)^2 \cdot \frac{(1-\nu)^2}{h^2} \quad (3.3)$$

where:

R – radius of the indenter in m

P – indentation force in N

E – modulus in Pa

ν – Poisson ratio

h - depth of indentation in m

Fused quartz is a standard material, suggested by the manufacturer of the Triboscope. However, it is a very hard material with a modulus of 72 GPa, which is comparable with the modulus of the transducer, $E=1140$ GPa. In this case one should use

the reduced modulus, which includes the modulus and the Poisson ratio of both sample and transducer [77]:

$$E = \frac{1}{\left(\frac{1 - \nu_T^2}{E_T} \right) + \left(\frac{1 - \nu_q^2}{E_q} \right)} \quad (3.4)$$

where:

E_T – modulus of the transducer

E_q – modulus of the fused quartz

ν_T – Poisson ratio of the transducer

ν_q – Poisson ratio of the fused quartz

The load curve used in this experiment is shown below.

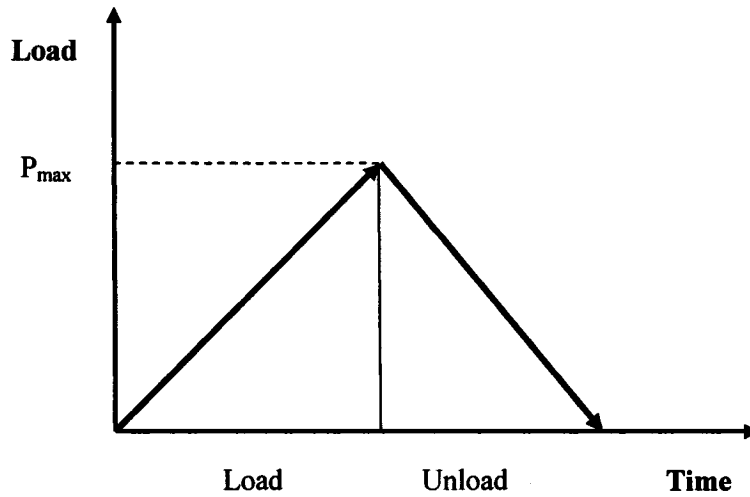


Fig. 3.10 Triangle Load-Time curve.

The results of the experiment are shown as depth of indentation as a function of the indentation load in Figure 3.11

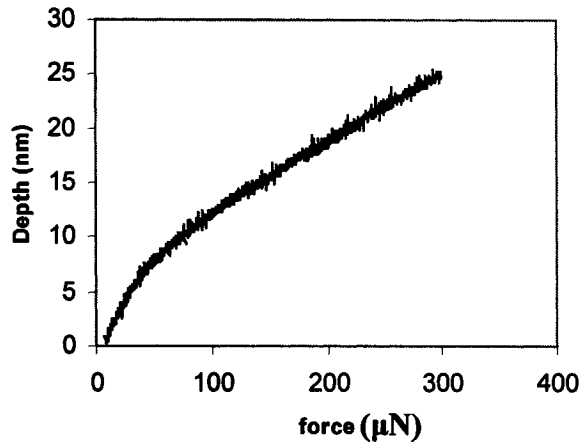


Fig. 3.11 depth of indentation vs. indentation load.

By applying the formula for elastic indentation with a sphere (Equation 3.3) we calculate the radius of curvature of the tip as a function of the indentation depth (Figure 3.12).

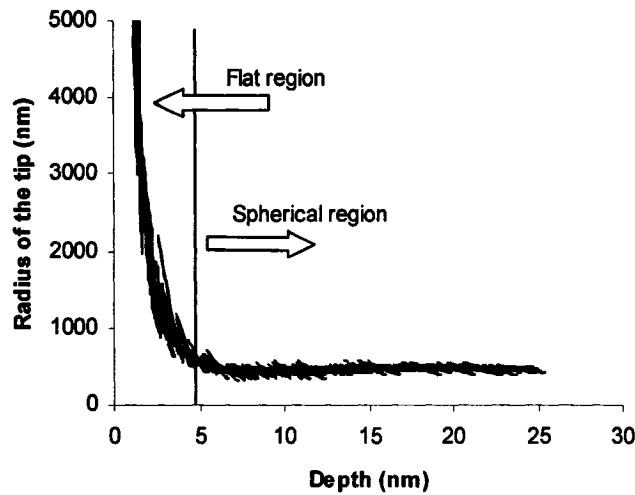


Fig. 3.12 Estimated radius of curvature for a spherical tip.

One can see that in the beginning we estimate a very large radius of sphere, later the curve is practically horizontal. This indicates that this tip has a flattened region

4.8 nm wide, which becomes a fairly good shaped sphere with a radius of 426 nm. Finally the sphere turns into a 90° cone. This geometry is shown below.

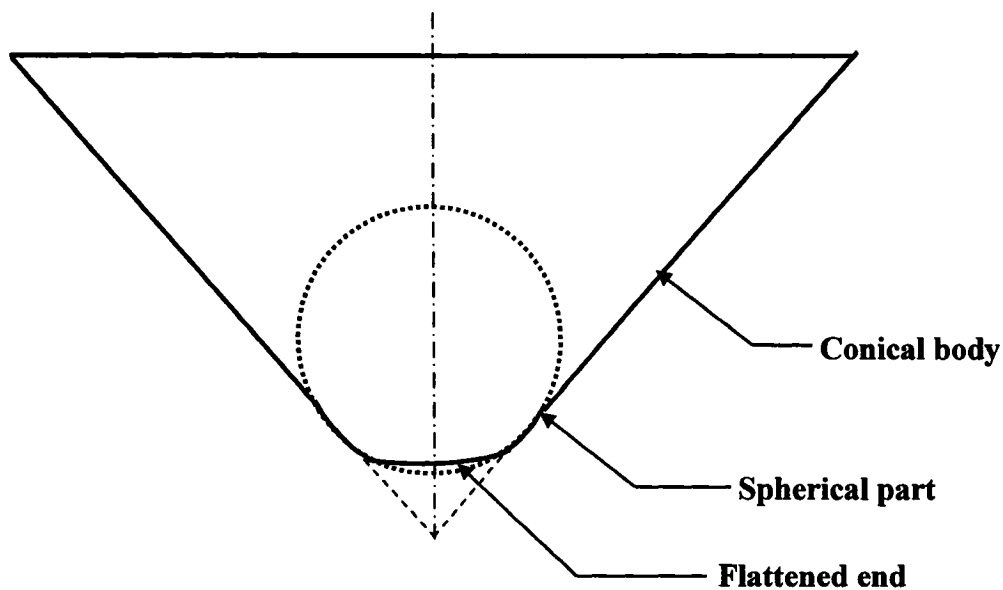


Fig. 3.13 Indenter geometry (not to scale).

3.6 Investigation of polybutadiene: Viscoelastic liquid.

For a viscoelastic liquid in our research we used linear (without cross-linking) polybutadiene [69-74]. Two main reasons for choosing of this material were: firstly, it is hydrophobic toward the material of the indenter, secondly because polybutadiene is a widely used and therefore well-studied material.

3.6.1 Polybutadiene chemical structure.

First we consider the chemical structure and properties of the polybutadiene. In our research we used a polybutadiene synthesized by the Firestone (Bridgestone) company. Without any significant cross-linking, polybutadiene possesses distinct

viscoelastic liquid qualities. The general chemical formula, is $(C_4H_6)_n$; however, a long polymer chain molecule may consist of different monomers that have the same chemical components but different element arrangements. For polybutadiene each isomer contains four atoms of the carbon including one unsaturated double carbon-carbon bond and five or six atoms of hydrogen. Chemical structure analysis made by the manufacturer shows that this particular sample of polybutadiene contains three kinds of polybutadiene isomers: vinyl [1, 2], trans[1, 4] and cis[1, 4], their contents given in the Table 3.2:

Table 3.2 Microstructure of Polybutadiene.

Component	Content, %
vinyl [1, 2]	8.8
trans [1, 4]	53.3
cis [1, 4]	37.7

Graphical representation of structure of each of these isomers is given in Figure 3.14, taken from [43].

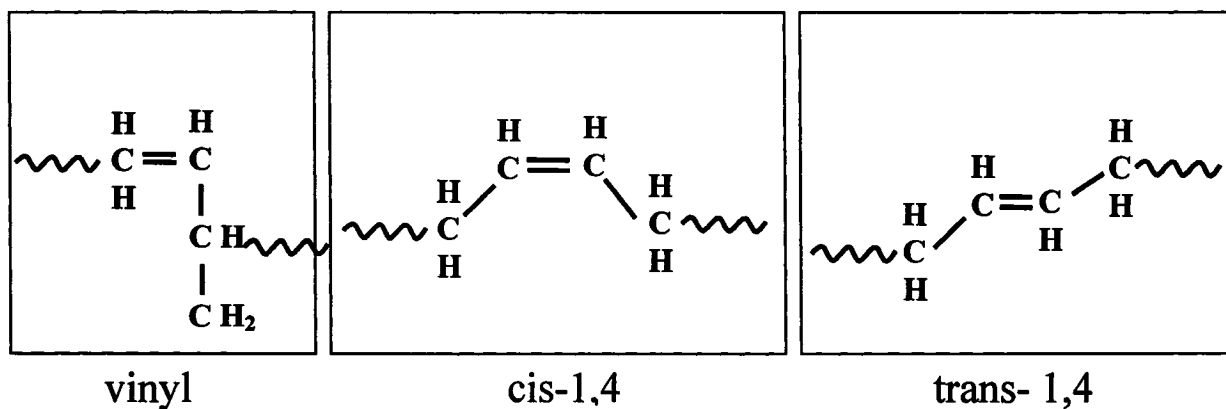


Fig. 3.14 Isomers of polybutadiene.

3.6.2 Physical properties of Polybutadiene.

In this research we investigated the correspondence between the bulk and the local properties of the polybutadiene. Bulk properties were measured using common rheological techniques and local properties were determined by nanoindentation.

3.6.3 Bulk Rheological properties of the Polybutadiene.

The investigated polybutadiene was synthesized at Firestone /Bridgestone Co. (Bridgestone/Firestone Research internal sample I.D.# 2622-114). The dynamic properties were measured with a rotational parallel plate rheometer using the SAOS method (Data received from researcher C.G. Robertson at Firestone). For example, the complex viscosity as a function of ω is shown in Figure 3.15.

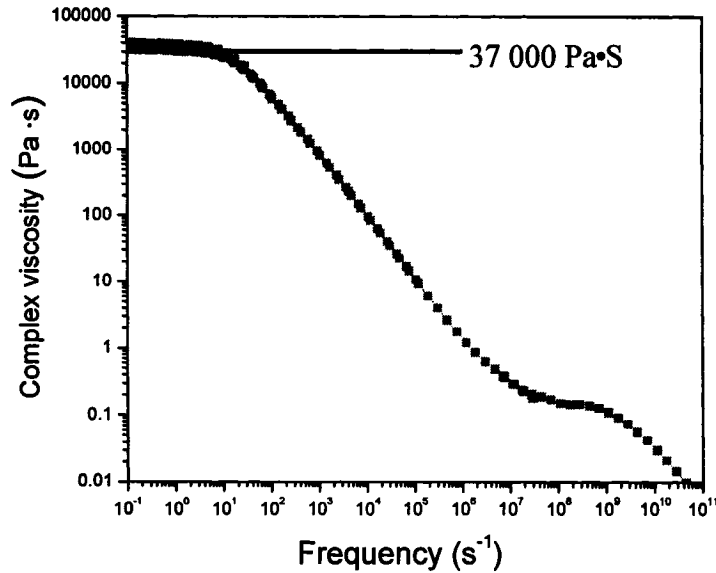


Fig.3.15 Bulk Complex viscosity, $T=25^{\circ}\text{C}$.

Figure 3.15 shows the complex viscosity of the polybutadiene as a function of frequency. We can see that the curve reaches a horizontal plateau at low frequencies ($\omega < 10$) where the viscosity remains constant. This viscosity of approximately constant value at small shear rates is called the zero shear viscosity.

One popular and practical model to simulate the mechanical response of molten polymers is the generalized Maxwell model (GMM) as explained in the section 2.5. Usually in order to model behavior of polymers adequately, the GMM should consist of several Maxwell elements, connected in parallel. However, observation shows that it takes less Maxwell elements to model monodispersed polymers – i.e. polymers with molecular chains of the similar length and structure. The relaxation spectrum which was calculated from the experimental dynamic properties using the numerical procedure of Honerkamp & Weese [42] is shown in Figure 3.16

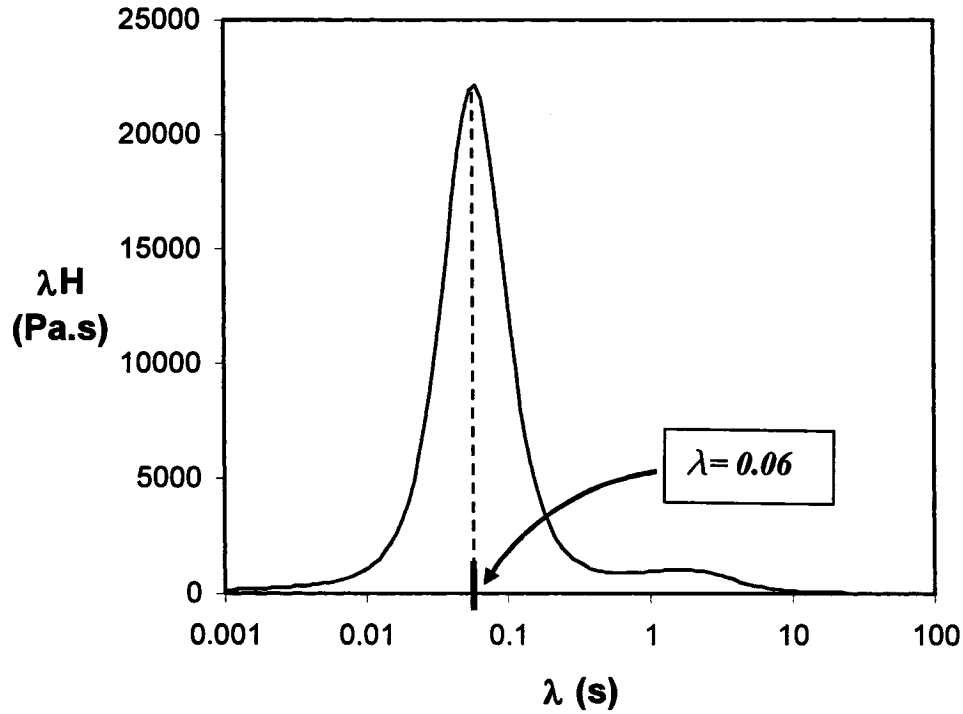


Fig.3.16 Relaxation spectrum of the Polybutadiene.

Analysis of the relaxation spectrum of the Polybutadiene shows that the polymer is rather monodisperse and can be accurately approximated with a single Maxwell element with the following characteristics:

Zero shear viscosity: 37000 Pa·S.

Relaxation time: 0.06 Sec.

These parameters will be used later in the physical model of the nanoindentation in Chapter 4.

3.6.4 Nanoindentation of the Polybutadiene with a spherical indenter.

When the basic bulk rheological properties are established for the polybutadiene, the next step is to conduct nanoindentation tests on the same material and under similar

conditions to find the correlation between the bulk properties and the results of nanoindentation tests that were done with the Hysitron Triboscope.

The first set of experiments were indentations of polybutadiene with a 90 degree diamond conical indenter having a spherical tip with an 8 μ m radius.

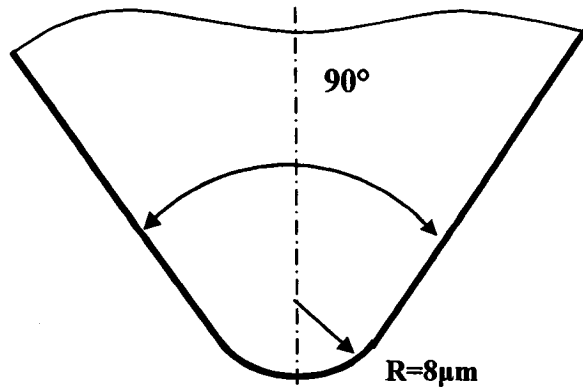


Fig.3.17 Cone-shaped indenter with Spherical tip.

The indentation was done in the closed loop mode with the constant indentation rate of 4.5 μ m/s. Results of this test is shown in Figure 3.18. This experiment was conducted at the Hysitron Inc. experimental site by L. Ionescu, because our laboratory does not have an 8 μ m indenter.

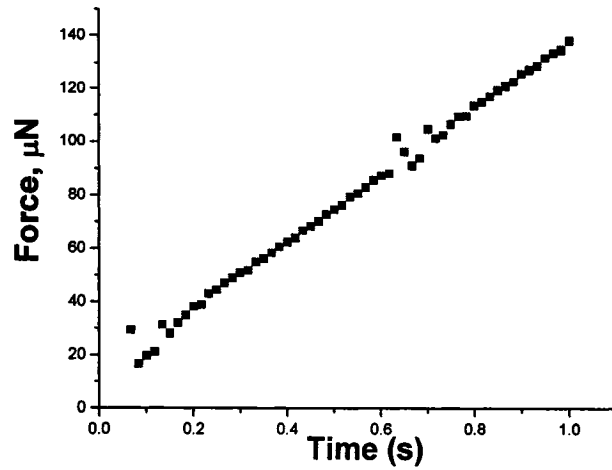


Fig. 3.18 Spherical Indenter, $R=8\text{ mm}$ Indentation rate – $4.5\text{ }\mu\text{m/s}$.

We need to note that the Hysitron Triboscope was originally designed for the testing of solids. The difficulty in applying it to the study of such soft materials such as polybutadiene is that the applied indentation force is very close to the noise level. From the graph in Figure 3.18 one can see that in the beginning of the experiment, when the signal level is low, it is effectively masked by the noise. When this type of indenter is applied on solid materials the indentation loads are expected to be of the order of $10^5\text{ }\mu\text{n}$. For the polybutadiene, however, the maximum load was of the order of $10^2\text{ }\mu\text{N}$. The noise level for the well-controlled, closed-loop mode is about $20\text{-}30\text{ }\mu\text{N}$. Therefore in these experiments on the nanoindentation of polybutadiene the signal to noise ratio is quite low, on the order of 5.

From Figure 3.18 one can also see that the load-time curve is almost a straight line with a slight curvature at small indentation depths. It tells us that for an indentation with a constant rate, the indentation force increases almost linearly. This is an argument in the favor of the use of Stoke's approach for the physical modeling of the indentation process

described in Chapter 4. The summation of the shear and compression forces found from Stokes equations also suggests a linear increase of total force for an indentation with a spherical indenter.

3.6.5 Nanoindentation of Polybutadiene with conical indenter.

Indentations were also conducted on the polybutadiene with another conical indenter with different indentation rates. This cone has an opening angle of 90° and a spherical tip with a radius of 426 nm. Therefore, the depth of the spherical part of the indenter is 124.7 nanometers. The final depth of the indentation for all tests is about 4500 nanometers. Since the spherical tip of the indenter is much smaller than the indentation depth, in our case its shape can be considered to be close to a perfect cone. Experiments were done with constant indentation rates ($4.5\mu\text{m/s}$, $2\mu\text{m/s}$, $1\mu\text{m/s}$ and $0.5\mu\text{m/s}$). Four repeats at different locations were performed at each rate. The repeatability of the indentations with higher indentation rates is significantly better than that with low rates. The least repeatable results are observed for speeds of indentation below $1\mu\text{m/s}$ (see Figure 3.19). A lower rate of indentation into a viscoelastic liquid requires less indentation force, which worsens the signal/noise ratio. Also it takes a longer time to reach the same penetration depth, therefore, increasing the effects of the time and/or temperature drift of the data acquisition system.

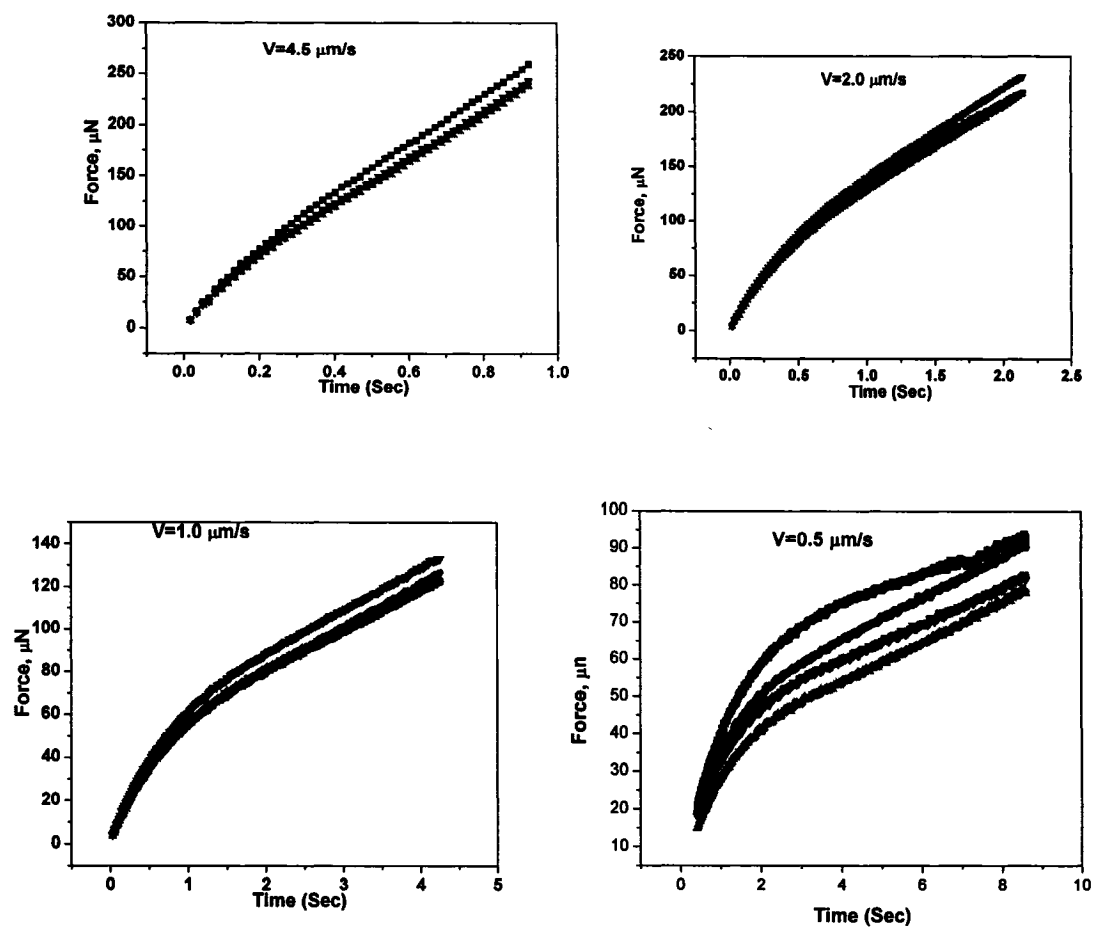


Fig. 3.19 Force vs. time curves for indentation rates 4.5, 2, 1, 0.5 $\mu\text{m/s}$. Polybutadiene.

In Figure 3.19 the average responses at each rate are compared.

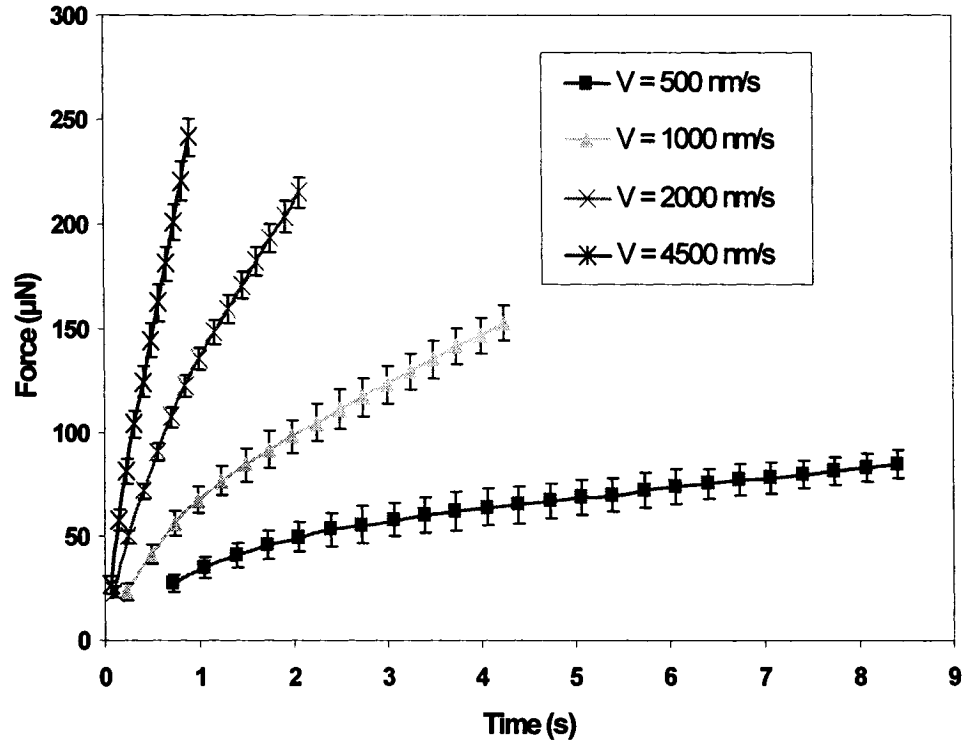


Fig. 3.20 Average force responses of polybutadiene for various indentation rates 4.5, 2, 1, 0.5 $\mu\text{m/s}$. Error bars represent standard deviations.

We can observe the typical pattern of the load-time curve for a constant rate indentation by studying Figure 3.20. First the indentation force growth rate, $\frac{dF}{dt}$, is high and eventually reaches constant value which corresponds to a linear relationship between the force and time. This behavior results from the fact that the polybutadiene is a viscoelastic material. In the beginning, the material response is viscoelastic causing a nonlinear $F(t)$. When the period of indentation becomes much larger than the relaxation time of the viscoelastic material, the indentation becomes practically viscous and the indentation force grows linearly.

We can try to verify how close the indentation process is a steady-state process by superposing the time-depth curves based on the idea of a steady-state conical body moving in a fluid. Then, the drag force would be proportional to the projected area of the axisymmetric body and the speed squared.

$$F_D = C_D A \frac{\rho V^2}{2} \quad (3.5)$$

where:

F_D – Drag force (N)

A – Projected area (m²)

V – Velocity (m/s)

ρ – Density (kg/m³)

C_D – Drag coefficient

In the case of indentation with a conical indenter we can write the following:

$$P = C A_c V_{ind}^2 \quad (3.6)$$

where:

P – Indentation force (N)

A_c – Contact area (m²)

V_{ind} – Indentation rate (m/s)

C – Superposing coefficient

If the process is steady-state, the superposing coefficient C should be constant. In Figure 3.21 we superpose the time-load curves for the indentations 1.0, 2.0 and 4.5 $\mu\text{m/s}$ on the 0.5 $\mu\text{m/s}$ curve, which was chosen as a master curve.

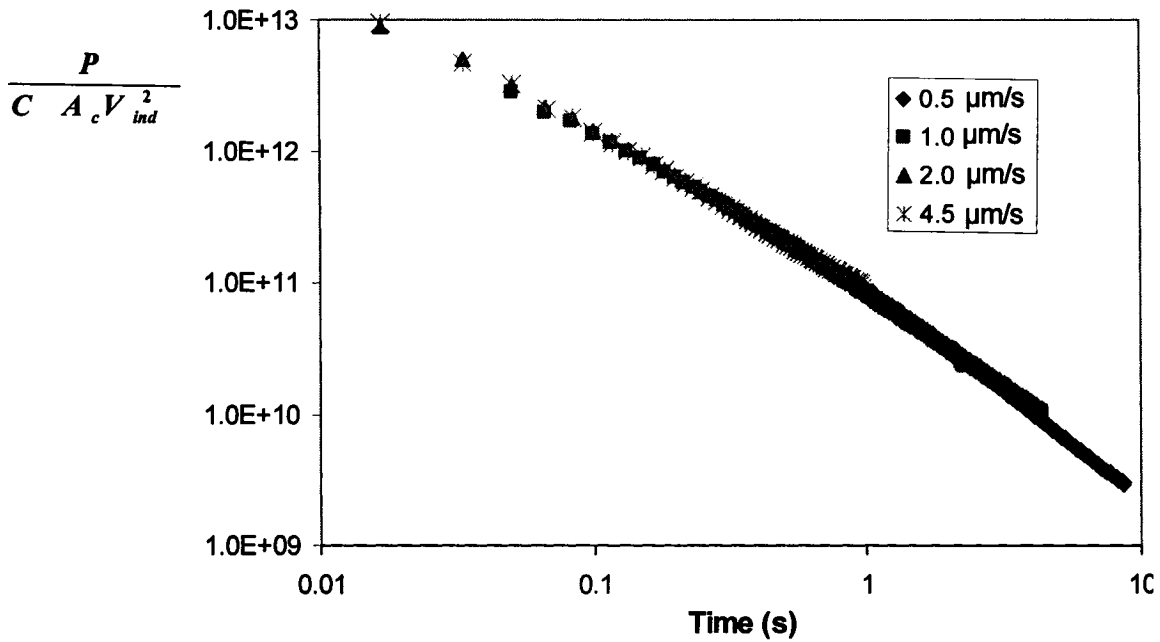


Fig. 3.21 Superposed load-time data for various indentation rates.

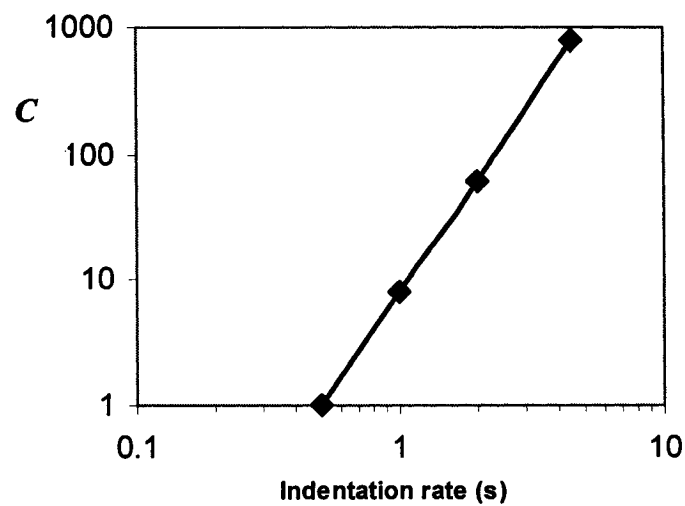


Fig.3.22 Superposing coefficient vs. Indentation rate.

The fact that the coefficient C is not constant (Figure 3.22), but increases by power law when the indentation rate grows, $C \propto V^{3.2}$, indicates that indentations occurred under non-steady state conditions.

In general, the indentation force for constant indentation rate depends on the indentation depth and the indenter geometry. Results of indentation of polybutadiene with the same speed $4.5 \mu\text{m/s}$ with various indenters are shown in Figure 3.23

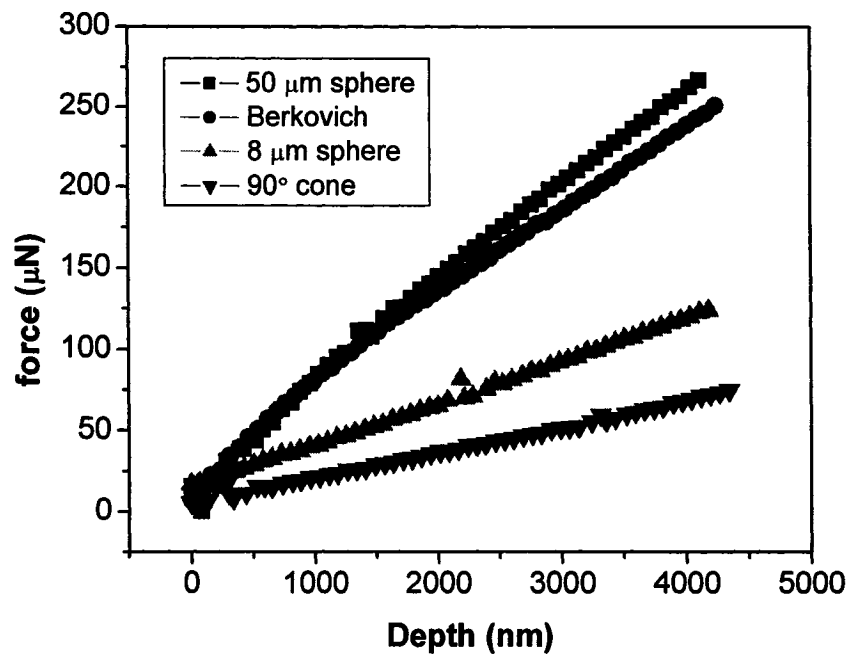


Fig. 3.23 Indentation of polybutadiene.

We have the smallest force of the indentation for the conical indenter, since it has the most “sharp” shape of all tested indenters, i.e. the smallest projected area at small indentation depth. The largest force is observed for the $50\mu\text{m}$ spherical indenter and the Berkovich indenter.

Normalization of the force by dividing it by the contact area shows that for the indentation of polybutadiene this norm asymptotically approaches a constant value,

however the approach rate and the values vary for different types of indenters (see Figure 3.24).

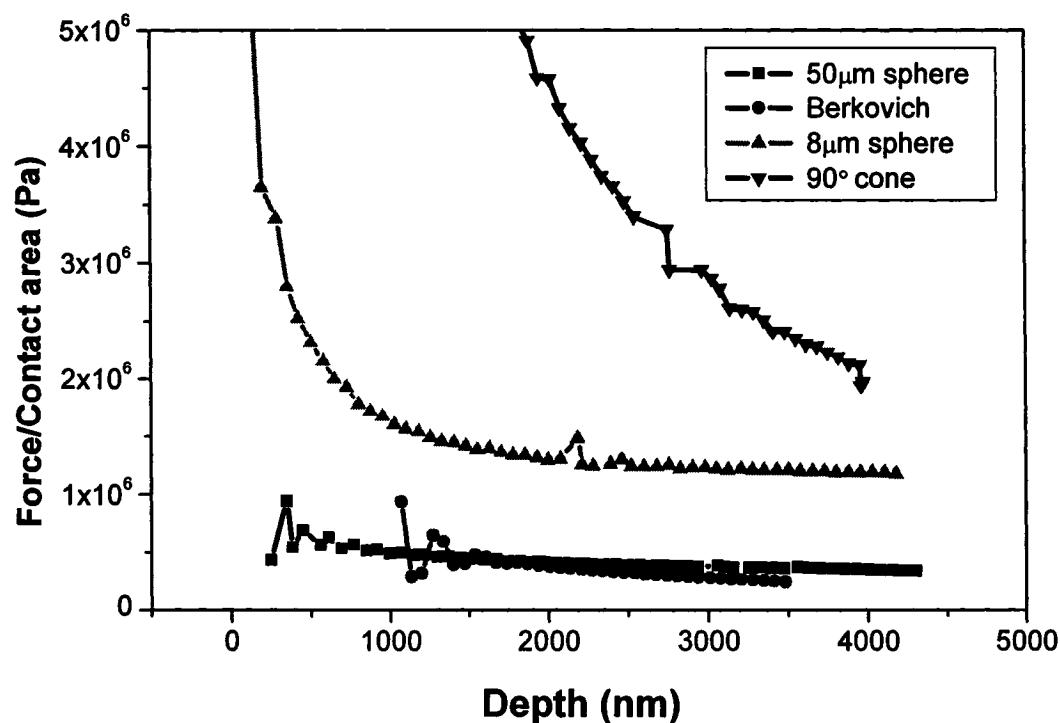


Fig. 3.24 Normalized force for indentation of polybutadiene.

In this normalization we only considered the projected area, disregarding the shape of the indenter. By an observation we can see a close similarity between “dull” indenters like the 50μm sphere and the Berkovich and “sharp” ones – the 8μm sphere and the 90° cone.

3.7. Investigation of cross-linked silicone rubber.

The next step of our research concerns the investigation of a viscoelastic solid by traditional rheological methods and by nanoindentation. For a viscoelastic solid we

choose a cross-linked silicon rubber [66-68]. The general chemical formula for silicon rubbers is shown in Figure 3.25.

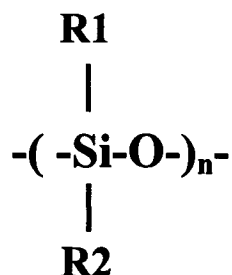


Fig. 3.25 General chemical structure of a silicon Rubber.

At least one of the hydrocarbon groups, *R1* or *R2*, contains an unsaturated double carbon-carbon bond (-C=C-) which allows cross-linking in the presence of curing agent and at elevated temperatures.

3.7.1 Sample preparation.

The silicon cross-linked rubber was molded in-house from its chemical components. It was made by mixing Silastic J RTV Part 21023-Base silicon rubber base with Silastic J Rtv Part 21024 curing agent supplied by the Dow Chemical company. These components were mixed by hand with the curing agent in a proportion of 10 parts of curing agent per 100 parts of rubber base, as specified by the manufacturer. Cross-linking was done in two steps. Primary curing was done in a vacuum oven for 12 hours at a temperature of 60°C and under a vacuum of 28 inch Hg. The vacuum was applied to remove all gaseous components at early stages of curing to reduce porosity and voids within the sample. The second stage of curing was 4 hours at a temperature of 120°C at

normal atmospheric pressure in air to ensure complete cross-linking and chemical stability of the sample at higher temperatures.

The mold was constructed to produce 3 samples of dimensions $45 \times 10.75 \times 10$ mm in one load. From these cross-linked bars samples of rectangular shape $40 \times 10.75 \times 4.1$ mm were cut for rheological tests.

3.7.2 Torsion tests on the cross-linked silicon rubber.

Torsion dynamic mechanical analysis tests were done on a rectangular bar of the cross-linked rubber of dimensions $30 \times 10.75 \times 4.1$ mm. These tests were conducted with an MCR-500 rheometer. The rheometer was adapted for the work with solid samples by installing the special torsion test clamps.

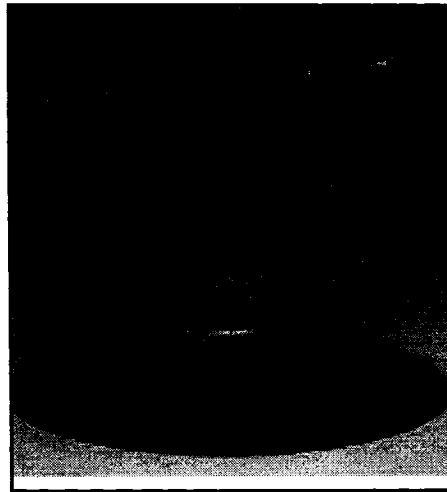


Fig 3.26 Torsion clamp.

Just like common rotational rheometry discussed previously, the torsion test used is based on the SAOS technique. Such tests let us measure the amount of mechanical energy that is stored and recovered in each cycle, and the energy that is lost due to

thermal dissipation. Thus, it allows us to measure basic rheological parameters such as loss and storage modulus.

For the first step we performed a standard strain sweep test to find the linear viscoelastic region. The linear viscoelastic region corresponds to a small enough magnitude of strain or strain rate when the stress from successive deformations is additive. Within the linear regime both the loss and the storage modulus are independent of strain, but do vary with frequency. Figure 3.27 shows results of strain sweep measurement for a frequency of $\omega=10$ Hz for the cross- linked silicon rubber.

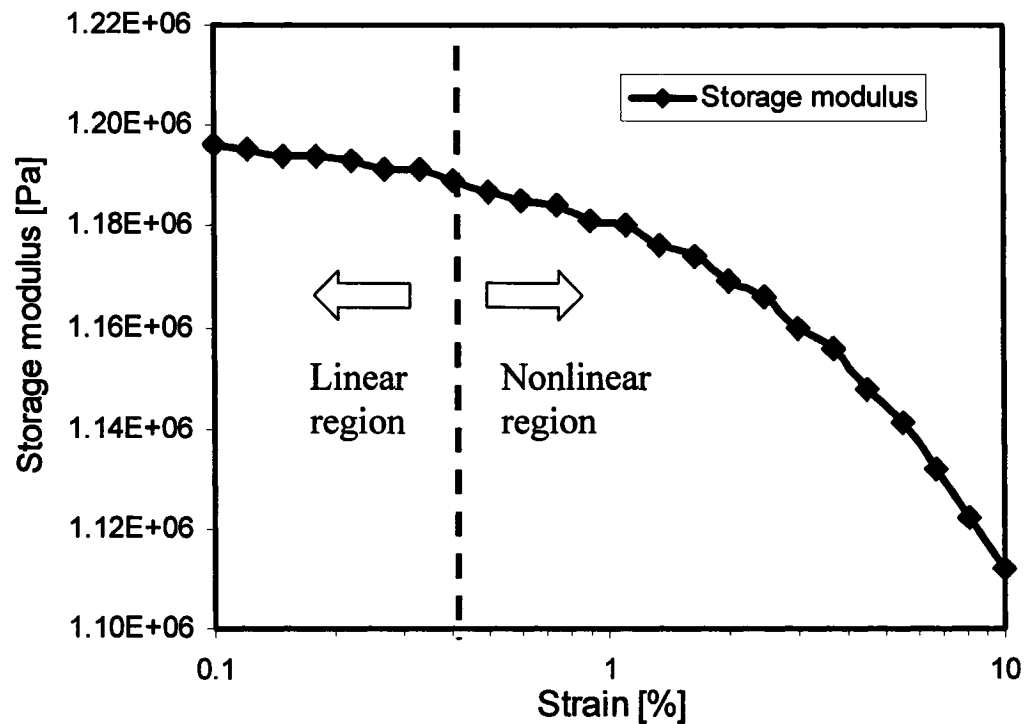


Fig. 3.27 Strain sweep torsion test at frequency $\omega=10$ Hz.

It was determined that the strain limit for the linear regime is $\gamma = 0.2\%$ at 10 Hz. In strain sweep tests, the narrowest linear region is for the highest frequency. Therefore the use of a strain magnitude of 0.2% ensures working within the linear region for all lower frequencies. When the linear region was established the next basic test was the frequency sweep, which was performed at several temperatures. One example is shown in Figure 3.28.

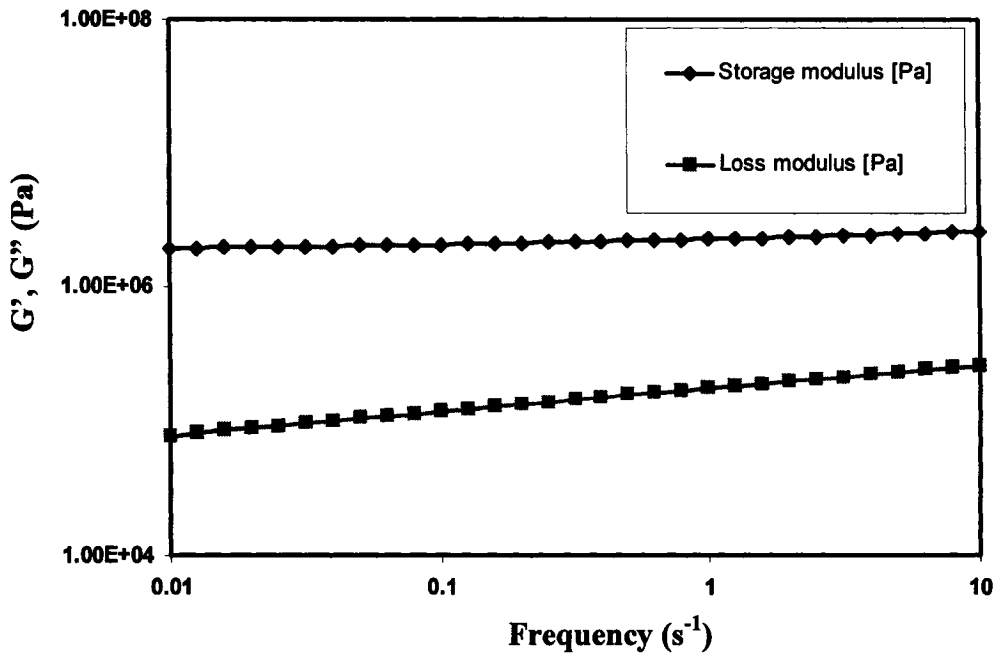


Fig. 3.28 Results of the frequency sweep at 25°C, cross-linked silicone rubber.

3.7.3 Temperature effect on material functions.

In rheology, material functions like the loss modulus, the storage modulus, the viscosity and others are measured as functions of frequency in the SAOS method. Generally, all material functions also depend on the temperature. If data, obtained for a tested material at different temperatures, can be superposed onto one *master curve*, the material is called thermorheologically simple.

The material function measured at the temperature (T) can be shifted to the same material function measured at the reference temperature (T_0) through a time scale shift factor (a_T) and a modulus shift factor (b_T). Graphically, on a log-log scale, (a_T) causes a linear horizontal shift of G' and G'' curves and (b_T) – a vertical one.

Though the shift factor $a_T(T)$ can not always be predicted theoretically for an unknown material, it can easily be found experimentally. Empirically the time scale shift factor $a_T(T)$ often follows the Arrhenius equation:

$$a_T(T) = \exp \left[\frac{E_a}{R} \left(\frac{1}{T} - \frac{1}{T_0} \right) \right] \quad (3.7)$$

where: E_a - activation energy (J/mol)

R – universal gas constant (J/(mol °K))

T – temperature (°K)

T_0 – reference temperature (°K)

For thermorheologically simple materials, increasing the temperature has the same effect on the linear viscoelastic properties as decreasing the frequency. This is the idea of time-temperature superposition.

In order to establish if our material falls into the definition of thermorheologically simple materials, we conducted a series of frequency sweep torsion DMA tests on the cross-linked silicon rubber at different temperatures. The frequency sweep tests were conducted using a strain magnitude of $\gamma = 0.2\%$. The range for the frequency sweep was $\omega = 0.01$ to 10 Hz. These tests were performed at 25°C, 50°C, 75°C and 100°C to find the effect of the temperature on the viscoelastic properties. Next a master curve at 25°C

was built by finding a_T and b_T that best superposed G' and G'' data. The master curve for the storage and loss modulus is shown in Figure 3.29.

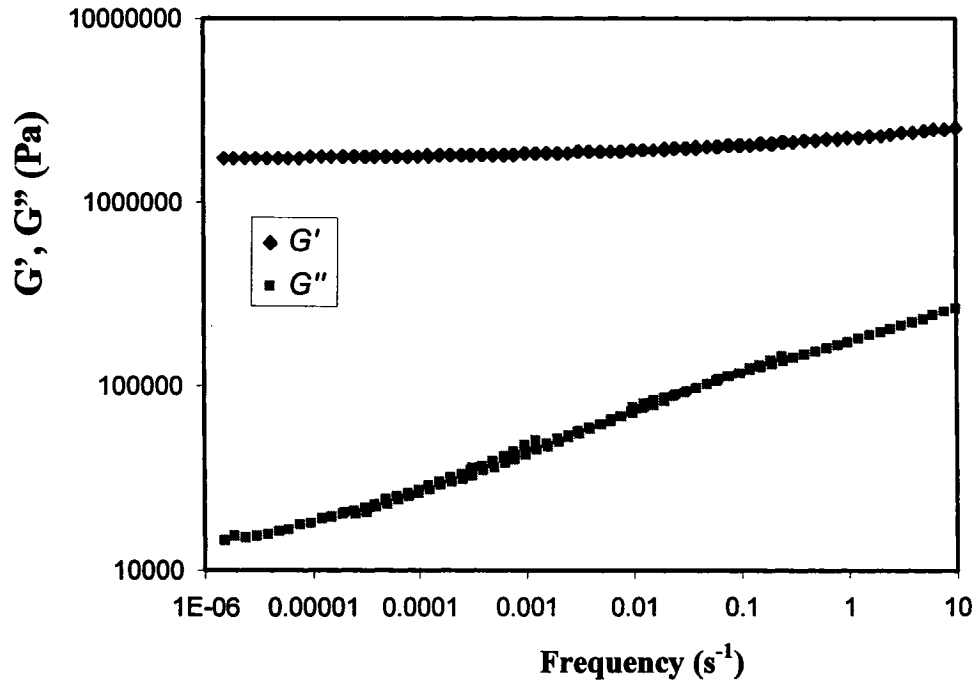


Fig. 3.29 Master curves for loss modulus and storage modulus at $T=25^{\circ}\text{C}$.

Often the modulus shift factor b_T is of the order of 1, then the only superposing shift factor would be the time scale shift factor (a_T). In our case the modulus shift factor (b_T) changes slightly with temperature (Figure 3.30):

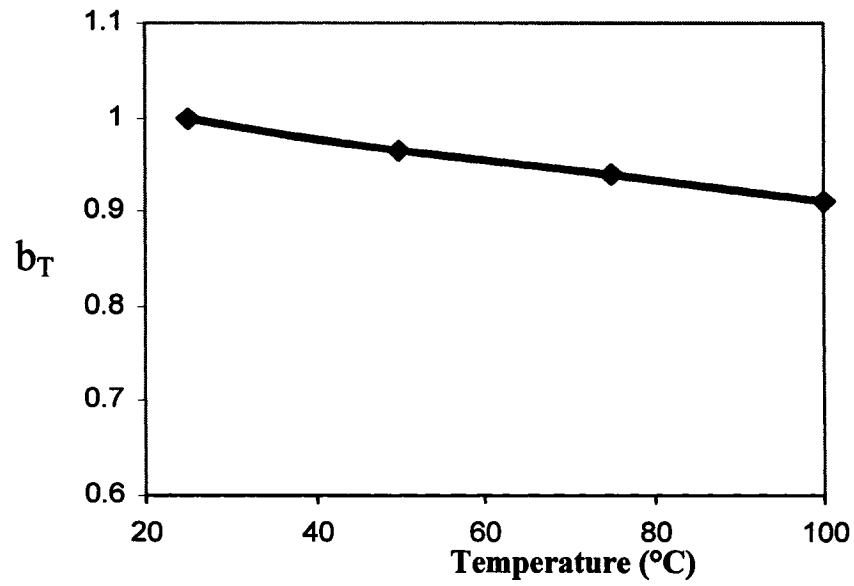


Fig. 3.30 Modulus shift factor (b_T).

The time scale shift factor for the tested cross-linked rubber follows the Arrhenius equation 3.7 with an activation energy $E_a / R = 13007 \text{ K}$.

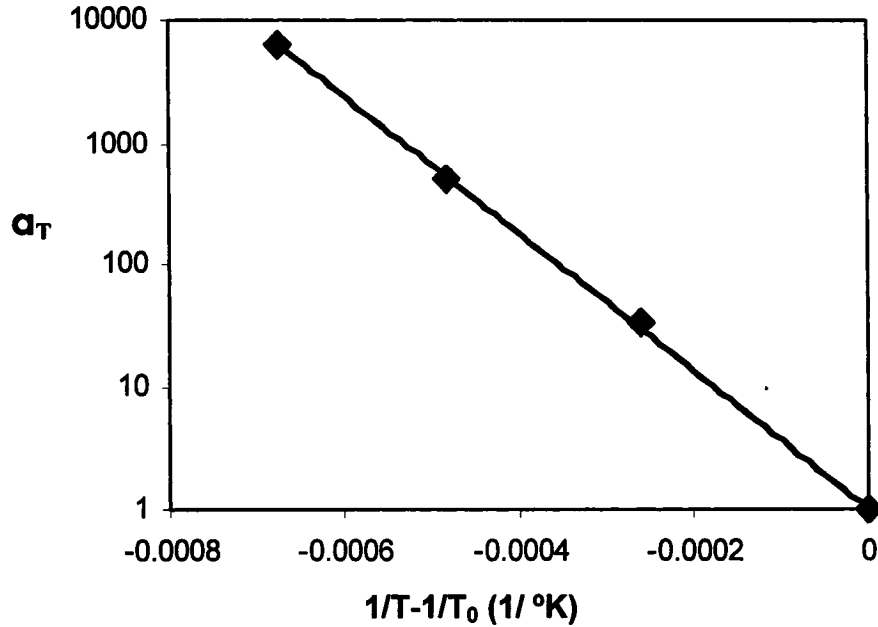


Fig. 3.31 Time scale shift factor (a_T).

3.7.4 Nanoindentation of the silicon rubber.

Nanoindentation was done with a 90 degrees conical indenter dulled with a small spherical tip of radius 426 nm. The maximum depth of the indentations was between 2 and 4.5 μ m. The spherical tip size is small compared with the indentation depth, and therefore it can be considered to be close to a perfect cone.

3.7.5 Step-stress Creep test.

A creep test is an indentation in the closed loop mode with constant force over some period of time. In the beginning of the indentation the force rapidly increases until it reaches the preset value and remains constant for a prescribed period. This is shown in Figure 3.32.

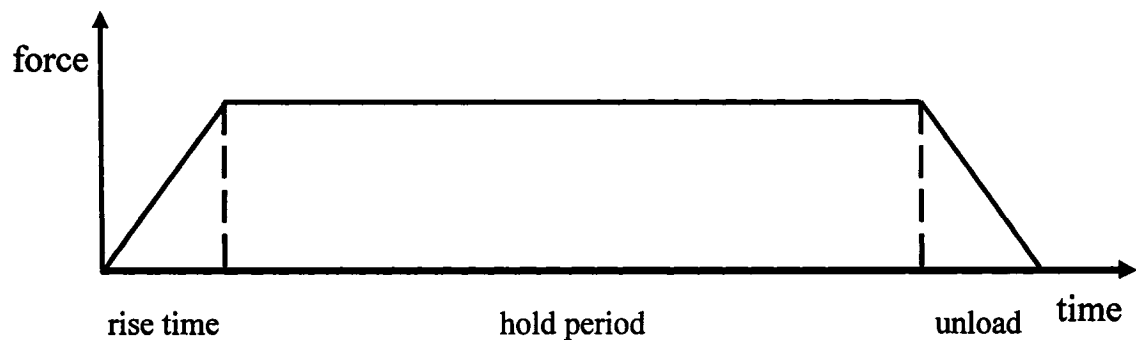


Fig.3.32 Load-time curve for the creep test.

In these creep experiments at the beginning, the step in stress is simulated by a rapid increase of the indentation force to the preset magnitude over a short period of time (within about 0.1 sec), which is limited by the electrostatic transducer. We consider that our step begins at $\frac{1}{2}$ of the rise time. The hold period length was set to 50 sec. It is an

optimal time because it is significantly larger than the relaxation time of our viscoelastic solid. On the other hand it is not exceedingly long, so the drift of the instrument signal does not cause excessive data distortion.

When the tested material is viscoelastic, after the preset load is reached, the indenter continues to creep into the sample. This creeping displacement curve can give us information about the material properties.

A series of indentations with target forces of 30, 50, 80, 100 μN was performed. Each indentation was made at a different location and repeated a number of times. Results showed a significant (up to 30%) deviation in the obtained data (see Fig.3.33). Here both variations in local properties and experimental drift contribute to this phenomenon.

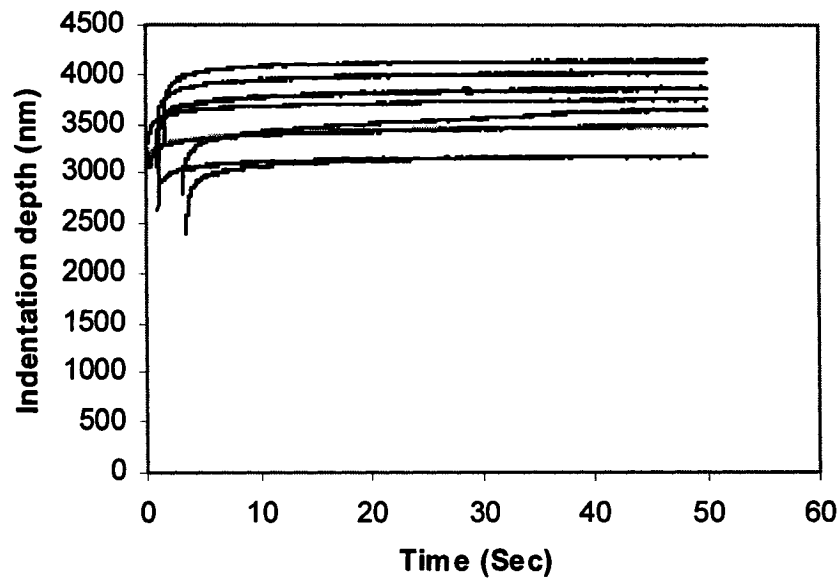


Fig. 3.33 Series of creep tests at a force of 100 μN .

To estimate the contribution of those two factors we conducted several repeated indentation tests at the same location. Results this test are shown in Fig. 3.34. Seven indentations were made in the same location with time interval between indentations of

approximately 10 seconds to allow the material to relax and accept its original form. These tests showed only a small variation due to the time/temperature drift of the instrument. Therefore, we can conclude that the variation in local properties is the primary source of the variation in our data in figure 3.33.

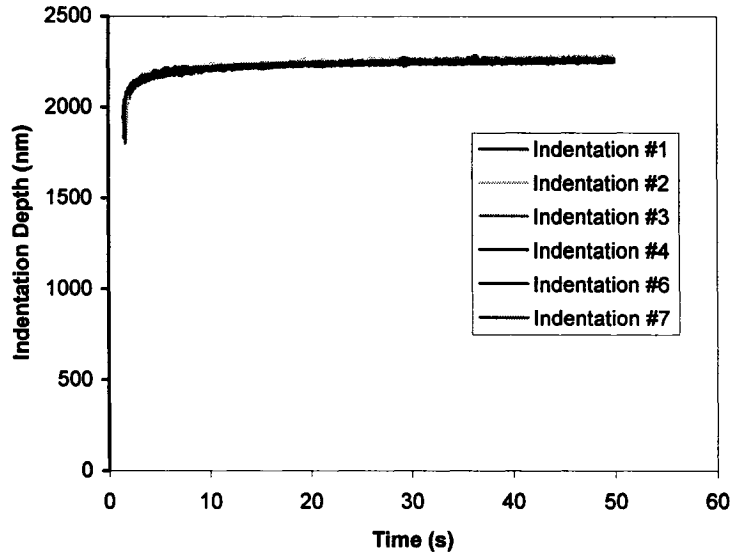


Fig. 3.34 Depth-time curves for repeated indentations.

The analytical solution for the indentation of linear viscoelastic solids with a conical indenter [2,5] gives a general expression for the depth of an indentation as a function of the load.

$$[h(t)]^2 = \frac{1}{C} \int_0^t D(t-t') \frac{dP}{dt'} dt' \quad (3.8)$$

where:

t - time

t' - integration variable

$D(t)$ - creep compliance

$h(t)$ - depth of indentation

C - geometrical factor, which is determined by the cone angle

$$C = \frac{\cot(\beta)}{\pi(1-\nu^2)} \quad (3.9)$$

β – angle between the side of the cone and the horizontal line (Figure 3.35)

ν –Poisson ratio

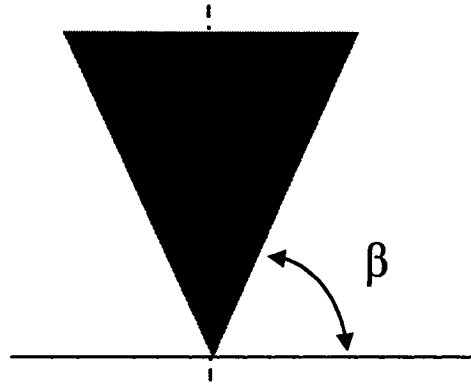


Fig 3.35 Cone geometry.

For a particular case, when an indentation is performed under a constant load

($P_0 = \text{constant}$), the creep compliance as a function of time is given by Equation 3.10

$$D(t) = C \frac{(Vt)^2}{P_0} \quad (3.10)$$

V – indentation velocity

P_0 – indentation force

By using this equation we can estimate the creep compliance from our experimental data. Figure 3.36 shows average creep compliance curves for indentations with step-stresses of range 50-150 μN .

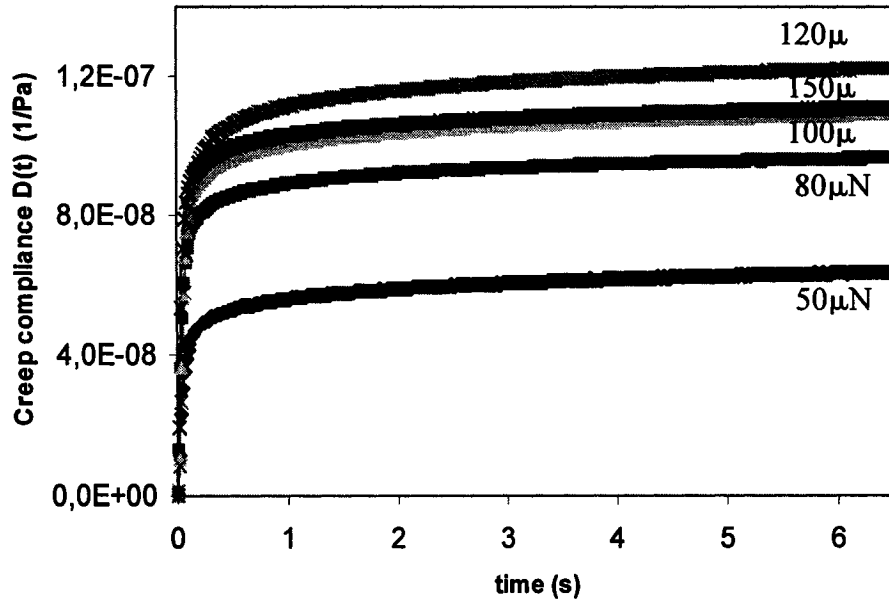


Fig. 3.36 Creep compliance for different step-stress values.

To determine the value of local modulus we can utilize the relationship between limiting values of the creep compliance $D(t \rightarrow \infty)$ and the storage modulus $G'(\omega \rightarrow 0)$. In other words, after a long period of time, the creep compliance $D(t)$ becomes inversely proportional to the storage modulus at zero frequency.

$$\lim_{t \rightarrow \infty} D(t) = \lim_{\omega \rightarrow 0} \frac{1}{3G'(\omega)} \quad (3.11)$$

From the torsion experimental results (See the master curve for the storage modulus Figure 3.36) we estimate that the $\lim D(\infty)$ should be $1.927\text{E-}7$ (1/Pa). We should note that Equation 3.10 is applicable only for a linear viscoelastic indentation. Outside the linear region Equation 3.12 gives only approximate results.

The experiments indicate that creep compliance is a function of both time and indentation force. For a step-load indentation the limiting creep compliance $D(t \rightarrow \infty)$ is a function of the indentation force. It reaches a maximum value of about 65% of the bulk value and reduces at larger force.

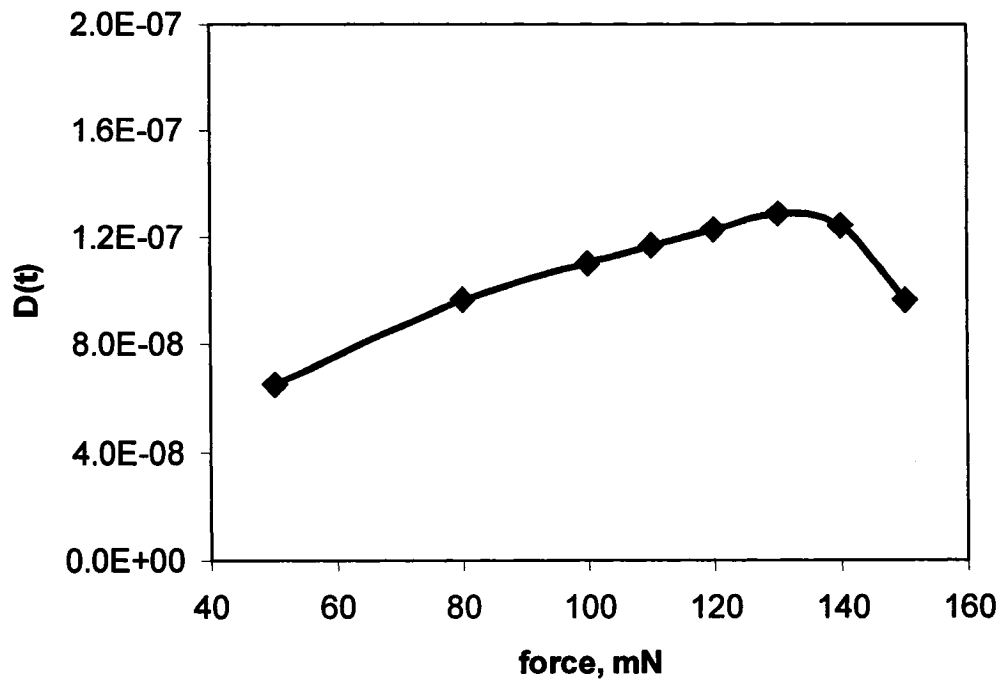


Fig. 3.37 Creep compliance for different indentation force.

This phenomena may be explained by the reaching the limits of the linear viscoelastic regime and/or damaging local network by the indentation.

We should note that Equation 3.10 is applicable only for a linear viscoelastic indentation. In case of a nanoindentation one should conduct indentations with a small depth in order to be in the linear region. Outside the linear region Equation 3.12 gives only approximate results.

CHAPTER 4

Physical models for nanoindentation of viscoelastic materials.

The purpose of the physical modeling is to determine the main physical phenomena involved in the nanoindentation of viscoelastic materials. In the ideal situation, one can suggest a simple set of governing equations. If governing equations realistically explains the results of experiment, it means that the physical theory, they are based on, is applicable to the nanoindentation process.

Traditional indentation was primarily used for testing of solid bodies. Analytical solutions for the indentation of an elastic solid were obtained by Hertz and Love. Later their approach was expanded to the indentation of viscoelastic materials by Sneddon, Ting and others [9-21] and lately experimentally tested by Sakai [1-6]. These models consider only the compression force and are, therefore, applicable mostly to the viscoelastic solids. However, up to now not much work has been gone in the investigation of the indentation of the viscoelastic liquids. For viscoelastic liquids a number of forces need to be accounted. These forces include: shear forces, compression forces, surface tension and buoyancy. The expressions for these forces can be obtained by applying the concepts of fluid mechanics, as is done in this chapter.

4.1 Stoke's theory of creeping flow.

The indentation of viscoelastic liquids can be considered as a viscous flow of a liquid around the indenter. Nanoindentation is usually performed only on samples with

high viscosity -typically on the order of 10^5 Pa·s or more. Also, because of the tiny characteristic size of the indenters (within a few micrometers) and relatively slow indentation rate (dozens of micrometers per second) the Reynolds number for such a flow is very small (on the order of 10^{-5} or less).

$$\text{Re} = \frac{Vd}{\nu}, \quad \text{where} \quad (4.1)$$

V – flow velocity

d - Characteristic size

ν - kinematic viscosity.

A small Reynolds number indicates that viscous forces dominate over the forces of inertia. Therefore, a logical choice for the basis of a physical model is Stoke's theory of creeping flow: slow laminar non-rotational flow of an incompressible, Newtonian fluid around a solid indenter with non-slip boundary conditions. Stokes found an analytical solution for a creeping, or ideal flow around a sphere completely submerged in fluid [35].

Such a flow is shown in Figure 4.1

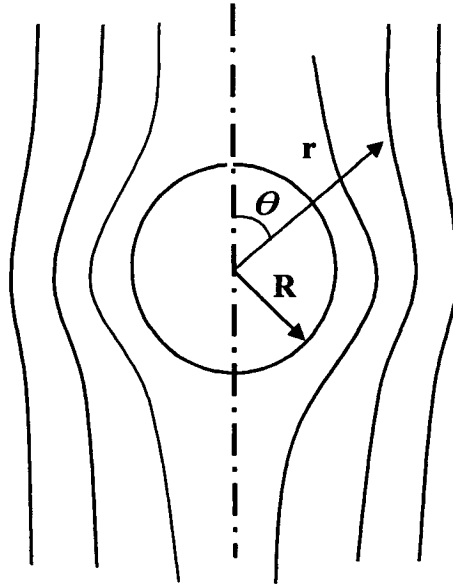


Fig. 4.1 Ideal flow around a sphere.

Later improved formulas for creeping flow were suggested by Oseen [35]. At very small Reynolds numbers ($Re < 10^{-2}$) Stokes and Oseen solutions give practically identical results. The Stoke's theory has been verified experimentally and proven to be valid for Newtonian flows with Reynolds numbers ($Re < 10^{-2}$) around fully submerged spheres. For many polymer melts the Reynold's number will be even smaller than that, so the use of the Stoke's theory is well justified. At the same time, the application of the Stoke's theory has some limitations. The analytical solution has been obtained only for a flow of a Newtonian fluid around fully submerged bodies of spherical shape, no models for flow around other shapes of indenters - like cones or pyramids are available. In his approach Stokes considers a steady flow around a fully submerged sphere. Only recently a few works dealing with unsteady ideal flow around partly submerged small size solid bodies has been published [47-52].

4.2 Indentation of liquids.

Stoke's solution gives velocity and pressure fields, which allows us to calculate shear stress and pressure on the surface for the spherical part of the indenter. The velocity distribution in the spherical system of coordinates is:

$$v_r = v_\infty \left(1 - \frac{3}{2} \left(\frac{R}{r} \right) + \frac{1}{2} \left(\frac{R}{r} \right)^3 \right) \cos(\theta) \quad (4.2)$$

$$v_\theta = -v_\infty \left(1 - \frac{3}{4} \left(\frac{R}{r} \right) + \frac{1}{4} \left(\frac{R}{r} \right)^3 \right) \sin(\theta) \quad (4.3)$$

Where (see Figure 4.1):

R – radius of sphere

r – distance from the center of the sphere

θ – angle from the z-axis

v – velocity

During a test the total force applied on the indenter by the driver will be equal to the sum of the forces acting on the submerged portion of the tip.

$$F_{TOTAL} = F_{COMPRESSION} + F_{SHEAR} + F_{SURFTENSION} + F_{BUOYANCY} \quad (4.4)$$

We will consider each of these forces in turn. We begin with the compressive and shear forces.

Stoke's expression for shear stress on the surface of a spherical indenter is as follows:

$$\tau_{r\theta} = -\frac{3}{2} \frac{\mu v_{\infty}}{R} \left(\frac{R}{r} \right)^4 \sin(\theta) \quad (4.5)$$

μ – viscosity.

And the pressure component of the stress is:

$$p = p_0 - \rho g z - \frac{3}{2} \frac{\mu v_{\infty}}{R} \left(\frac{R}{r} \right)^2 \cos(\theta) \quad (4.6)$$

One of difficulties of interpretation of the results is that the Triboscope does not distinguish the force components and registers only the sum of the vertical components of all acting forces. Compression and shear forces can be determined separately using the Stoke's theory. Here we make an assumption that the velocity distribution during indentation is similar to the one for the ideal flow around a completely submerged sphere and we consider the flow as a quasi-steady state. This idea is shown in Fig. 4.2

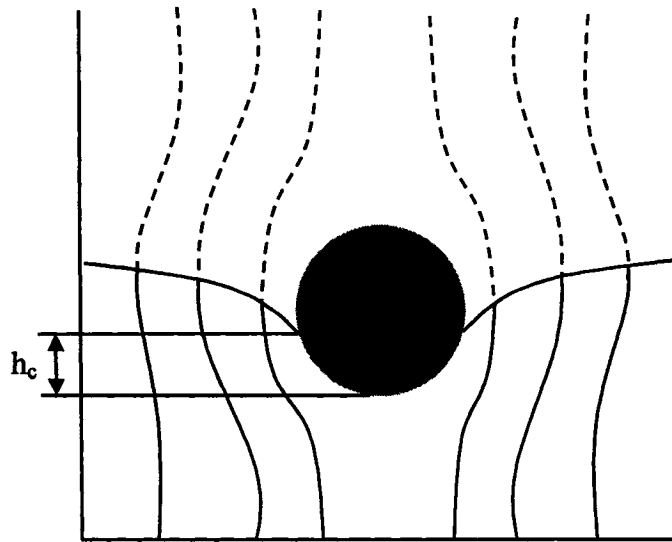
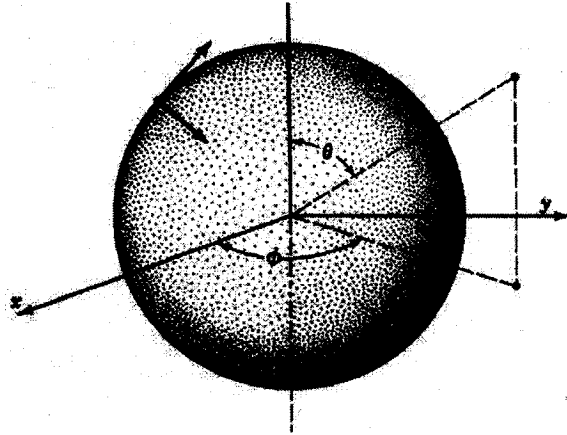


Fig. 4.2 Flow around spherical indenter.

Then the compression and shear forces acting on the indenter are integrated over the submerged part of surface. The spherical system of coordinates is shown in Fig. 4.3 along with the nomenclature.



R – radius of spherical indenter

r – distance from the center of sphere

θ, φ – spherical system angles

Fig. 4.3 Spherical system of coordinates.

First we consider the normal stress to calculate the compression force. To obtain the total compression force acting on the indenter we integrate the vertical component of the normal stress σ_{rr} over the submerged part of the indenter. In the spherical system of coordinates it is appropriate to express the geometry of the submerged part by the angle (β) between the z-axis and the line connecting the center of the sphere with the interface line (see Fig.4.4).

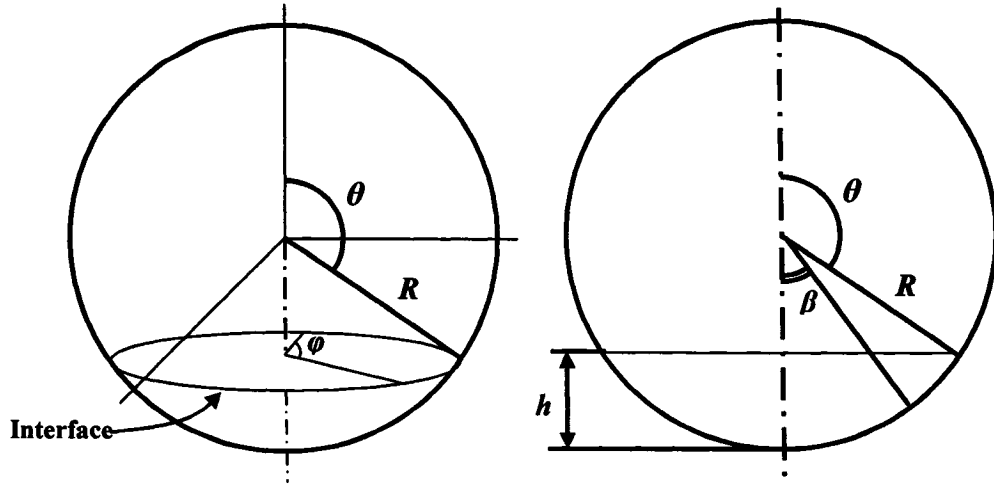


Fig. 4.4 Indentation geometry.

The normal stress on the surface of a submerged sphere is:

$$\sigma_{rr} = \frac{3}{2} \frac{\mu V_{\infty}}{R} \cos \theta \quad (4.7)$$

and the total force due to compression in the z-direction is:

$$F_{comp} = \int_A (\sigma_{rr}) \cos(\theta) dA \quad (4.8)$$

dA – area element on a sphere surface.

In a spherical system of coordinates an area element on a sphere of radius R is:

$$dA = R^2 \sin \theta \, d\theta \, d\varphi \quad (4.9)$$

then, an expression for compression force for a fully submerged sphere is:

$$F_{comp}(\beta) = \int_{\varphi=0}^{\varphi=2\pi} \int_{\theta=0}^{\theta=\pi} (\sigma_{rr}) \cos(\theta) R^2 \sin(\theta) \, d\theta \, d\varphi \quad (4.10)$$

and for a partly submerged sphere is:

$$F_{comp}(\beta) = \int_{\varphi=0}^{\varphi=2\pi} \int_{\theta=\pi}^{\theta=\pi-\beta(h)} (\sigma_{rr}) \cos(\theta) R^2 \sin(\theta) d\theta d\varphi \quad (4.11)$$

For a certain depth of indentation, (h) the angle (β) is given in the Equation 4.8:

$$\beta(h) = \arccos\left(\frac{R-h}{R}\right) = \arccos\left(1 - \frac{h}{R}\right) \quad (4.12)$$

Finally, by combining these equations we get:

$$F_{COMP}(h) = \int_{\varphi=0}^{\varphi=2\pi} \int_{\theta=\pi}^{\theta=\pi-\arccos\left(1-\frac{h}{R}\right)} \left(\frac{3}{2} \frac{\mu v_{\infty}}{R} \cos(\theta)\right) \cos(\theta) R^2 \sin(\theta) d\theta d\varphi \quad (4.13)$$

This integral is simple to solve, giving:

$$F_{COMP} = \frac{\pi \mu V_{\infty} h (3R^2 - 3Rh + h^2)}{R^2} \quad (4.14)$$

When we deal with non-Newtonian liquids a proper viscoelastic model has to be employed. In order to simplify our derivations, we use an approximate approach based on the Maxwell model. We assume that viscosity is a function of time:

$$\mu = \mu_0 \left(1 - \exp\left(-\frac{t-t_0}{\lambda}\right) \right) \quad (4.15)$$

where:

λ - relaxation constant to be determined.

t_0 – shear flow “start time”, which will be different for each level of the indenter. It

indicates time when one particular part of the indenter comes into contact with tested material. It can be expressed as a function of θ .

t – total time of the indentation.

This approach is valid for a simple flow. Here we apply it to the complex flow of an indentation and assume that errors introduced will be small.

$$F_{COMP} = 3\pi\mu V_{\infty} R \int_{\pi}^{\pi-\beta(h)} \left(1 - \exp\left(\frac{t-t_0}{\lambda}\right) \right) \cos^2 \theta \cdot \sin \theta \, d\theta \quad (4.16)$$

Generally the depth of the indentation is a function of time:

$$h_{IND} = \int_0^t V_{\infty}(t) dt \quad (4.17)$$

For indentation with a constant rate, the indentation depth is:

$$h_{IND} = V_{\infty} \cdot t \quad (4.18)$$

For low viscosity fluids the contact depth (h) is very close to the total displacement of the tip during the indentation h_{IND} . However, for highly viscous liquids the contact depth is always smaller than the total indentation depth. This is a result of bending of the interface boundary as shown in Figure 4.5.

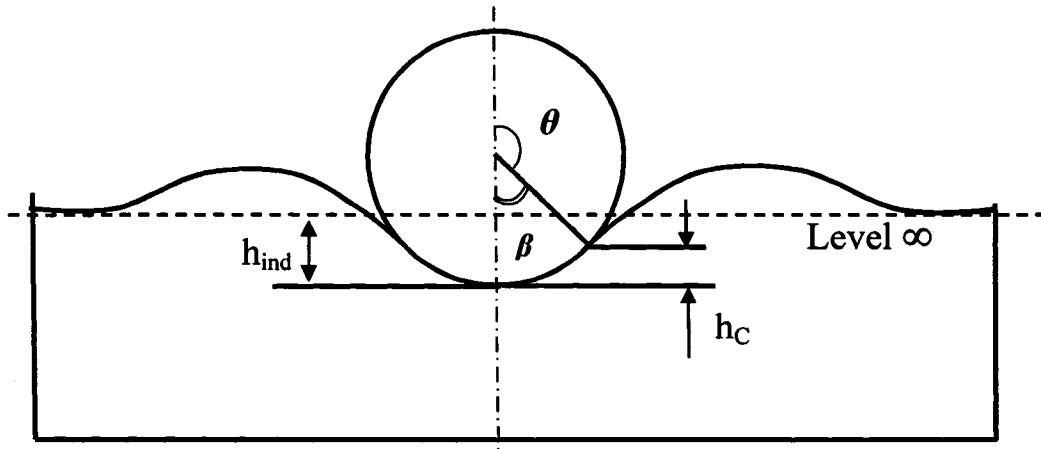


Fig. 4.5 Deformation of interface boundary during indentation.

For indentations with constant rate, the contact depth is proportional to the indentation depth.

$$h_c = C_1 h_{IND} \quad (4.19)$$

This phenomenon will be discussed in more detail in Chapter 5.

For a constant rate indentation, time t_0 can be easily related to the depth h_c at an angle θ :

$$t_0(\theta) = C_1 h(\theta) / V_{Ind} = \frac{R}{C_1} (1 - \cos \theta) / V_{Ind} \quad (4.20)$$

The current indentation time is related to β as below:

$$t(\beta) = C_1 h(\beta) / V_{Ind} = \frac{R}{C_1} (1 - \cos \beta) / V_{Ind}$$

When this expression used in the equation 4.20, the compression force becomes solely a function of θ .

Now we consider the shear forces. Recall that Stoke's solution gives the shear stress as:

$$\tau_{r\theta} = \frac{3}{2} \frac{\mu v_{\infty}}{R} \left(\frac{R}{r} \right)^2 \sin(\theta) \quad (4.21)$$

Following the same procedure as before, we integrate the vertical component of shear stress ($\tau_{r\theta}$) over the submerged portion of a spherical indenter.

$$F_{SHEAR}(h) = \int_{\varphi=0}^{\varphi=2\pi} \int_{\theta=\pi}^{\theta=\pi-\beta} (\tau_{r\theta}) R \sin^2 \theta d\theta d\varphi \quad (4.22)$$

Solution of this integral gives an expression for shear forces as a function of the indentation depth:

$$F_{SHEAR}(h) = \frac{\pi \mu v_{\infty} h^2 (3R - h)}{R^2} \quad (4.23)$$

Again, following the same idea as with the normal stress, we get the shear forces for a viscoelastic liquid:

$$F_{SHEAR}(\beta) = 3\pi V R \eta \int_{\pi-\beta}^{\pi} \left(1 - \exp\left(\frac{t-t_0}{\lambda} \right) \right) \cos \theta \cdot \sin^2 \theta d\theta \quad (4.24)$$

These equations can easily be solved numerically.

4.1.3. Surface tension force.

In traditional indentation surface tension forces are usually neglected. However, at nanoscale these forces can make significant contribution in the force balance and often

need to be accounted for. Surface forces act along the contact line between the polymer and the indenter as shown in Figure 4.6.

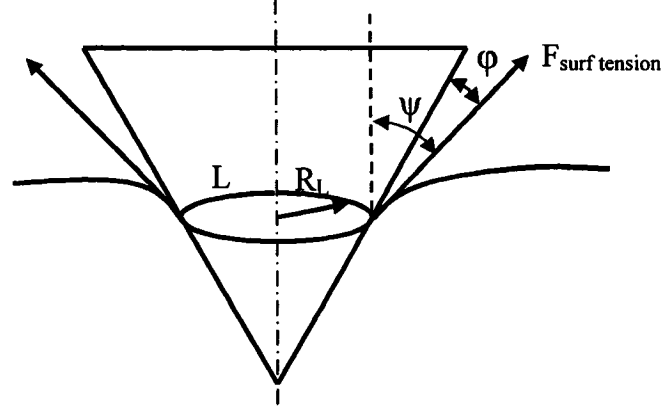


Fig. 4.6 Surface tension forces.

Surface forces depend on the surface energies of the polymer and indenter and the wetting angle. The last one depends on number of parameters. Even if we assume a situation when the wetting angle is 0, the surface tension forces are directed tangentially toward the surface of the indenter and act the most effectively, the surface tension force usually remains at least an order of magnitude smaller than the compression and shear ones.

$$F_{SURF.TENSION} = \gamma \cdot L \cdot \cos\psi \quad (4.25)$$

For a spherical indenter:

$$L = 2\pi R_L = 2\pi \sqrt{2R_L h_C - h_C^2} \quad (4.26)$$

where :

γ -surface tension

L - perimeter of the contact (interface) line

Because of the surface tension force, it is crucial to select a suitable combination of material of the indenter tip and the material under investigation, to exclude wetting of the indenter. It was found that when the tested viscoelastic liquid wets the indenter, nanoindentation measurements become very difficult, if not impossible.

In case of the polybutadiene indentation the surface tension force makes a visible contribution, though it is an order of magnitude smaller than the compression and shear forces (see Figure. 4.8).

4.1.4. Buoyancy force.

When the viscoelastic material under study is a liquid, we can determine the buoyancy force which is proportional to the density of polymer and the volume of the submerged portion of the sphere.

$$F_{BUOYANCY}(h) = V(h) \cdot \rho \cdot g \quad (4.27)$$

where:

g - is the gravitational constant

ρ - density of the tested material

$V(h)$ - volume of the submerged part, which can be expressed as a function of the depth of an indentation, h .

h - depth of indentation, generally is a function of time $h(t)$

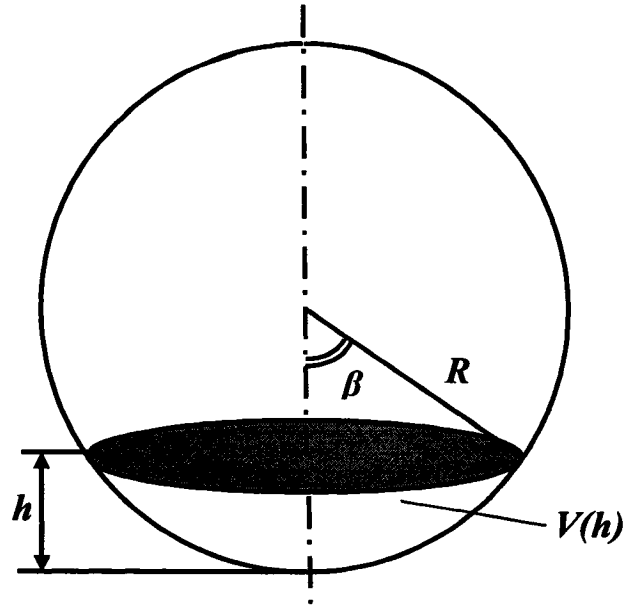


Fig. 4.7 Portion of the indenter, submerged in a polymer.

For a spherical indenter, the volume of the submerged portion is:

$$V(h) = \pi h^2(t) \left(R - \frac{1}{3} h(t) \right) \quad (4.28)$$

The buoyancy force is the smallest of all forces considered here. Typically for nanoindentation it is several orders of magnitude smaller than compression or shear forces and can be neglected with no significant impact on the accuracy.

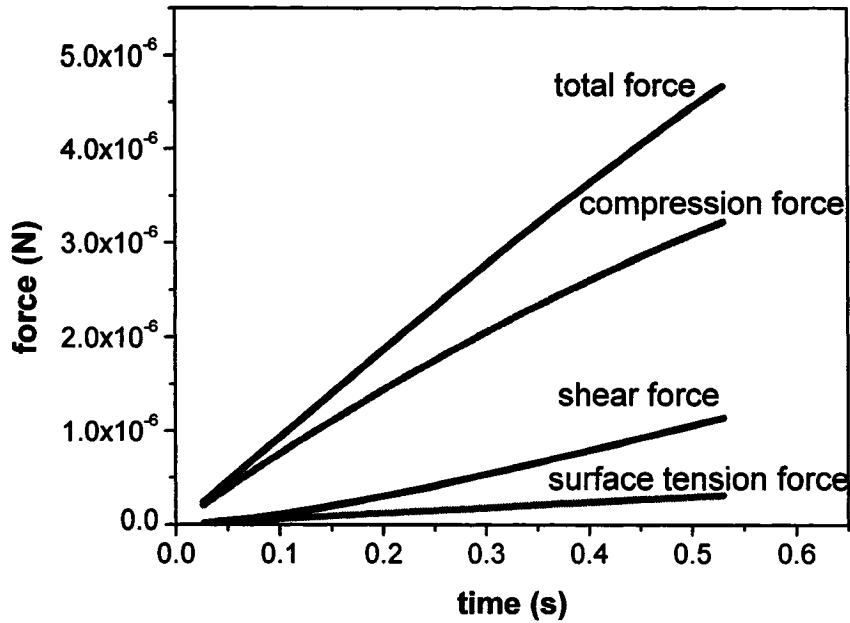


Fig. 4.8 Forces in Polybutadiene indentation from Stoke's theory.

$$R=8\mu\text{m}, V=4.5\mu\text{m/s}, \mu=37000\text{ Pa}\cdot\text{s}.$$

Using this approach we can predict the different forces acting on the indenter during an indentation. For a spherical indenter, in the beginning, when the depth of the indentation is small compared to the radius of the indenter, the compression force dominates and the shear force is small because its vectors at the flat part of the tip are almost orthogonal to the z-axis of the indentation. Later, however, the compression force grows slower than the shear force. Eventually, by the Stoke's theory, for a fully submerged sphere, the overall shear force component is twice as big as the compression component.

4.2 Stokes theory approach in the modeling of AFM tapping mode.

Recently the use of a simplified version of Stoke's theory to interpret phase shift data obtained by tapping mode of atomic force microscopy (AFM) has been reported for rather soft materials. In tapping mode a tip at the end of a vibrating cantilever comes in contact for a short time with the surface of a material under study and then bounces up.

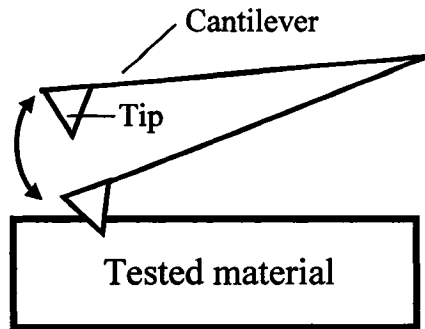


Fig. 4.9 Taping mode of AFM.

The depth of the tip's penetration (indentation) into the surface is very small, even compared to the size of the AFM tip, approximately 10-50 nm. If the material under study exhibits properties of a fluid, its viscosity will be one of the important factors that affects the whole cantilever motion.

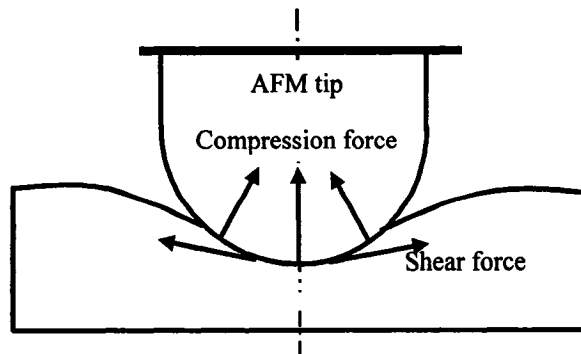


Fig. 4.10 Compression and Shear forces in AFM.

The influence of the material viscosity on the force balance can be estimated by simplification of the results, described in sections 4.11, 4.12. For AFM measurements, the depth of the tip penetration, (h), is much smaller than the tip radius (R_{tip}). Then the component of the shear forces in the z-direction is very small and can be neglected.

If the surface tension and the buoyancy forces are also neglected, then the only significant force left, is the compression force. We can rewrite Equation 4.17 as:

$$F_{COMP} = \frac{3\pi\mu\nu_{\infty}h}{R^2} \left(R^2 \right) - \frac{3\pi\mu\nu_{\infty}h^2R}{R^2} + \frac{\pi\mu\nu_{\infty}h^3}{R^2} \quad (4.29)$$

Recalling that $R \gg h$, we can neglect the second and third terms of the equation. Then Equation 4.31 reduces to:

$$F_{COMP} = 3\pi\mu\nu_{\infty}h \quad (4.30)$$

Note that the compression force then is proportional to the viscosity and the depth of indentation, but does not depend on the radius of the tip.

In the AFM (Atomic Force Microscopy) the only parameters measured are related to the motion of the cantilever. Therefore other parameters must to be found indirectly. In tapping mode the cantilever makes vertical oscillatory movements and hits the investigated surface at lowest part of oscillation wave. When it bounces up from the surface, a phase shift in the cantilever motion occurs. This shift depends of the properties of the cantilever, parameters of its motion and, obviously on the properties of the tested

material. The last ones are to be measured. Such, for materials with simple properties, knowing the compression Stoke's force acting on an AFM tip, one can determine viscosity. For more complex viscoelastic materials, it is even possible to find components of the relaxation spectrum (though without close relation to particular rheological model [47-49].

4.3 Indentation of viscoelastic solids.

An approach to the modeling of indentation of viscoelastic solids has been developed from the theory of elastic solids. It is based on the works of Lee[11,16], Radok[9] , Sneddon [7] and others[12-15,17], and has been further developed and practically applied by Sakai et. al. to viscoelastic solids [1-6]. We make use of Sakai's approach here.

Hook's law for elastic materials in terms of Poisson ratio, Young's modulus, infinitesimal strain and stress is expressed as:

$$d\bar{\sigma} = \frac{E}{(1-\nu^2)} d\bar{\varepsilon} \quad (4.31)$$

where:

σ – stress

ε – strain

ν – Poisson ratio

E – Young's modulus

During indentation, assuming the Poisson ratio coefficient to be constant, but Young's modulus a function of time,

$$d\bar{\sigma} = \frac{1}{(1-\nu^2)} E(t-t') d\bar{\epsilon}(t') \quad (4.32)$$

Then the total indentation force as a function of time can be found by integrating with respect to t' from $t'=0$. A simple solution can be obtained for constant rate indentation in the form:

$$P(t) = C \int_0^t E(t-t') \left(\frac{d\{h(t')^n\}}{dt'} \right) dt' \quad (4.33)$$

where C and n are geometrical factors which can be specified for indenters of various shapes.

This formula in theory can be applied to both viscoelastic liquids and viscoelastic solids, although it does not work well for liquids.. Viscoelastic properties are represented by the introduction of a relaxation modulus. The relaxation modulus can be modeled with a series of Maxwell elements (generalized Maxwell formula).

$$E(t) = \sum_{i=1}^m E_i \exp\left(-\frac{t}{\tau_i}\right) \quad (4.34)$$

In some cases viscoelastic materials, such as monodispersous polybutadiene, exhibit relatively simple behavior when subjected to stress. Such materials and can be represented with single Maxwell element. Then we have Equation 4.35 for viscoelastic liquids and Equation 4.36 for viscoelastic solids:

$$E(t) = E_0 \exp\left(-\frac{t}{\tau}\right) \quad (4.35)$$

$$E(t) = E_0 \exp\left(-\frac{t}{\tau}\right) + E_e \quad (4.36)$$

This particular approach seems to be applicable to stiff materials with distinguishable elastic properties. Another advantage is that analytical solutions exist for various indenter shapes: flat-end, spherical, conical and, by similarity with conical for various pyramidal indenters. However, it is less suitable for low viscosity liquids since it only includes the compression forces and does not account for shear stresses.

4.4 Combining approaches for viscoelastic liquids and viscoelastic solids.

Some viscoelastic liquids (for example, Polybutadiene), have also significant Young's modulus. To model the response of such materials, we suggest combining our approach for viscoelastic liquids with the described above theory for viscoelastic solids. Then the compression force is calculated from the Sakai's formulae 4.33 and the other forces – shear, surface tension and buoyancy can be found from Equations 4.10, 4.23 and 4.24.

Chapter 5.

Numerical simulation of viscous flow around an indenter.

5.1 Objectives of the numerical simulation.

Viscoelastic liquids, like polybutadiene, exhibit behavior similar to a highly viscous fluid under normal conditions. For these materials, as a first step towards understanding their behavior, an indentation can be considered as a viscous flow around a solid indenter. The goal of the numerical modeling is to simulate this unsteady flow by solving the Navier-Stokes equations. Here the indentations of polybutadiene are modeled using the FLUENT commercial software. The geometry of the problem and the mesh structure was produced by Gambit mesh generator. First the steady-state flow around a fully submerged sphere was modeled to validate the chosen approach and the problem setup. Then, the actual indentation was simulated as an unsteady two-phase flow. In the following sections the results of those simulations are presented and discussed.

5.2 Modeling of the Stoke's problem.

The first step for creating a numerical model was to simulate the flow of a highly viscous liquid around a fully submerged sphere. Because of the small indentation rate (10^0 - 10^2 micrometers per second), the small size of the indenter (from nano- to micrometers) and a very high viscosity (the zero-shear viscosity of the Polybutadiene is $\mu_0 \approx 37000 \text{ Pa} \cdot \text{S}$), the flow under consideration has a very low Reynolds number:

$$\text{Re} = \frac{V \cdot d}{\mu / \rho} \ll 10^{-2}, \quad (5.1)$$

This suggests that such a flow may be very similar to ideal creeping flow. Stoke's theory of an ideal flow was developed for a sphere that moves in an infinite volume of liquid, as shown in Figure 4.1

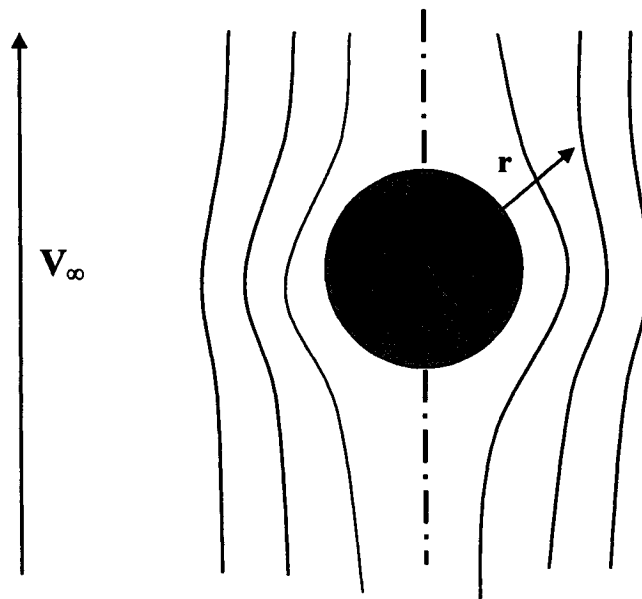


Fig.4.1 Stoke's flow

In reality, the size of the sample under investigation is usually thousands of times larger than the size of the indenter. The finite volume method involves integration over a finite region, therefore, the first task is to choose the proper geometry and boundary conditions for the numerical model.

5.3 Problem formulation.

In our numerical work we considered a flow inside a cylindrical enclosure with moving boundaries, around a completely submerged sphere as a model for Stoke's ideal flow around a sphere.

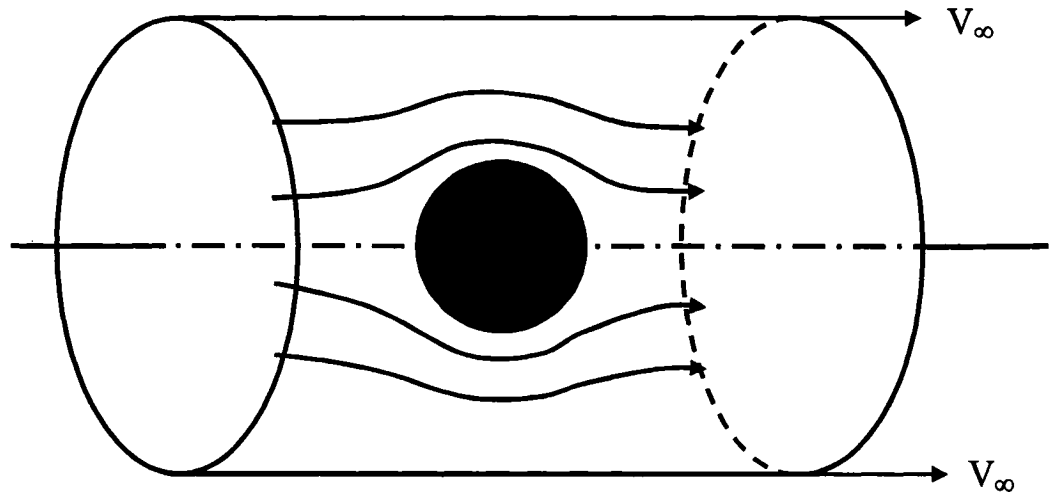


Fig. 5.1 Model geometry for flow around a sphere.

The first task was to determine the minimum dimensions of the area, relative to the size of the spherical indenter, which allows one to accurately simulate the motion of an infinite fluid. We did this by comparing the results to Stoke's solution. The problem set up is shown in Figure 5.2.

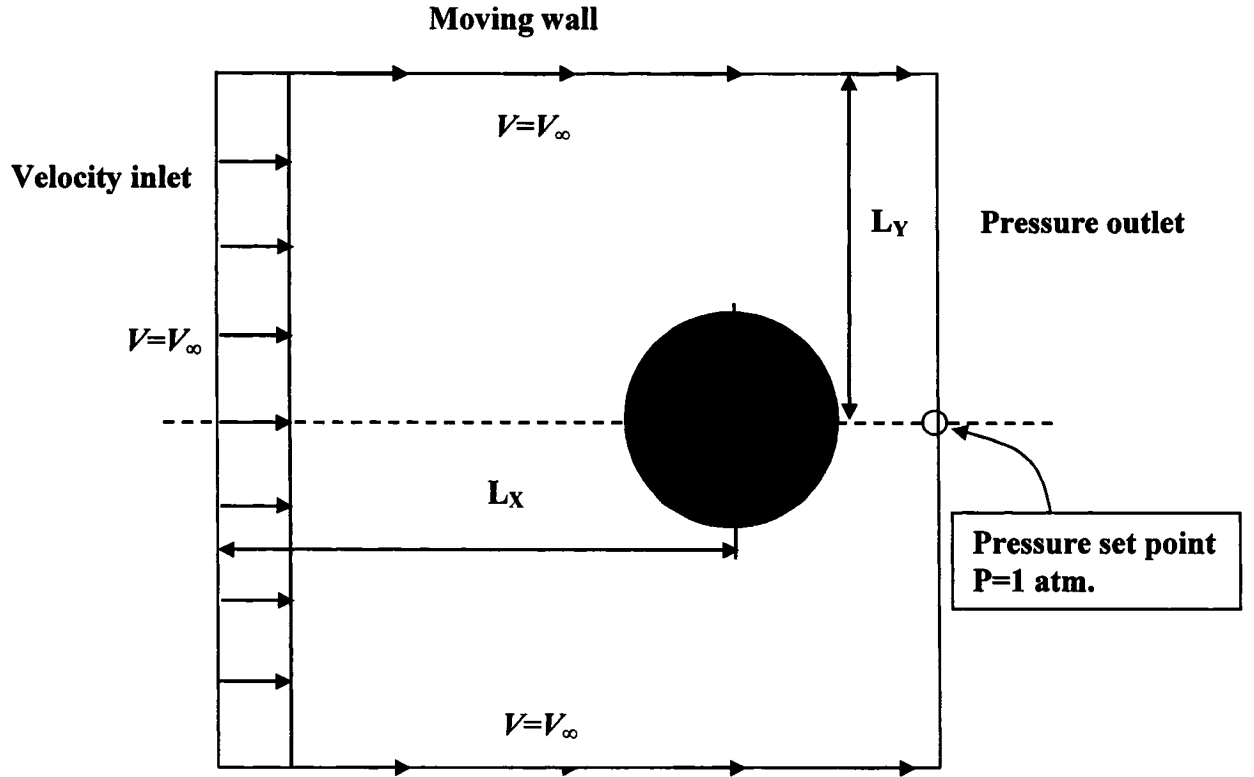


Fig.5.2 Problem set-up for creeping flow around a sphere.

From Stoke's theory all components of the velocity can be expressed as functions of distance from the center of the sphere and the angle from the z-axis in the spherical system of coordinates.

$$v_r = v_\infty \left(1 - \frac{3}{2} \left(\frac{R}{r} \right) + \frac{1}{2} \left(\frac{R}{r} \right)^3 \right) \cos(\theta) \quad (4.2)$$

$$v_\theta = -v_\infty \left(1 - \frac{3}{4} \left(\frac{R}{r} \right) - \frac{1}{4} \left(\frac{R}{r} \right)^3 \right) \sin(\theta) \quad (4.3)$$

$$v_\phi = 0 \quad (5.1)$$

These equations are discussed in detail in Section 4.1. Then the magnitude of the velocity is:

$$|v| = v_{\infty} \sqrt{\left(1 - \frac{3}{2}\left(\frac{R}{r}\right) + \frac{1}{2}\left(\frac{R}{r}\right)^3\right)^2 \cos^2(\theta) + \left(1 - \frac{3}{4}\left(\frac{R}{r}\right) - \frac{1}{4}\left(\frac{R}{r}\right)^3\right)^2 \sin^2(\theta)} \quad (5.2)$$

The ratio $|v|/|v_{\infty}|$ can be a measure of the magnitude of the disturbance of the flow, produced by the sphere. At the radius r , where this ratio is close to 1 at all angles (θ) , the distance from the center of the sphere is considered to be sufficient to reach undisturbed flow where the velocity is simply V_{∞} .

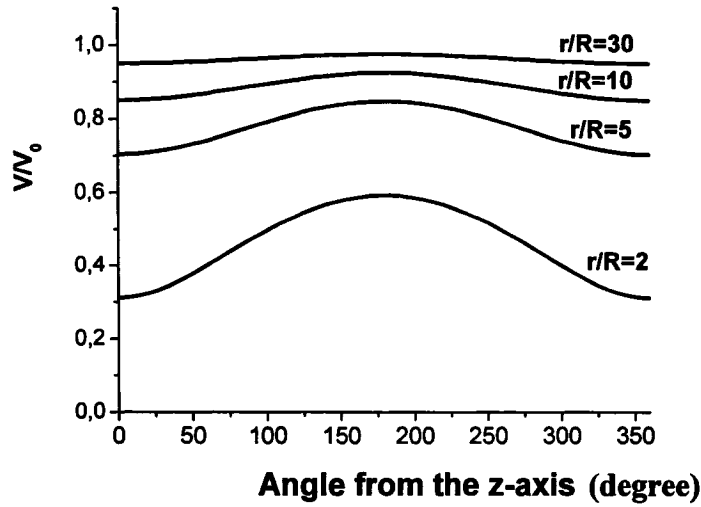


Fig. 5.3 Velocity magnitude ratio as a function of θ for fixed r/R ratio.

From the Fig. 5.4 we conclude that the ratio $\frac{L_x}{R} = 30$ is expected to be sufficient for adequate modeling of Stoke's Ideal flow.

We assume that the viscous flow is axisymmetrical. A flow around a round axisymmetric indenter (for example of a conical or a spherical shape) is three-dimensional in the Cartesian system of coordinates, but it turns into a two-dimensional problem in the

cylindrical system of coordinates. In our model the tip is considered to be motionless. It is placed at a fixed location on the axis of symmetry and the indentation is simulated by the motion of the fluid. The boundary conditions and problem formulation are shown in Figure 5.4:

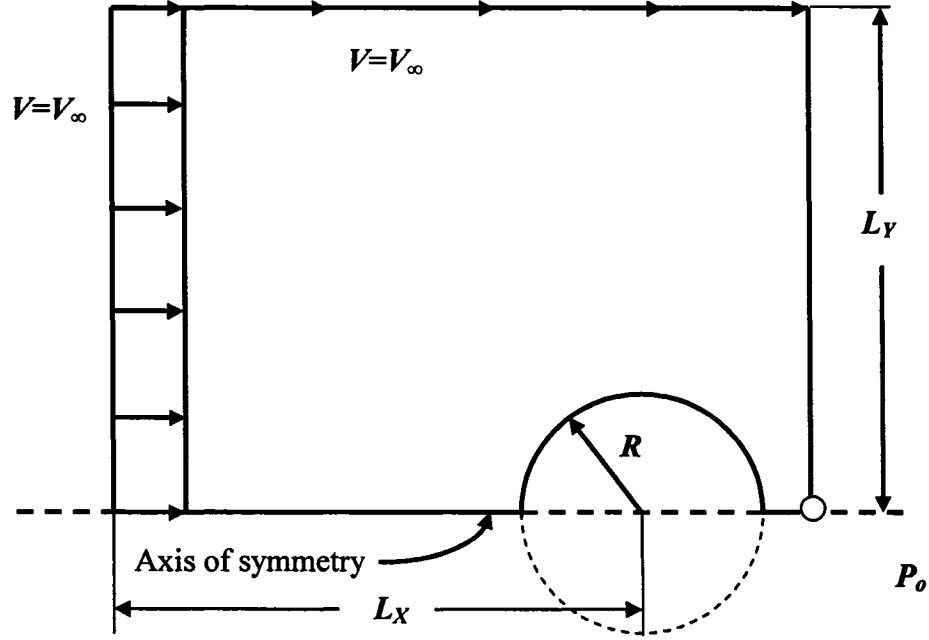


Fig.5.4 2D problem formulation and boundary conditions in cylindrical system of coordinates.

Note that the indenter is stationary and fluid is moving with a velocity $V = V_{INDENTATION}$ at a distance X from the indenter.

Results of the numerical simulation of this problem were compared with the analytical solution for the ideal (Stoke's) flow. The criteria for similarity was the agreement between shear and compression forces predicted by Stoke's theory and the results of the numerical solution. The graphical representation of the results of numerical simulation is shown in Figures (5.5-5.7).

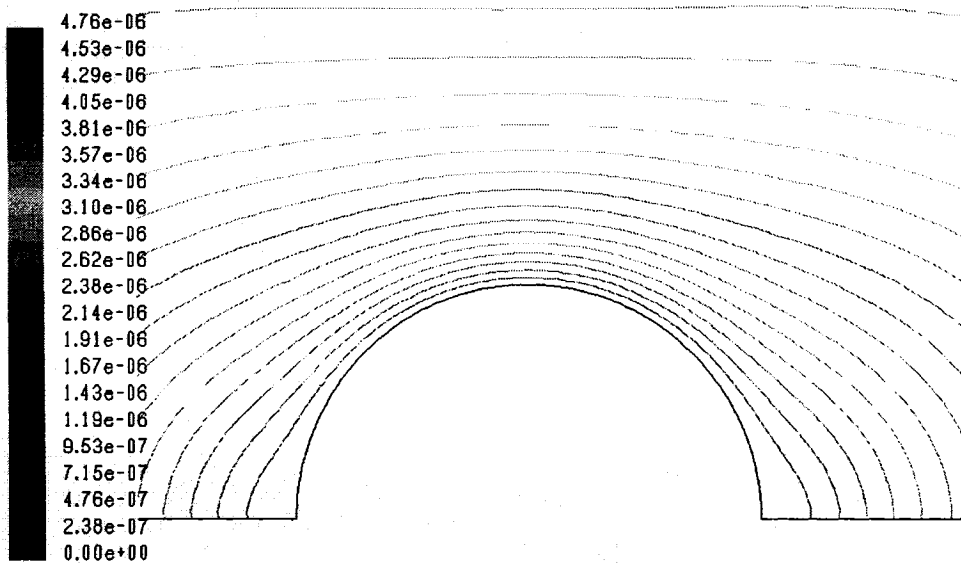


Fig. 5.5 Velocity magnitude isolines for simulated creeping flow around a sphere.

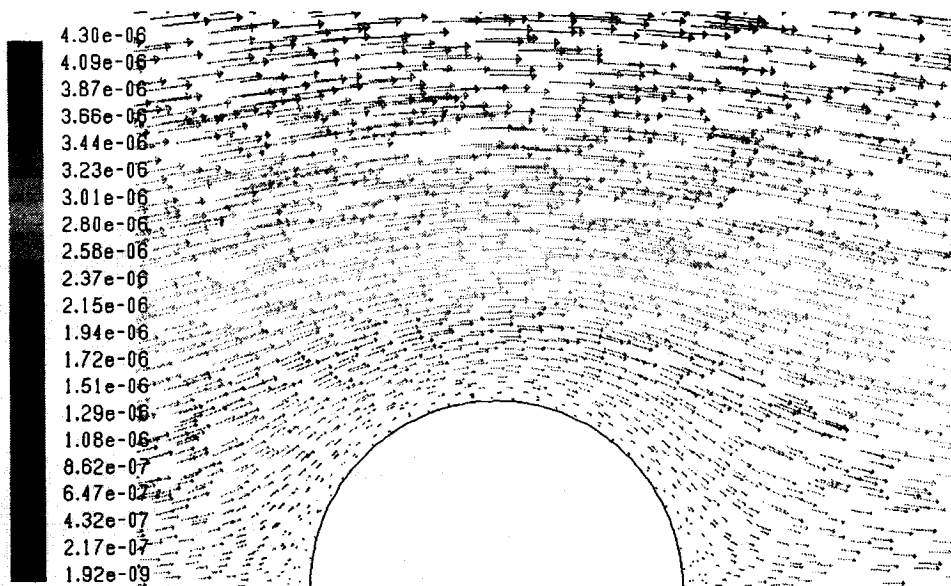


Fig. 5.6 Velocity vector field for simulated creeping flow around a sphere.

From Figure 5.6 we can clearly see that the modeled flow is a slow laminar one.

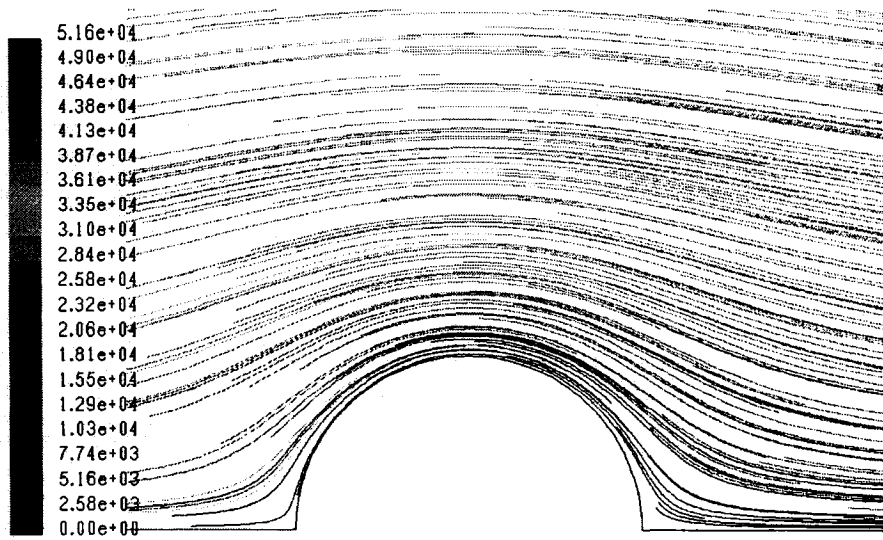


Fig. 5.7 *Particles path lines Velocity vector field for simulated creeping flow around a sphere.*

A quantitative comparison of the output from the numerical simulation with the Stoke'e creeping flow theory can be done via the velocity fields. For a 2D graph illustration we will compare velocity magnitudes along two selected lines – an axial line passing through the sphere in the flow direction and a line directed at 45° angle toward the flux. (See Figure 5.8)

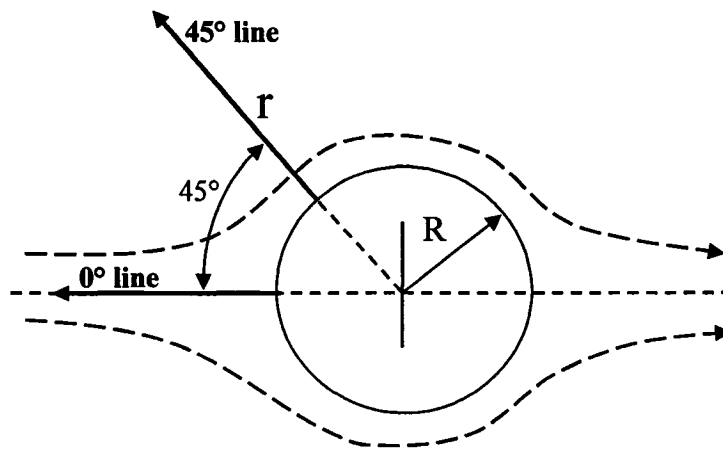


Fig. 5.8 *Selected lines for velocity profile comparison.*

The result of comparison is shown in Figures 5.9 and 5.10.

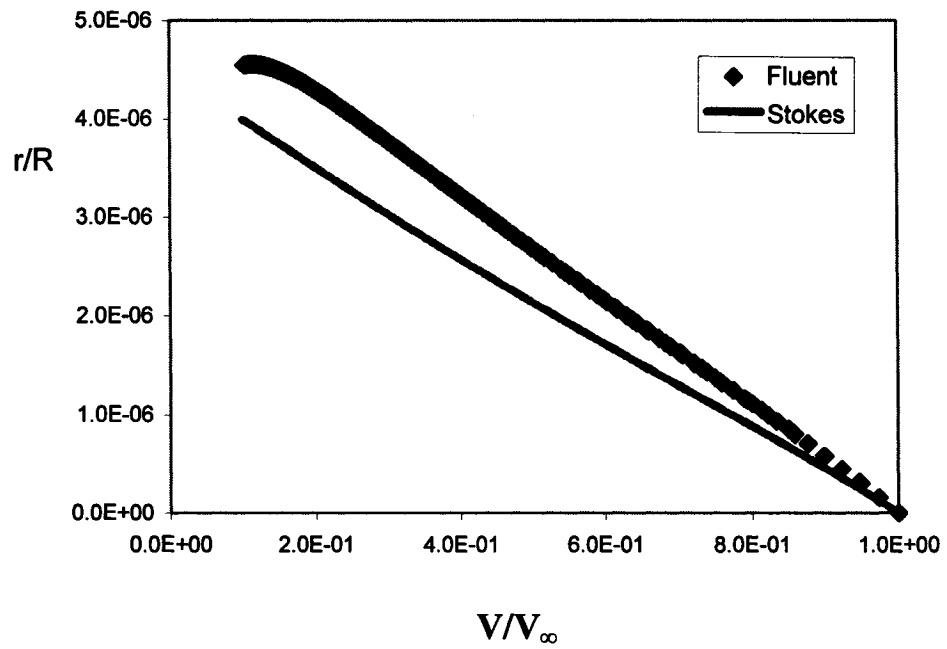


Fig 5.9 comparison at 45 degrees.

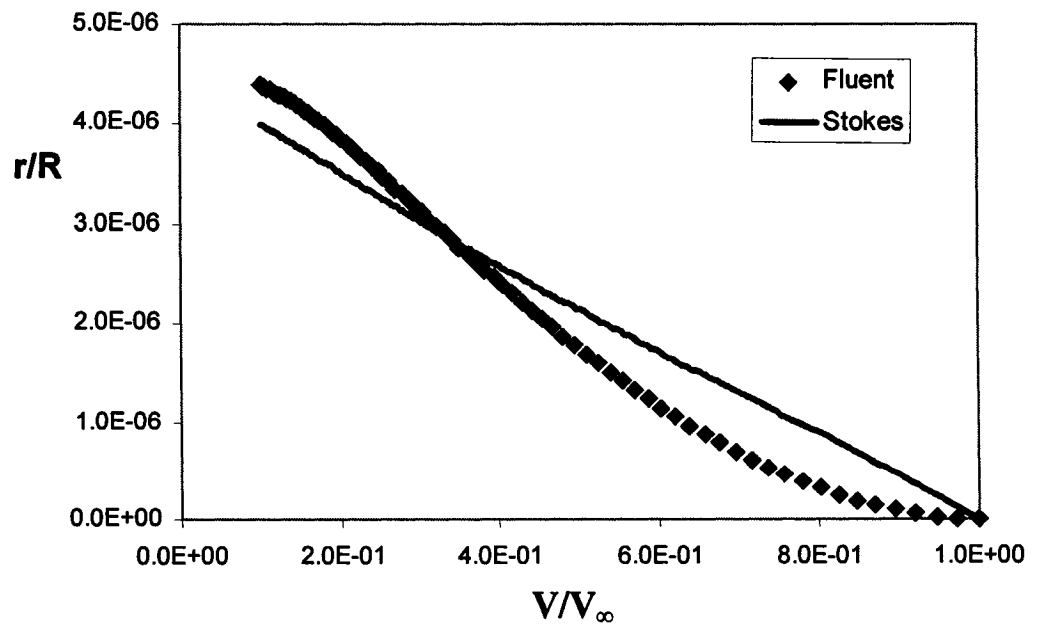


Fig 5.10 comparison at 0 degrees.

Values of compression and shear forces, obtained by numerical simulation, were compared with the drag force, calculated from Stoke's formula:

$$F_{DRAG} = 6\pi\mu V_{\infty} R \quad (5.3)$$

The calculation was performed for the following conditions:

$V_{\infty} = 4.5\mu\text{m/s}$, $\mu = 37000 \text{ Pa}\cdot\text{s}$, $R = 8 \mu\text{m}$ and $Lx/R = Ly/R = 10$ the error was about 8.95 % in the total force.

Table 5.1 Comparison of analytical and numerical solutions for Stoke's flow.

	Shear forces (N)	Compression forces(N)	Total Force (N)
Stoke's formulas	1.924E-5	0.962E-5	3.17E-5
Numerical modeling	2.15E-5	1.03E-5	2.88E-5
Deviation (%)	10.5	5.035	8.95

These results indicate indicates that that the flow is similar to the ideal one and that our problem has been correctly formulated. We decided, however, to adjust the geometry of the model for future calculations and the ratios Lx/R , Ly/R were increased up to 30. We expect this to reduce the error proportionally and especially to increase the accuracy of the simulated velocity field.

5.4 Modeling of the indentation.

The next step was the numerical simulation of the dynamics of the actual indentation process. The problem was set up as an unsteady two- phase flow, where one phase had a high viscosity and density (as polybutadiene). This phase represents the investigated material. The second phase has a low viscosity and density and represents the ambient air. One of the biggest challenges here is the appearance of vortices in the air, especially at the first stages of the indentation. During the indentation, as the polymer fills the narrow gap between its surface and the indenter the air is forced out of the gap with a speed that is higher than the speed of the indentation. This high speed flux, directed at sharp angle toward the direction of the indentation causes separation of streamlines and creates vortices (Figure 5.12).

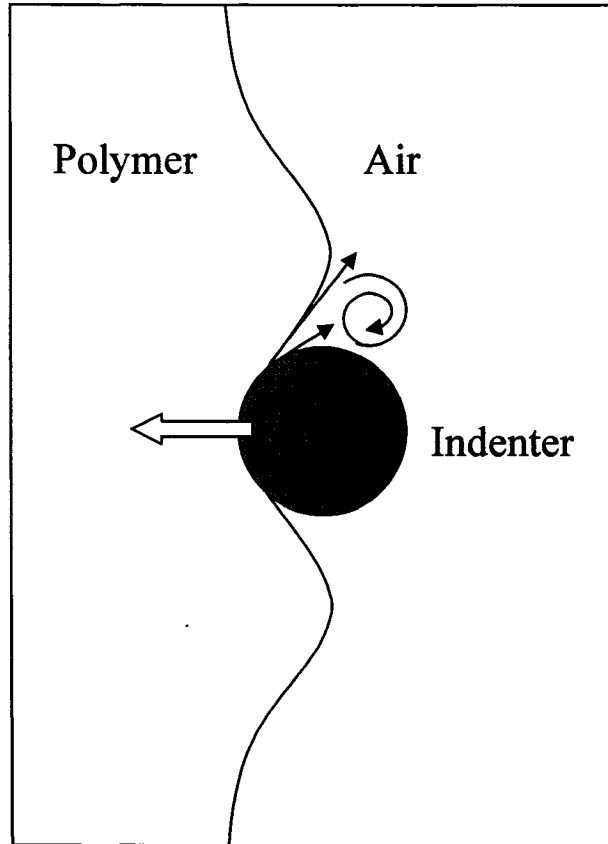


Fig.5.12 Vortex formation in an indentation simulation.

Such vortices can separate from the point of their origin, grow and move along the phase interface to peripheral regions where the mesh is coarse. That makes the numerical solution unstable.

We found an effective method to overcome this problem. The viscosity of the air is artificially increased to 10^{-3} - 10^{-2} Pa·s to make the solution stable at reasonably large time steps. Generally, this might increase the drag force, especially at small depths of indentation. However, the viscosity of the air is still several orders of the magnitude smaller than the viscosity of the polymer phase and should not have a significant impact on results of the computation. In order to validate this assumption, we compare results of

two numerical experiments: the first experiment was a simulation of the indentation with the minimal viscosity of the gas phase required for stability: 10^{-3} Pa·s. After that the viscosity of the air was increased by another order of magnitude, up to 10^{-2} Pa·s. The results of these two computations are compared in Figure 5.16.

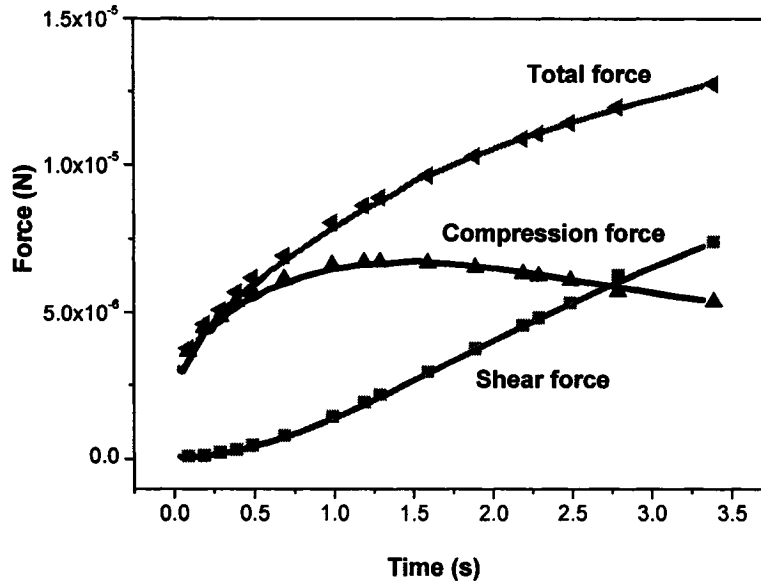


Fig.5.13 Results of simulations: Forces acting on indenter. Symbols are results of simulations with air viscosity set to 0.001 Pa·s and lines those with air viscosity set to 0.01 Pa·s.

Theses results show that there is no significant increase of the compression and shear forces when the air viscosity is increased and proves that the applied method of stabilization is valid.

Results of the two-phase indentation model are shown in Figures 5.14 and 5.15. All results are given for simulation of indentation of Newtonian fluid with a spherical indenter. The parameters were chosen to match an experimental indentation: viscosity of

the investigated material $\mu=37000 \text{ Pa}\cdot\text{s}$, indentation velocity $V_{\infty}=4.5\mu\text{m/s}$ and radius of the indenter $R=8\mu\text{m}$. The data shown here are for the moment in time 0.627 seconds from the beginning of the indentation. The phase profile at that moment is shown in Figure 5.14.

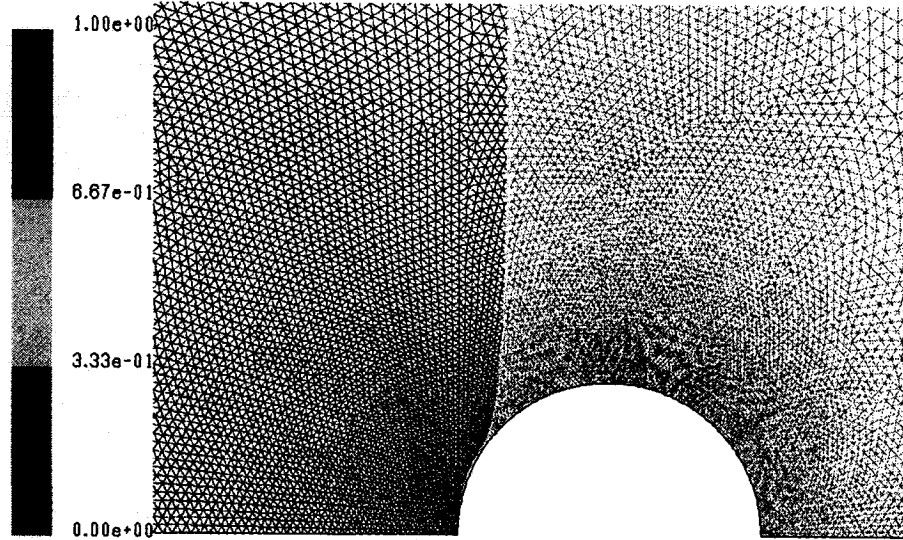


Fig. 5.14 Phase profile at 0.62715 sec of indentation.

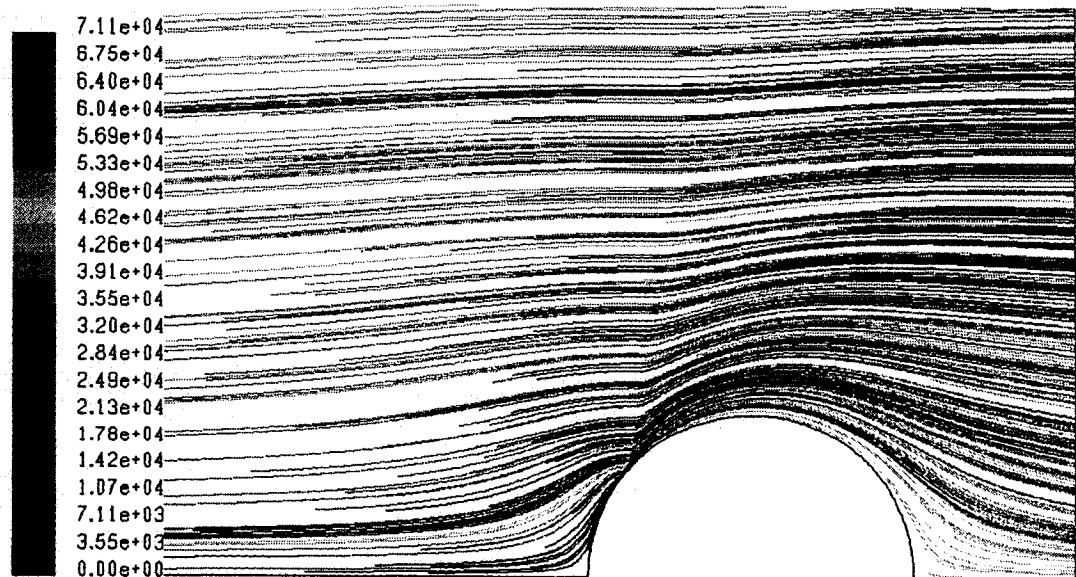


Fig. 5.15 Particle pathlines.

5.5 Mesh independence.

In order to verify mesh independence we used meshes of 3-node triangular elements of different densities. We are mostly interested in the processes and parameters in close proximity to the surface of the indenter. Therefore, the mesh was made the most dense around the indenter and it exponentially coarsened toward the peripherals. The surface of the indenter was chosen as a base for the meshing and the nodes on the indenter are evenly distributed. In the mesh independence study, the number of nodes on the indenter surface was decreased by 30% and the results of the calculations with the course and the fine meshes are shown in the Figure 5.16. The similarity of the results proves mesh independence for our model.

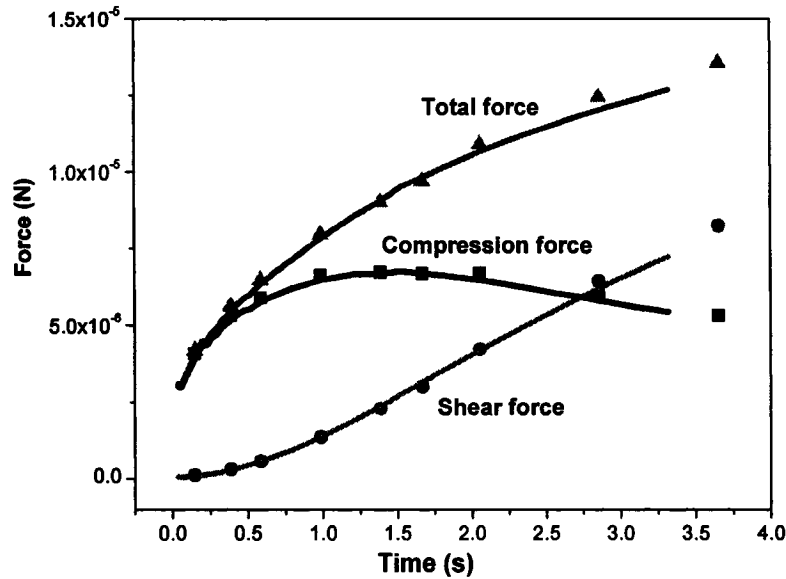


Fig.5.16 Comparison of simulation results with original and coarsened mesh. Symbols represent results from coarse mesh and line represent results from fine mesh.

$$R=8\mu\text{m}, V=4.5\mu\text{m/s}, \mu=37000\text{ Pa}\cdot\text{s}.$$

5.6 Contact Depth during an indentation.

An interesting observation was made about the shape of the polymer/air interface during the simulation of constant rate indentation with a spherical indenter: the contact depth of the indentation, h_c , was found to be different from the total indentation depth, h_{ind} , as shown in Figure 5.18

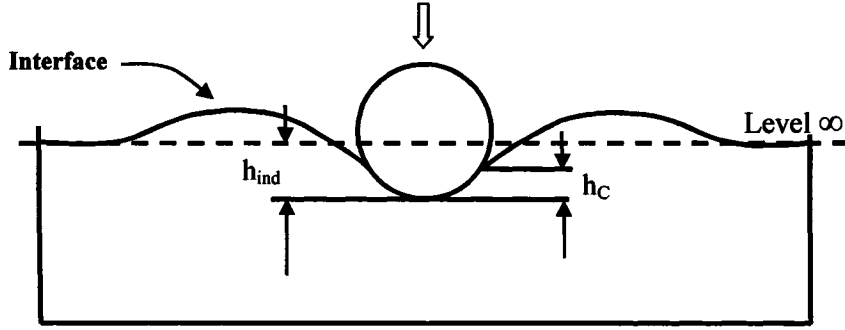


Fig.5.17 Interface distortion during indentation.

In the case of a purely elastic material, the ratio, h_{IND}/h_c depends only on the shape of the indenter. Analytical solutions by Hertz and Love show that for spherical indenters $h_{IND}/h_c=2$ and for conical indenters $h_{IND}/h_c=\pi/2$. Later this was applied by Sakai [1-6] to axisymmetrical pyramidal indenters through the similarity principle.

For low-viscosity liquids we expect h_c to be close to h_{IND} : $h_{IND} \sim h_c$. Our numerical simulations show that for highly viscous fluids generally $h_{IND} > h_c$. The contact depth during indentation is an important parameter because it determines the true indentation depth and the contact area which is important in the stress calculation. In order to establish the correlation between (h_{IND}/h_c) and other indentation parameters we conducted a series of numerical experiments. In these experiments we simulated

indentation with spherical indenters of different sizes, indentations with different rates, and for liquids of different viscosities. These results are shown below. The dimensionless ratio h/h_c was plotted vs. dimensionless time $Time/(R/V_\infty)$ where (R/V_∞) is time that takes for a sphere with a radius R to be displaced to a depth of one radius with the indentation speed V_∞ .

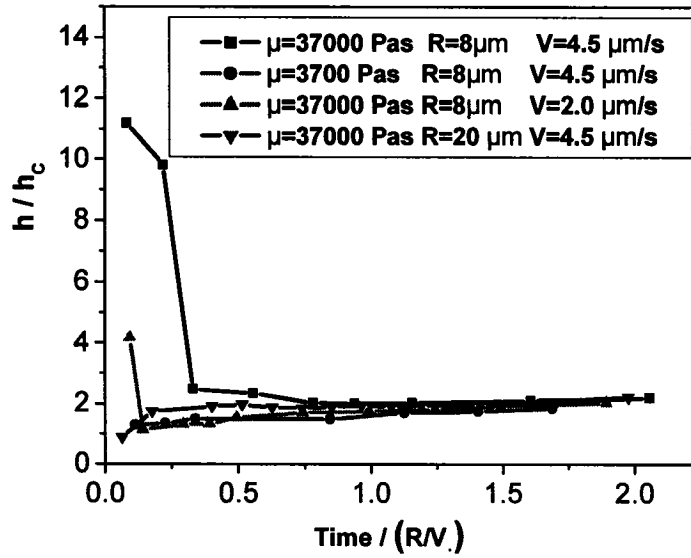


Fig. 5.18 Contact depth/indentation depth ratio for viscous liquid indentation.

The results of the simulations showed that after a short start-up period, when the process is established, the ratio between the depth of the indentation h_{IND} and the contact depth h_c tends to 2.

$$\frac{h}{h_{IND}} \rightarrow 2 \quad (5.4)$$

This behavior is typical for indentations of liquids with different but high viscosities, different rates of indentation and different sizes of the indenter. That is similar to Hertz's analytical solution for an indentation of purely elastic material, though this result is

actually obtained for viscous liquids using the fluid mechanics approach. In the next chapter we will make use of Equation 5.4 in the development of the procedure for interpreting experimental data of viscoelastic liquids.

5.7 Results of modeling.

In the nanoindentation experiments the following sequence of steps is performed: First the indenter is placed on the surface of the material under investigation. At that point a small contact force is applied to ensure a reliable contact. In case of testing a liquid, like polybutadiene, this contact force causes a slow creep of the indenter into the material. Therefore, by the time the actual indentation experiment starts, the indenter is partly submerged to a small depth. In order to simulate this real life situation, with spherical indenters in each case we assumed an initial contact depth of 1% of the radius of the indenter. Therefore the compression force at the very beginning of the indentation is non-zero but starts at some value, depending on the shape of an indenter, the properties of the material and the indentation rate.

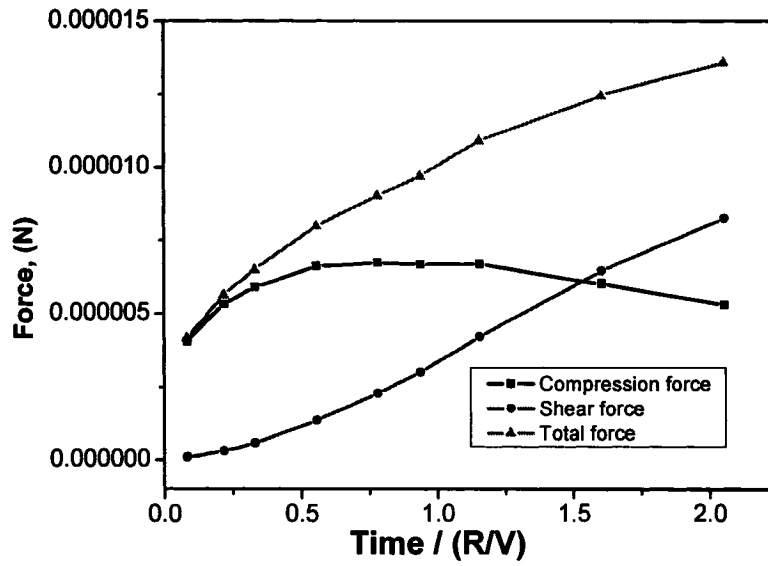


Fig.5.19 Indentation with parameters: $\mu=37000 \text{ Pa}\cdot\text{s}$ $R=8 \mu\text{m}$ $V=4.5 \mu\text{m/s}$.

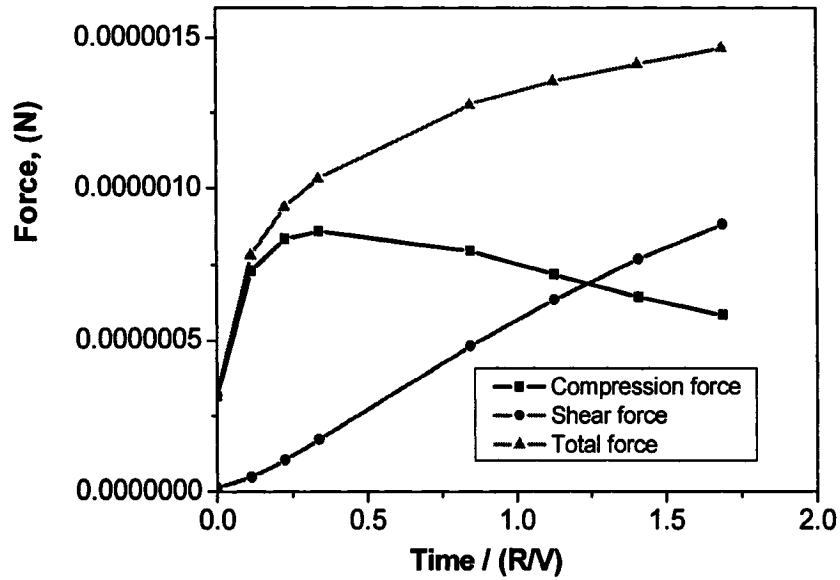


Fig.5.20 Indentation with parameters: $\mu=3700 \text{ Pa}\cdot\text{s}$ $R=8 \mu\text{m}$ $V=4.5 \mu\text{m/s}$.

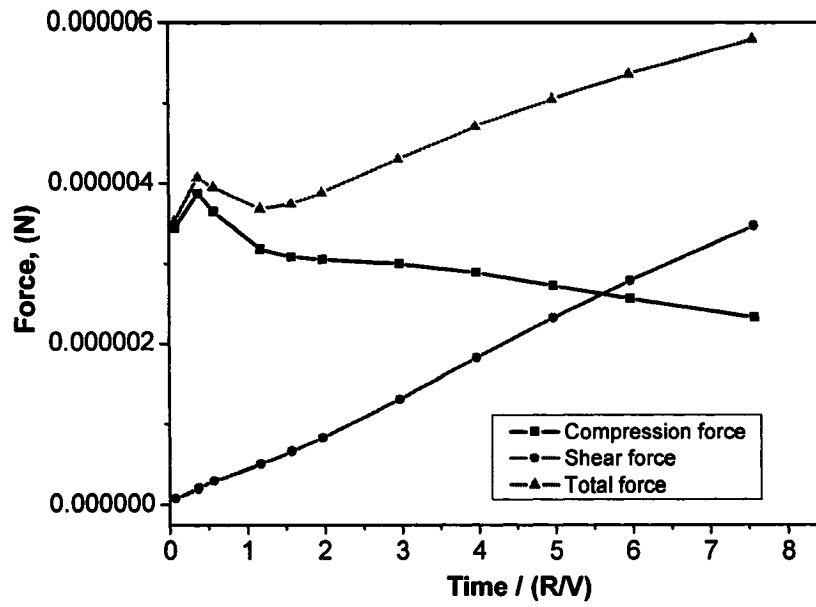


Fig.5.21 Indentation with parameters: $\mu=37000 \text{ Pa}\cdot\text{s}$ $R=8 \mu\text{m}$ $V=2 \mu\text{m/s}$.

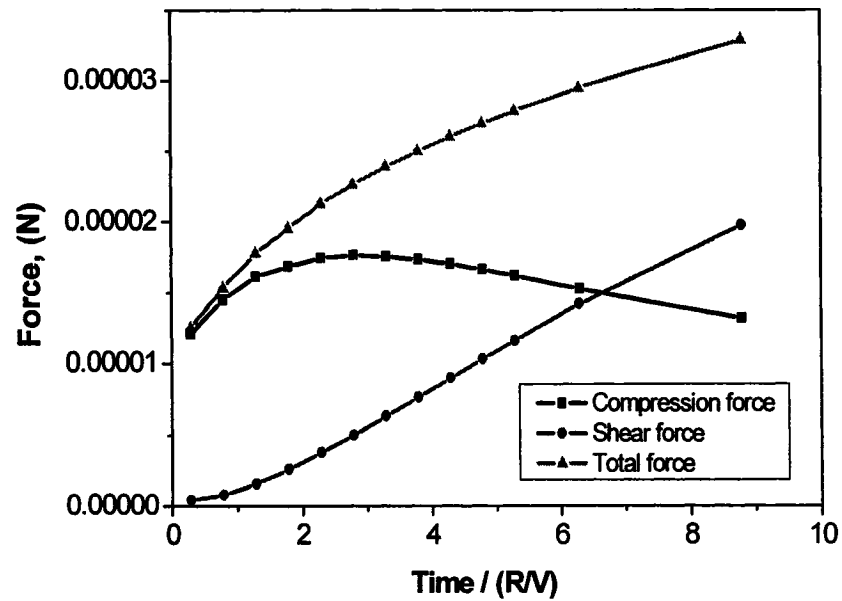


Fig.5.22 Indentation with parameters: $\mu=37000 \text{ Pa}\cdot\text{s}$ $R=20 \mu\text{m}$ $V=4.5 \mu\text{m/s}$.

We can see that behavior of the compression and shear forces is slightly different from that predicted by the physical model discussed in the previous chapter. The compression force increases at first, but later its growth rate slows, it reaches a maximum and begins to decrease (Figures 5.19-5.22).

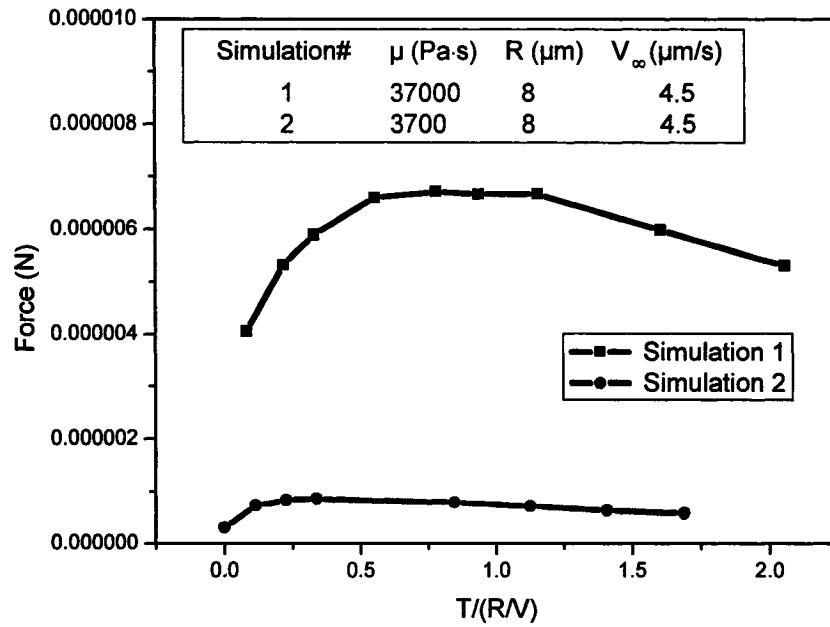


Fig. 5.23 Compression force curve for different viscosities.

This is especially visible at the smaller indentation rates and the larger indenter radii (Figure 5.21, 5.22). The shear force behavior is closer to the expected one. It grows continuously within the chosen time period, which is approximately time of submergence $h_c=R$ for each numerical experiment (Figure 5.19-5.22, 5.24).

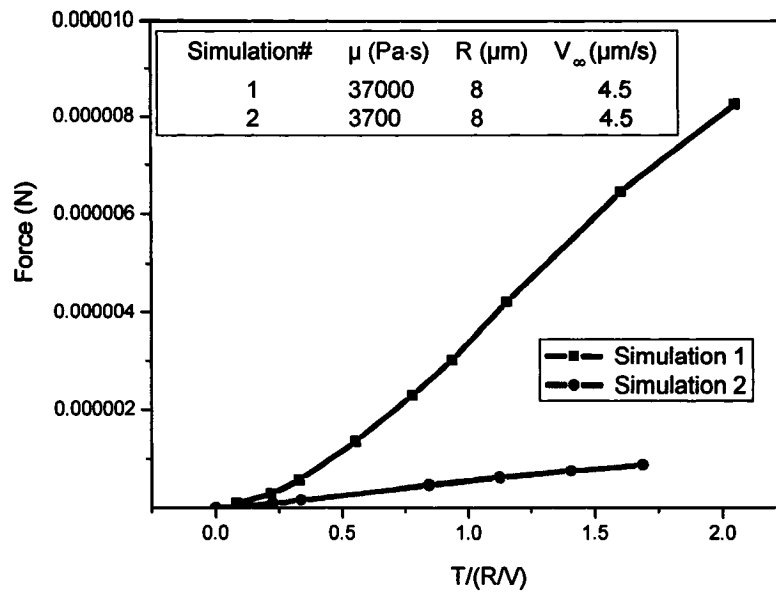


Fig. 5.24 Shear force change for different viscosities.

This can be explained by the fact that the indentation process is not quite at steady state. Despite the high viscosity of the polymer, the velocity distribution significantly changes during the indentation. Velocity gradients around the indenter surface, that are large at first, decrease in time, affecting the drag force and both local compression and shear components reduce. The observations brings us to the conclusion that even for highly viscous liquids the velocity distribution will be to a certain degree different from the one for the steady-state Stoke's solution. This difference can result in a larger indentation force compared to the indentation force, predicted from the Stoke's approach.

Chapter 6.

Comparison of results and discussion.

6.1 Introduction.

In the course of this work we considered three directions of the research: physical modeling of nanoindentation, numerical simulation of nanoindentation using FLUENT commercial software and experimental studies of viscoelastic materials with both rheological methods and nanoindentation technique.

In this chapter we compare results from the theoretical modeling of nanoindentation with the output of numerical simulation and the experimental data. We also compare bulk properties obtained by rheological measurements with local properties, measured by nanoindentation technique. This comparison allows us to evaluate the validity of suggested approaches and to draw conclusions about the applicability of the selected theories and the accuracy of the applied methods.

6.2 Comparison of theoretical modeling and numerical simulations.

In this part we compare the results from the numerical simulation of the indentation of a Newtonian liquid with properties close those of polybutadiene, with the physical model based on Stoke's creeping flow described in Chapter 4. For a proper comparison we use Formulas 4.17 and 4.26 to calculate the forces acting on a partly submerged sphere, derived in Chapter 4. According to the Stoke's theory,

The compression forces are:

$$F_{COMP} = \frac{\pi\mu\nu_{\infty}h_C(3R^2 - 3Rh_C + h_C^2)}{R^2} \quad (4.17)$$

and the shear forces are:

$$F_{SHEAR}(h) = \frac{\pi\mu\nu_{\infty}h_C^2(3R - h_C)}{R^2} \quad (4.26)$$

The deformation of the polymer/air interface was accounted for by the expression $h=2h_c$, as it was suggested in Chapter 5. This comparison allows us to evaluate the applicability of the Stokes steady-state approach to a transient indentation process for highly viscous Newtonian fluids.

The comparison of the predicted compression and shear forces for indentation of a fluid with a spherical indenter are shown in the Figure 6.2.

The parameters of the indentation are:

Density of fluid: 900 kg/m³

Viscosity: 37000 Pa·s

Indenter radius: 8 μm

Indentation rate: 4.5 μm/s

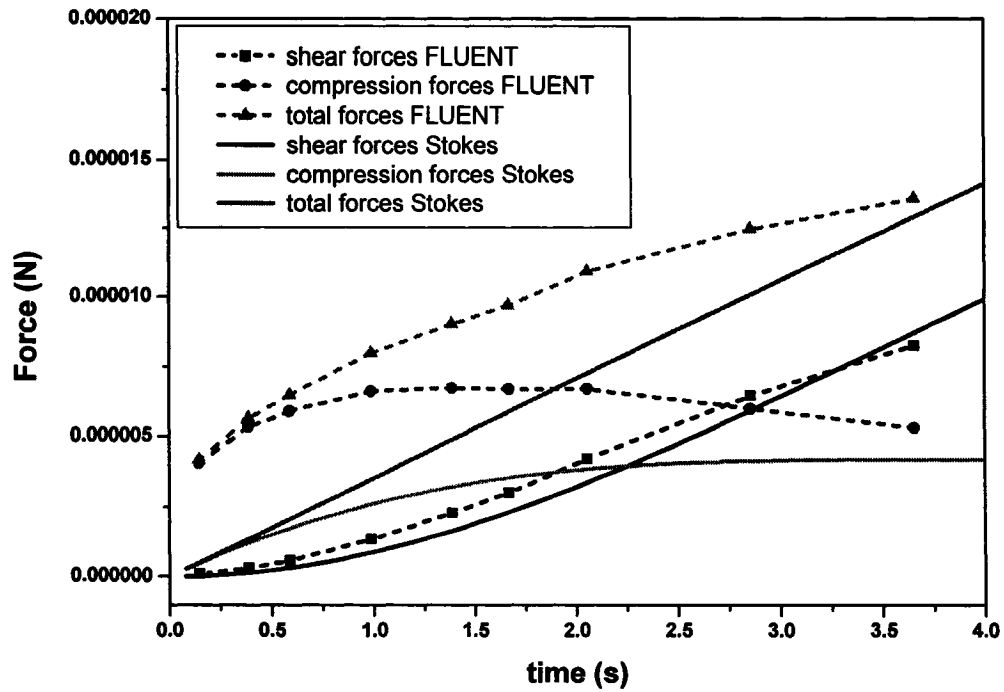


Fig. 6.1 Results of physical and numerical modeling of a nanoindentation of Newtonian fluid.

We can see that the total indentation forces are of the same order of magnitude but still have different values. The total indentation force is the sum of the compression and the shear forces. From Figure 6.1 we can see that these component forces behave differently. The largest difference between the simulation and Stoke's theory comes from the compression forces. Recall that the numerical modeling of indentation was done considering a partly submerged at the start indenter to simulate the real life situation (see Figure 6.2). The initial contact depth of the indenter was set to $0.01 \cdot R$ in the simulation.

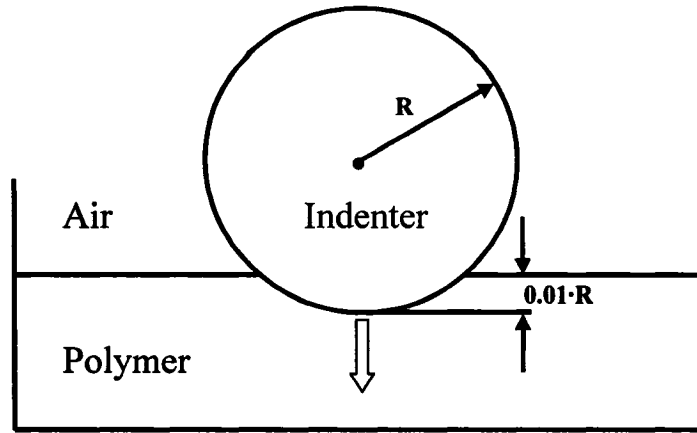


Fig. 6.2 Starting position of the indenter for numerical modeling of indentation process.

The compression force starts with a higher initial value than predicted by formula 4.17. The Stoke's approach suggests that some initial submergence will only result in the shifting of all curves on the time axis. The initial contact depth is only 1% of the radius of the indenter and the time shift for indentation velocity $V=4.5\mu\text{m/s}$ and indenter radius $R=8\mu\text{m}$ will be only 0.018 sec. The high initial value of the compression force can not be explained by this small shift.

This might be explained by the different velocity distribution from the Stoke's steady-state creeping flow given by Equations 4.2 and 4.3. The actual velocity profile might create a large normal stress on the tip of the indenter which can result in significant compression force even at small depths of indentation.

Generally, for a transient process of an indentation with a partly submerged indenter we can expect the velocity distribution will be different from the one for a steady – state Stoke's flow. We can expect higher velocities and, consequently, larger forces, especially for the compression forces due to the inertia component, which is neglected in Stoke's theory. In order to evaluate this difference, we compare the velocity, predicted by

Stokes theory with results of the numerical simulation at one selected point. It is convenient to pick a point on the axis of symmetry in the direction of indentation as shown in Figure 6.3.

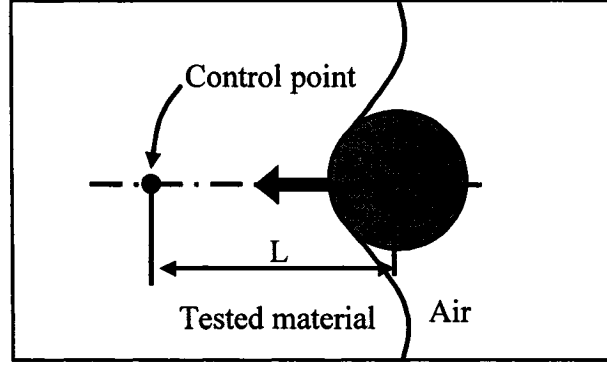


Fig. 6.3 Control point for an indentation with a spherical indenter.

According to the Stoke's theory the velocity on the axis line is:

$$v_r = v_\infty \left(1 - \frac{3}{2} \left(\frac{R}{r} \right) + \frac{1}{2} \left(\frac{R}{r} \right)^3 \right) \quad (6.1)$$

It is important to select a proper location for the control point. If the control point is located too close to the surface of the indenter or too far away, the velocity predicted by numerical simulation will be close to the Stoke's flow as it is enforced by the boundary conditions. Therefore, we place the control point at the distance of $1.65R$ from the center of the sphere. As we can see from the Figure 6.4, the actual velocity magnitude is higher in the beginning of the indentation and asymptotically approaches the Stoke's value.

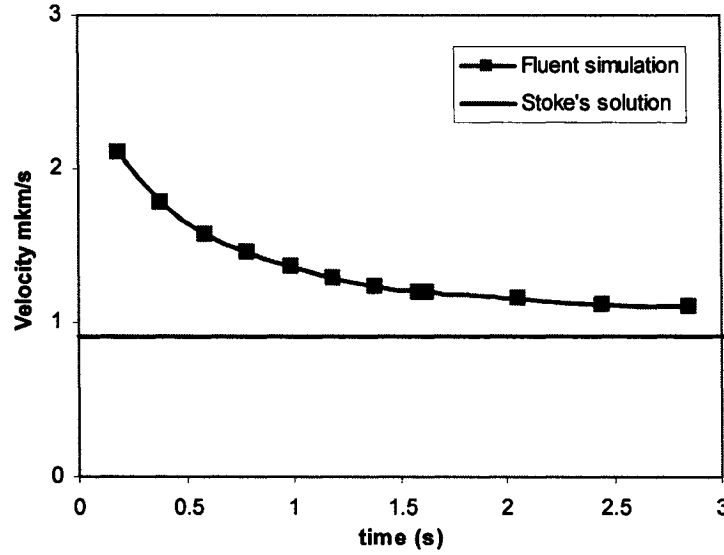


Fig. 6.4 Velocity at the control point from Stoke's theory and numerical simulation.

The behavior of the magnitude of the velocity at the control print is similar to the one, for a potential flow around a sphere of a smaller radius. So, we suggest a modified Stoke's approach to simulate this transient behavior. We introduce a fictitious sphere with an effective diameter, equal to the contact diameter at each time of the indentation $D_e = D_c$, and tangent to the indenter at its lowest point as shown in the Figure 6.5. Then we calculate the velocities for a Stoke's flow around it.

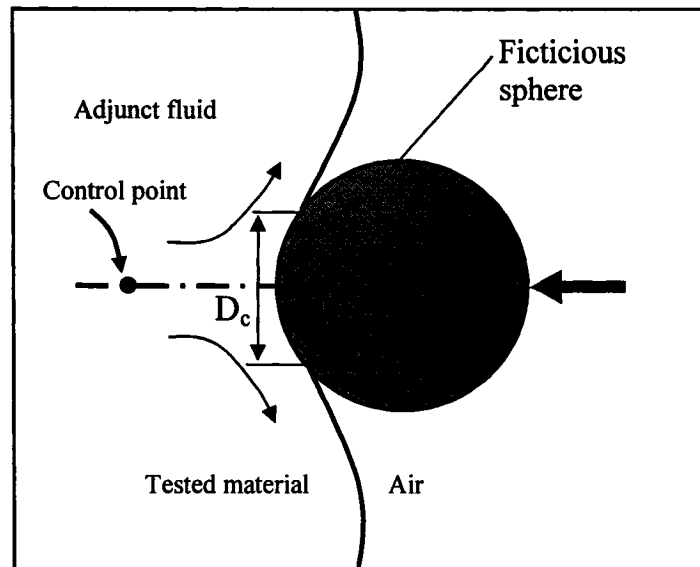


Fig. 6.5 Fictitious sphere.

This approach gives a good agreement with the numerical simulation at the chosen control point (Figure 6.6). Future work involves the derivation of expression for the forces using the fictitious sphere approach.

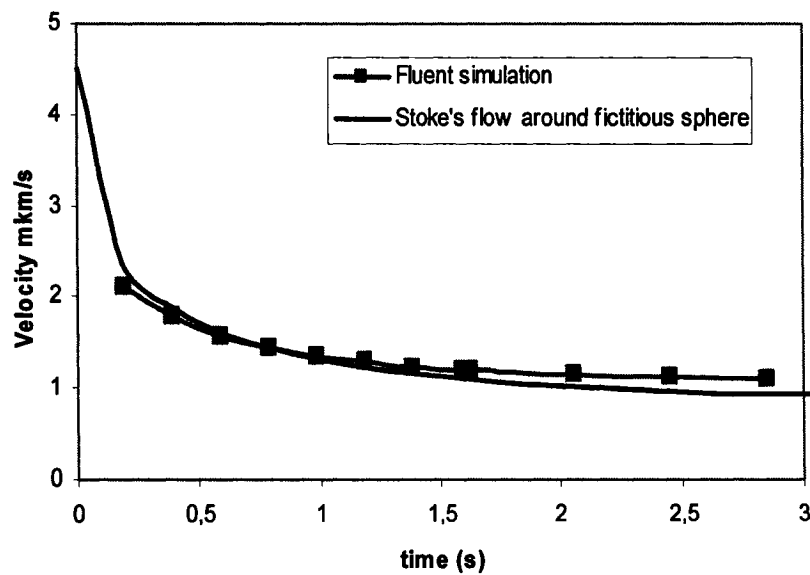


Fig. 6.6 Velocity at the control point from modified Stoke's approach and numerical simulation.

Nevertheless from the Figure 6.1 we can see that the shear force behavior is very similar to that predicted by Equation 4.26. The deviation between the forces, predicted by the Stoke's theory and FLUENT numerical simulation is shown in the Figure 6.7.

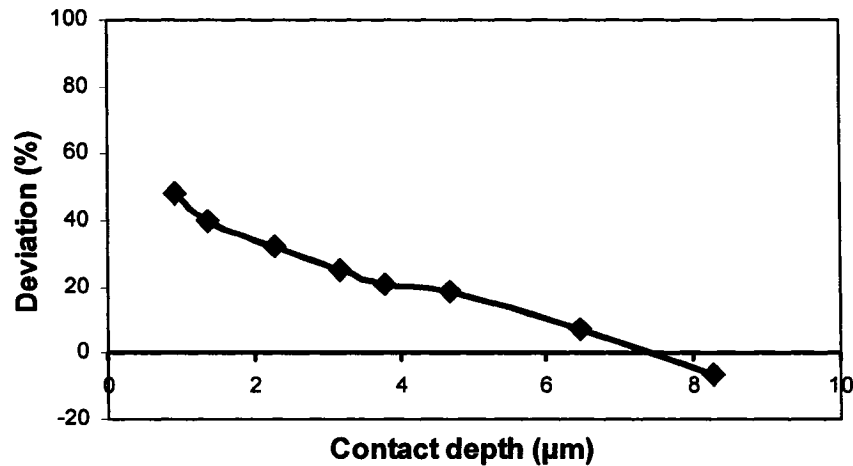


Fig. 6.7 Deviation in predicted shear force.

This indicates that the velocity gradient distribution along the surface of the indenter, in the direction normal to the surface, is close to the one for the steady Stoke's flow.

This brings us to a conclusion that for the testing of viscoelastic liquids with primarily viscous behavior by the nanoindentation technique, the steady-state theory of creeping flow predicts fairly well the shear forces. Therefore, it would be beneficial to use specially shaped tips to minimize influence of compression forces and to emphasize the shear component. One such shape is a flat plate of small thickness (Figure 6.6).

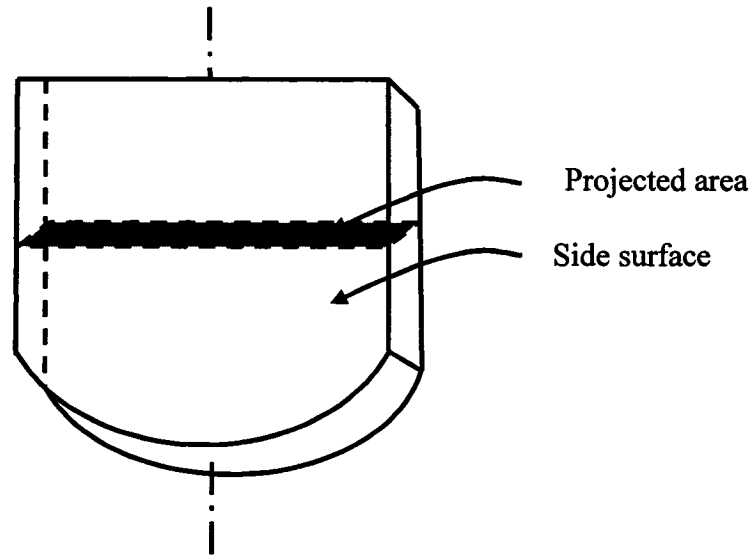


Fig. 6.8 Suggested indenter shape.

The use of such an indenter would also minimize the fluid displacement and therefore reduce the difficulty related to the complex three-dimensional deformation. In this sense a spherical indenter is the worst possible shape since it has the minimum surface area per volume. The shape proposed above keeps the total indentation force high improving the signal for soft materials. Also it allows us to minimize the effect of surface tension.

6.3 Comparison of experimental data with theoretical model.

In this part we compare experimental data from the indentation of polybutadiene with a spherical indenter with a radius of $R=8\mu m$ with the results of the physical modeling.

Here we present two physical models – one of them is solely based on the Stoke's theory.

6.3.1 Model based on the Stoke's theory.

The compression and the shear forces are found from Equations 6.2 and 6.3 accordingly. Since our polybutadiene is monodisperse, (see Figure 3.16), the viscoelastic properties can be rather well represented by a single Maxwell element.

Compression force:

$$F_{COMP} = 3\pi V_{\infty} \eta \int_{\pi}^{\pi-\beta(h)} \left(1 - \exp\left(\frac{R(\cos \theta - \cos(\pi - \beta))}{\lambda V_{IND}} \right) \right) \cos^2 \theta \cdot \sin \theta d\theta \quad (6.2)$$

Shear force:

$$F_{SHEAR}(\theta_{IND}) = 3\pi V R \eta \int_{\pi-\theta_{IND}}^{\pi} \left(1 - \exp\left(\frac{R(\cos \theta - \cos(\pi - \beta))}{\lambda V_{IND}} \right) \right) \cos \theta \cdot \sin^2 \theta d\theta \quad (6.3)$$

The expression for surface tension force was derived from Equations 4.28, 4.29:

$$F_{SURF.TENSION} = 2\pi\gamma\sqrt{2R_L h - h_C^2} \sin(\theta(h)) \quad (6.4)$$

Then the total force of an indentation is the sum of all given components.

We used the known parameters – radius of the indenter, the indentation rate and bulk measured relaxation time were used as constants. The unknown parameter which was determined for the best fit of experimental data (Figure 6.7). The actual indentation force is much larger than predicted by the physical model. The viscosity, found from this model exceeds the bulk one by the factor of 16.

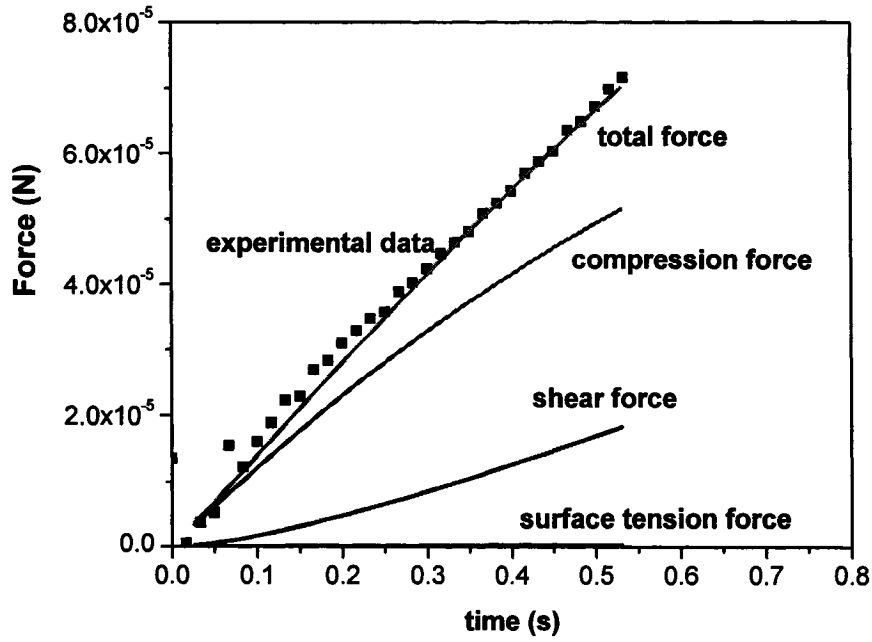


Fig. 6.9 Fit of experimental data VS model based on the Stoke's solution for indentation of polybutadiene.

6.3.2 Combined indentation model.

In the second approach, we combined the model, based on the Snedon and Sakai theory with the one based on the Stoke's theory (Section 4.1) of nanoindentation of viscoelastic liquids (Section 4.3).

$$F(t) = CE_0 \int_0^t \exp\left(-\frac{t-t'}{\tau}\right) \left(\frac{d\{h(t')^n\}}{dt'} \right) dt' \quad (6.5)$$

where:

F - indentation force

C, n - coefficients, depending on the geometry of the indenter

E_0 - Young's modulus

τ - relaxation time

h - depth of the indentation

The bulk rheological properties of polybutadiene show that the relaxation time $\tau=0.06\text{s}$ and the Young's modulus is $E_0=3\eta_0/\tau = 1.77\text{ MPa}$.

The approach of Sneddon and Sakai [1-6], [11-16] does not include the shear force, therefore the shear component was calculated from the Stoke's approach combined with the Maxwell viscoelastic model as described in the section 6.2.1.

This approach gives us better agreement with experiment (Figure 6.10), but it still estimates the local zero shear viscosity four times larger than the bulk value.

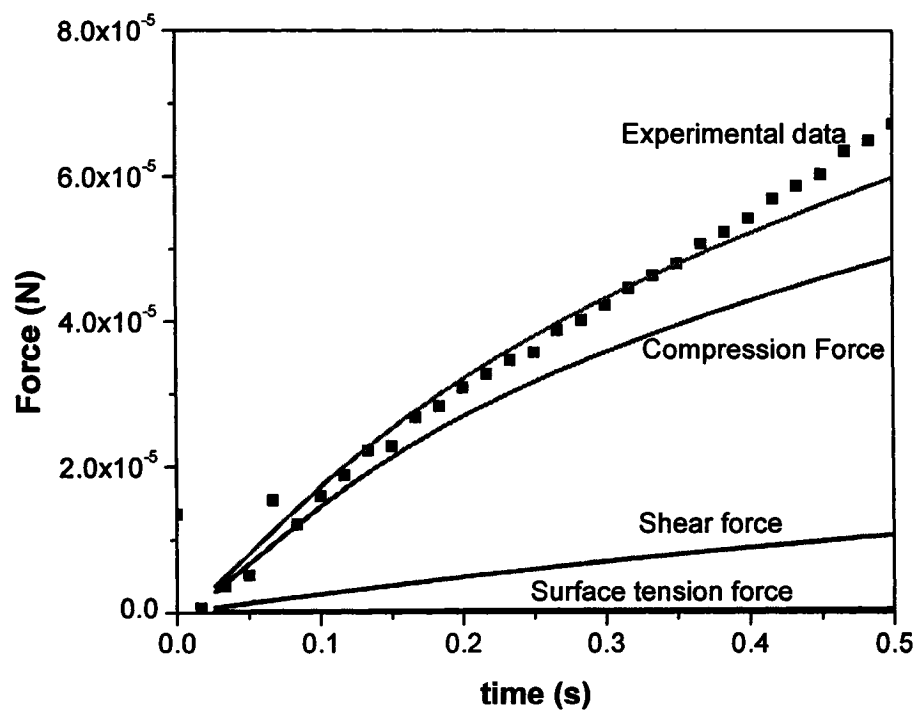


Fig. 6.10 Fit of experimental and theory predicted forces for indentation of polybutadiene.

A possible explanation for this discrepancy is that the properties of polymers on the surface are significantly different from the bulk properties. In a number of recent papers in the field of nanoindentation, Atomic Force Microscopy and nanorheology complex behavior of long-chain liquid or melt polymers has been noted. [47-52]. One of significant factors affecting the indentation process is interaction of indenter with polymer network. The deformations, localized in polymer body around indenter [57], cause changes in existing polymer matrix. It was found that depending on properties of an individual polymers and particularly average molecular weight, at indentation depths of order of 10^1 - 10^2 nanometers significant disentanglement occurs in liquid/melt polymers [49], which greatly increases the indentation energy. However, up to now very little is known about the dynamical behavior of physical entanglement, which makes quantitative estimation of the indentation force very difficult.

6.4 Comparison of experiment data for viscoelastic solid with model.

Results of the nanoindentation tests of the viscoelastic solid, the cross- linked silicon rubber, are in a good agreement with the theory of Sneddon and Sakai. We have a very good agreement between the local properties, measured by nanoindentation, and the bulk properties, measured by DMA.

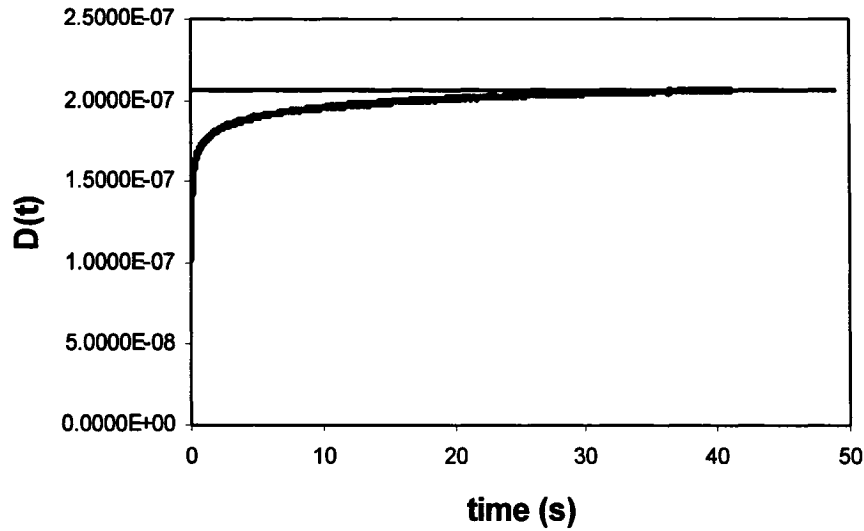


Fig. 6.11 Creep test of indentation of cross-linked silicone rubber with 30 μ n force.

Therefore, one of the basic parameters of viscoelastic materials – the bulk equilibrium modulus was measured by small-force indentation with accuracy of about 2 %. Additionally we were able to measure the retardation time by fitting the Voight model to the $D(t)$ measured from nanoindentation.

Since silicon cross-linked rubber is a highly elastic viscoelastic solid we can determine the retardation time by modeling the behavior with a Voight element (see section 2.5.1), fitting the experimental data to Equation 6.5.

$$D(t) = D_0 + D_i \left[1 - \exp\left(-\frac{(t-t_0)}{\lambda}\right) \right] \quad (6.5)$$

where:

λ – retardation time

D_0 – glassy compliance

$D_0 + D_i = D(\infty)$ – equilibrium compliance

The fitting of the creep compliance curve in Figure 6.9 gives us a retardation time of $\lambda=0.18$ sec.

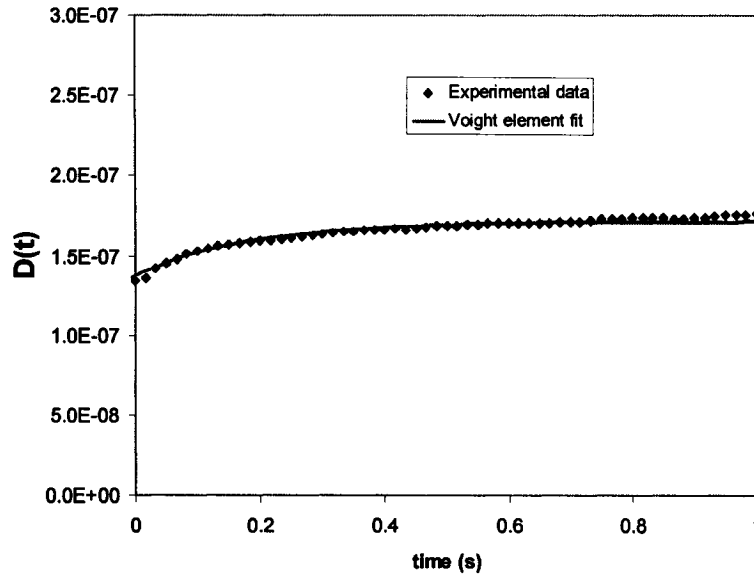


Fig.6.12 Fitting of experimental data with Voigt element model.

We can draw a conclusion that at the current state of its development, the nanoindentation technique can be effectively used to measure properties of viscoelastic solids. As for viscoelastic liquids, there is need for further development in deeper understanding of the physics of the process of nanoindentation and particularly the interaction between the indenter and the surface of a high molecular weight polymer.

CHAPTER 7

Conclusions.

The purpose of this work was to research the possibility to apply nanoindentation as a testing technique in rheometry. We investigated the advantages of nanoindentation as well as its limitations. The research focused on three main directions: physical modeling, numerical simulations and experimental research.

In the course of this work we considered a number of physical models that can be used to describe nanoindentation process and account for viscoelastic properties of a tested material. We formulated a model for indentation of viscoelastic liquids based on the Stoke's potential flow and suggested a combination of this model with that of Sneddon and Sakai for simulating the behavior of viscoelastic liquids.

In numerical modeling we suggested a problem set up for the simulation of a Stoke's potential flow and a two-phase viscous indentation flow with indenters of various shapes by solving Navier-Stokes equations using the FLUENT commercial code. This set up can be a basis for modeling an indentation of viscoelastic liquids.

In the experimental research we investigated a viscoelastic liquid and a viscoelastic solid with conventional rheological methods and with nanoindentation. We compared the bulk properties with the local ones. Special attention was paid to the varying of the local properties for different materials.

The comparison of the theoretical modeling with experimental results showed that bulk properties of viscoelastic solids can be measured by indentation with sufficient accuracy. At the same time, for the nanoindentation of viscoelastic liquids with high

molecular weight, the physical model should be improved by taking account the surface effects and, probably, other physical phenomena.

We can say that this work shows that nanoindentation can be successfully used in rheological studies. It shows that nanoindentation can be successfully used in testing of viscoelastic solids and viscoelastic liquids.

Chapter 8

Contributions.

Nanoindentation is a new state-of-the-art modification of traditional indentation. It utilizes various innovative technologies and engineering solutions and broadens the area of applications of the indentation technique. This work is one of the first attempts to employ nanoindentation for the testing of viscoelastic materials. It includes physical and numerical modeling as well as experimental research.

A theoretical model of nanoindentation is proposed that incorporates Stoke's theory of a creeping flow, Sneddon & Sakai models for the indentation of elastic and viscoelastic solids and the Maxwell viscoelastic model.

Numerical modeling was done for steady-state potential flow with various parameters around indenters of different shapes. The two-phase transient Newtonian flow during indentation was modeled by solving the system of Navier-Stokes equations, using the FLUENT commercial software.

The experimental part of this work included investigation of viscoelastic materials by nanoindentation method as well as traditional rheological techniques, which allows us to compare the bulk and the local properties of the tested materials. We developed and tried nanoindentation testing procedures to determine properties viscoelastic solids and viscoelastic liquids. A constant force nanoindentation was found to be advantageous for the investigation of viscoelastic solids, like cross-linked silicone rubber. It was shown that despite a significant, up to 25%, that the averaging of experimental data allows us accurately measure such parameters as modulus and the main retardation time.

For viscoelastic liquids we propose indentation with a constant rate. It was shown that usual fluid mechanics approach is not always accurate because of a significant impact of the surface effects.

Also we proposed directions for future theoretical research and desirable of software and hardware modifications of the nanoindentation unit.

Chapter 9

Future work.

The future work on the development of the nanoindentation method will be focused on two aspects – theoretical and experimental. The theoretical part includes investigating physical phenomena involved in the nanoindentation (like the surface effect in polymers) and developing physical models of the nanoindentation for the adequate representation of complex motion of the displaced material under investigation and predicting the indentation force.

Prospective physical models that are worthy of additional investigation would be the theory of boundary layers, particularly the Falkner-Scan theory for pyramidal indenters and the Mangler transforms for axisymmetrical indenters of rotational shapes (conical and spherical). Another approach is to simplify the deformation field of tested material by the use of a specially shaped indenter. For example, for the indentation with a flattened plate indenter, as discussed in the Chapter 6, a suitable model is one for the transient motion of a plate in a semi-infinite liquid also obtained by Stokes.

Being designed for testing solid materials, the nanoindentation unit needs to be modified for improved testing of soft viscoelastic materials. We recommend the following improvements to the apparatus in order to improve performance with soft materials:

- improve control of the indentation force.
- increase sensitivity, resolution, speed and reduce noise/signal ratio of the AD converter to be able precisely register small indentation forces and small displacements.

- improve characteristics of the transducer by increasing range of the available forces and displacements.
- design and manufacture new types of indenters – design indenters of various shapes to serve special purposes. One of possible directions would be to minimize the projected area and increase the surface area.
- choose proper material or coating for indenter surface for soft materials like molten polymers since indenter hardness is not any longer the most desirable characteristic. It is more important here to make it hydrophobic to a wide range of viscoelastic liquids. A thin layer of coating can be a good engineering solution.

Many new types of indentation tests could also be developed. A combination of a linear displacement function with the SAOS, or DMA principle is one possibility. We can suggest the following example. It might be useful to measure the elastic properties of viscoelastic liquids with a short relaxation time by combining constant rate indentation with SAOS. The expression for the displacement as a function of time can be as Equation (9.1):

$$x(t) = V \cdot t + A \sin(\omega t) \quad (9.1)$$

The linear component of this function provides a permanent compression component and the deviations from the harmonic part can reveal the elastic properties.

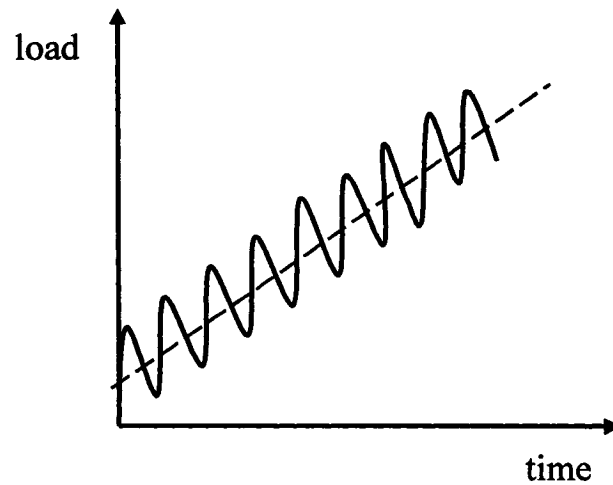


Fig. 9.1 Combined a linear and a harmonic load function.

Such a test can be used to measure a storage modulus of a viscoelastic liquid with a very short relaxation time, which is much shorter than the indentation time.

Another interesting idea is to use the wetting phenomena of the indenter with a tested material. We found that if a tested material wets the indenter very well, the nanoindentation test is practically impossible. As soon as indenter is brought in contact with the tested material, it climbs up and pulls the indenter down by capillary forces. We might make use of this, generally negative phenomenon, to measure elongational flow by using a coated flat end indenter. After being brought in a brief contact with the tested material, the indenter can be brought up, pulling a layer of the polymer with it. This idea is illustrated below.

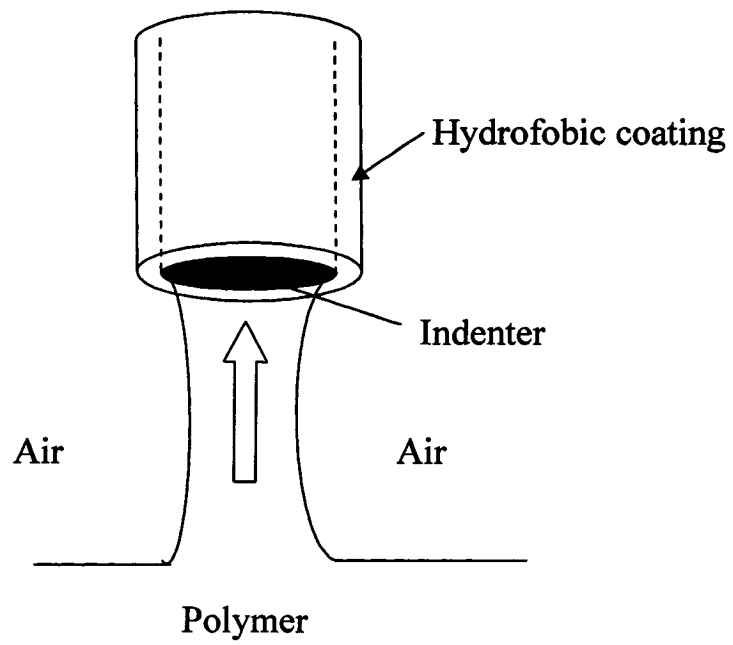


Fig. 9.2 Elongation flow test.

This method can also be used to measure interfacial energy between the material and the indenter.

References.

1. Shimizu, S.; Yanagimoto, T.; Sakai, M.. **Pyramidal indentation load-depth curve of viscoelastic materials.** Journal of Materials Research (1999), 14(10), 4075-4086
2. Sakai, M.; Shimizu, S.. **Elastic, plastic, and viscoelastic contact problems in axisymmetric indentation.** Ceramic Transactions (2002), 133(Improved Ceramics through New Measurements, Processing, and Standards), 105-114
3. (taken Sakai, M.; Shimizu, S.; Miyajima, N.; Tanabe, Y.; Yasuda, E. **Viscoelastic indentation on iodine-treated coal tar pitch.** Carbon (2001), 39(4), 605-614.
4. Sakai, M.; Shimizu, S.. **Indentation rheometry for glass-forming materials.** Journal of Non-Crystalline Solids (2001), 282(2,3), 236-247.
5. Sakai, M. **Time-dependent viscoelastic relation between load and penetration for an axisymmetric indenter.** Department of Materials Science, Philosophical Magazine A: Physics of Condensed Matter: Structure, Defects and Mechanical Properties (2002), 82(10), 1841-1849.
6. Sakai, M.; Shimizu, S. **Elastic, plastic, and viscoelastic contact problems in axisymmetric indentation.** Ceramic Transactions (2002), 133(Improved Ceramics through New Measurements, Processing, and Standards), 105-114.
7. Sneddon, Ian N.. **Symposium on elasticity and viscoelasticity in ceramics. Introductory talk.** Transactions of the British Ceramic Society (1954), 53 697-709.
8. Sneddon, Ian N.. **Special Functions of Mathematical Physics and Chemistry.** (1956), 171 pp.
9. Radok, J. R. M.; Tai, Clement L. **A theory of inclusions in viscoelastic materials.** Journal of Applied Polymer Science (1962), 6 518-28.
10. . Sneddon, Ian Naismith **Progress in solid mechanics V.3.** Amsterdam [Netherlands] : North-Holland Pub. Co. ; New York : Interscience Publishers, 1960-1963.

11. E.H Lee, J.R.Radok, **"The Contact Problem for Viscoelastic bodies,"** Journal of Applied Mechanics, 1960 27(82), 438-444.
12. S.C. Hunter, **The Hertz Problem for a Rigid Spherical Indenter and a Viscoelastic Half-Space,** Journal of the Mechanics and Physics of Solids, 8, 1960 p.219-234.
13. T.C.Ting, **Remarks on Linear Viscoelastic Stress Analysis in Cylinder Problems.** 9th Midwestern conference, Madison, August, 1965.
14. G.A.Graham **The Contact problem in the Linear Theory of Viscoelasticity** International Journal of Engineering Sciences. (3) 1965 27-45.
15. I.N.Sneddon **The Relation Between Load and Penetration in the Axisymmetric Boussinesq Problem for a Punch of Arbitrary Profile** International Journal of Engineering Sciences. (3) 1965 47-57.
16. E.H Lee, T.G. Rogers **Solution of Viscoelastic Stress Analysis Problems Using Measured creep or relaxation functions.** Journal of Applied Mechanics, (30)85, 1963, 127-133.
17. M.E Gurin, E.Stenberg "On the linear theory of viscoelasticity" Archive for Rational Mechanics and Analysis 11(4) 1962, 288-299
18. Cheng, L.; Xia, X.; Yu, W.; Scriven, L. E.; Gerberich, W. W. **Flat-punch indentation of viscoelastic material.** Journal of Polymer Science, Part B: Polymer Physics (2000), 38(1), 10-22.
19. Low, I. M. **Effects of load and time on the hardness of a viscoelastic polymer.** Materials Research Bulletin (1998), 33(12), 1753-1758.
20. Low, I. M.; Paglia, G.; Shi, C. **Indentation responses of viscoelastic materials.** Journal of Applied Polymer Science (1998), 70(12), 2349-2352.
21. Tang, B.; Ngan, A. H. W. **Investigation of viscoelastic properties of amorphous selenium near glass transition using depth-sensing indentation.** Soft Materials (2004), 2(2-3), 125-144.

22. Vanlandingham, M. R.; Chang, N.-K.; Drzal, P. L.; White, C. C.; Chang, S.-H.
Viscoelastic characterization of polymers using instrumented indentation. I. Quasi-static testing. Journal of Polymer Science, Part B: Polymer Physics (2005), 43(14), 1794-1811.
23. White, C. C.; Vanlandingham, M. R.; Drzal, P. L.; Chang, N.-K.; Chang, S.-H.
Viscoelastic characterization of polymers using instrumented indentation. II. Dynamic testing. Journal of Polymer Science, Part B: Polymer Physics (2005), 43(14), 1812-1824.
24. Yang, Shuang; Zhang, Yong-Wei; Zeng, Kaiyang. **Analysis of nanoindentation creep for polymeric materials.** Journal of Applied Physics (2004), 95(7), 3655-3666.
25. Low, I. M.; Shi, C. **Vickers indentation responses of epoxy polymers.** Journal of Materials Science Letters (1998), 17(14), 1181-1183.
26. Cheng, Liangsheng; Scriven, L. E.; Gerberich, William W. **Viscoelastic analysis of micro-and nanoindentation.** Materials Research Society Symposium Proceedings (1998), 522(Fundamentals of Nanoindentation and Nanotribology), 193-198.
27. Lawrence, C. J.; Adams, M. J.; Briscoe, B. J.; Kothari, D. C. **Wedge indentation and stress relaxation of a viscoelastic paste.** World Congress on Particle Technology 3, Brighton, UK, July 6-9, 1998 (1998), 588-598.
28. Shinozaki, D. M.; Lu, Y. **Micro-indentation relaxation measurements in polymer thin films.** Creep and Stress Relaxation in Miniature Structures and Components, Proceedings of a Symposium, Cincinnati, Oct. 8-9, 1996 (1996), 135-149.
29. Yoshioka, Naoto; Yoshioka, Masato. **Dynamic observation of indentation process: a possibility of local temperature rise.** Philosophical Magazine A: Physics of Condensed Matter: Structure, Defects and Mechanical Properties (1996), 74(5), 1273-1286.
30. Kholodilov, O. V. **Method for determining the microhardness of polymer materials.** Zavodskaya Laboratoriya (1989), 55(2), 92-4. CODEN: ZVDLAU ISSN:0321-4265.

31. Klyuev, E. A.; Gorokhovskii, G. A.; Cheberyak, A. G.; Kuznetsov, E. A. **Stressed state in the contact zone of polyurethane with a solid indenter.** Mekhanika Polimerov (1976), (5), 838-44.
32. **Evaluation of the surface referencing technique in depth-sensing indentation of soft materials.** Tang, B.; Ngan, A. H. W. Department of Mechanical Engineering, The University of Hong Kong, Hong Kong, Peop. Rep. China. Soft Materials (2004), 2(2-3), 183-193.
33. Paiva, Adriana; Sheller, Nina; Foster, Mark D.; Crosby, Alfred J.; Shull, Kenneth R. **Study of the Surface Adhesion of Pressure-Sensitive Adhesives by Atomic Force Microscopy and Spherical Indenter Tests.** Macromolecules (2000), 33(5), 1878-1881.
34. Pai, Shih-i **Modern fluid mechanics.** Beijing : Science Press ; New York : Distributed by Van Nostrand Reinhold, 1981.
35. Bird, R.B. Stewart W.E. **Transport phenomena.** New York : J. Wiley, 2002.
36. Eckert E.R.G., Drake R.M. **Analysis of heat and mass transfer** Washington : Hemisphere Pub. Corp., c1987.
37. Schlichting H. **Boundary layer theory. Translated by J.** New York, McGraw-Hill, 1960.
38. D.F. Rogers. **Laminar flow analysis / David F. Rogers** New York : Cambridge University Press, 1992.
39. Morrison, Faith A **Understanding rheology / Faith A. Morrison** New York : Oxford University Press, 2001.
40. Tanner, Roger I **Engineering rheology / Roger I. Tanner** Oxford [Oxfordshire] : Clarendon Press ; New York : Oxford University Press, 1988.

41. Dealy, John M. **Melt rheology and its role in plastics processing : theory and applications** / John M. Dealy and Kurt F. Wissbrun. New York : Van Nostrand Reinhold, c1990.
42. Honerkamp, J & Weese, J, **A Nonlinear regularization Method for the Calculation of Relaxation Spectra**, Rheol. Acta, 1993,32,64-73
43. Web cite of **The International Institute of Synthetic Rubber Producers**.
44. Johnson, K. L. **Contact mechanics** Cambridge; New York : Cambridge University Press, 1985.
45. **Contact mechanics** / edited by M. Raous and M. Jean and J.J. Moreau New York : Plenum Press, 1995.
46. Ainbinders, S.; Loginova, A. Ya. **Contact area of a rigid spherical indenter with the surface of polymer materials at various pressures, temperatures, and contact times**. Mekhanika Polimerov (1971), 7(3), 457-64.
47. Leclere, Ph.; Dubourg, F.; Viville, P.; Cornet, V.; Aime, J. P.; Lazzaroni, R. **Dynamic force microscopy analysis of nanocomposites, polymer blends, and block copolymers: Beyond imaging the surface morphology**. PMSE Preprints (2003), 88 497-498.
48. Dubourg, F.; Kopp-Marsaudon, S.; Leclere, Ph.; Lazzaroni, R.; Aime, J. P. **Experimental determination of the viscosity at the nanometer scale on a block copolymer with an oscillating nano-tip**. European Physical Journal E: Soft Matter (2001), 6(5), 387-397.
49. Dubourg, F.; Aime, J. P.; Marsaudon, S.; Boisgard, R.; Leclere, P. **Probing viscosity of a polymer melt at the nanometre scale with an oscillating nanotip**. European Physical Journal E: Soft Matter (2001), 6(1), 49-55.
50. Dubourg, F.; Aime, J. P. **Role of the adhesion between a nanotip and a soft material in tapping mode AFM**. Surface Science (2000), 466(1-3), 137-143.

51. Kopp-Marsaudon, S.; Leclere, Ph.; Dubourg, F.; Lazzaroni, R.; Aime, J. P. **Quantitative measurement of the mechanical contribution to tapping-mode atomic force microscopy images of soft materials.** *Langmuir* (2000), 16(22), 8432-8437.
52. Boschung, E.; Heuberger, M.; Dietler, G. **Energy dissipation during nanoscale indentation of polymers with an atomic force microscope.** *Applied Physics Letters* (1994), 64(26), 3566-3574.
53. Granick, Steve; Kumar, Sanat K.; Amis, Eric J.; Antonietti, Markus; Balazs, Anna C.; Chakraborty, Arup K.; Grest, Gary S.; Hawker, Craig; Janmey, Paul; Kramer, Edward J.; Nuzzo, Ralph; Russell, Thomas P.; Safinya, Cyrus R. **Macromolecules at surfaces: Research challenges and opportunities from tribology to biology.** *Journal of Polymer Science, Part B: Polymer Physics* (2003), 41(22), 2755-2793.
54. Granick, Steve; Kumar, Sanat K.; Amis, Eric J.; Antonietti, Markus; Balazs, Anna C.; Chakraborty, Arup K.; Grest, Gary S.; Hawker, Craig; Janmey, Paul; Kramer, Edward J.; Nuzzo, Ralph; Russell, Thomas P.; Safinya, Cyrus R. **Macromolecules at surfaces: Research challenges and opportunities from tribology to biology.** *Journal of Polymer Science, Part B: Polymer Physics* (2003), 41(22), 2755-2793.
55. Zhu Yingxi; Granick Steve **Limits of the hydrodynamic no-slip boundary condition.** *Physical review letters* (2002 Mar 11), 88(10).
56. Mukhopadhyay, Ashis; Granick, Steve. **Micro- and nanorheology.** *Current Opinion in Colloid & Interface Science* (2001), 6(5,6), 423-429.
57. A.E.Giannakopoulos, S.Suresh. **Determination of Electroplastic Properties by Instrumented Sharp Indentation.** *Scripta Materialia*, (1999), 40(10), 1191-98.
58. Hu, Hsuan Wei; Granick, Steve. **Viscoelastic dynamics of confined polymer melts.** *Science (Washington, DC, United States)* (1992), 258(5086), 1339-42.
59. Demirel, A. Levent; Cai, Lenore; Dhinojwala, Ali; Granick, Steve; Drake, J. M. **Nanorheology of polymers, block copolymers, and complex fluids.** *Materials*

- Research Society Symposium Proceedings (1995), 366(Dynamics in Small Confining Systems II), 113-22.
60. Dhinojwala, Ali; Granick, Steve. **New approaches to measure interfacial rheology of confined fluids.** Journal of the Chemical Society, Faraday Transactions (1996), 92(4), 619-623.
 61. Guo, Qian; Izumisawa, Satoru; Chen, Haigang; Jhon, Myung S. **Interfacial properties of sub/mono/multi-layer perfluoropolyether nanofilms.** Abstracts of Papers, 230th ACS National Meeting, Washington, DC, United States, Aug. 28-Sept. 1, (2005).
 62. Nukaga, Hideyuki; Fujinami, So; Watabe, Hiroyuki; Nakajima, Ken; Nishi, Toshio. **Nanorheological analysis of polymer surfaces by atomic force microscopy.** Japanese Journal of Applied Physics, Part 1: Regular Papers, Brief Communications & Review Papers (2005), 44(7B), 5425-5429.
 63. Moon, Seung-ho; Swearingen, Stephanie; Foster, Mark D. **Near surface nanomechanical and nanorheological behavior of PSAs measured using scanning probe microscopy.** Proceedings of the Annual Meeting of the Adhesion Society (2003), 26th 301-303.
 64. Restagno, F.; Crassous, J.; Charlaix, E.; Monchanin, M. **A new capacitive sensor for displacement measurement in a surface force apparatus.** Los Alamos National Laboratory, Preprint Archive, Condensed Matter (2001), 1-18.
 65. Liu, Shufen. **Solid silicone rubber.** Faming Zhuanli Shenqing Gongkai Shuomingshu (2003), 10 pp.
 66. Liu, Shufen. **Solid silicone rubber.** Faming Zhuanli Shenqing Gongkai Shuomingshu (2003), 10 pp.
 67. Chiu, Hsien-Tang; Chiu, Shih-Hsuan; Wu, Jyh-Horng. **Study on mechanical properties and intermolecular interaction of silicone rubber/polyurethane/epoxy blends.** Journal of Applied Polymer Science (2003), 89(4), 959-970.

68. Verolainen, N. V.; Kareyeva, V. M.; Voronchikhina, L. I. **Preparing of high-filled composites in the presence of surfactants.** *Izvestiya Vysshikh Uchebnykh Zavedenii, Khimiya i Khimicheskaya Tekhnologiya* (2003), 46(7), 90-92.
69. Allal, Ahmed; Lamaison, Sandrine; Leonardi, Frederic; Marin, Gerard. **From the microstructure of polymers to their rheological properties.** *Comptes Rendus Physique* (2002), 3(10), 1451-1458.
70. Cho, Kwang Soo; Ahn, Kyung Hyun; Lee, Seung Jong. **Universality of linear viscoelasticity of monodisperse linear polymers.** *Journal of Polymer Science, Part B: Polymer Physics* (2004), 42(14), 2730-2737.
71. Isono, Yoshinobu; Kamohara, Toshihiro; Takano, Atsushi; Kase, Toshio. **Nonlinear viscoelastic properties and change in entanglement structure of linear polymer. Part 1. Single-step large shearing deformations.** *Rheologica Acta* (1997), 36(3), 245-251.
72. Martter, T. D.; Foster, M. D.; Lizarraga, G.; Xu, S.; Yoo, T.; Quirk, R. P.; Butler, P.; Majkrzak, C. F. **Surface and bulk studies in blends of star and linear polybutadiene.** *Polymeric Materials Science and Engineering* (2001), 84 694-695.
73. Malkin, A. Ya.; Blinova, N. K.; Vinogradov, G. V.; Zabugina, M. P.; Sabsai, O. Yu; Shalganova, V. C.; Kirchevskaya, I. Yu; Shatalov, V. P. **Rheological properties of polydisperse polymers.** *European Polymer Journal* (1974), 10(5), 445-51.
74. Sapozhnikov, I. M.; Pavlov, N. G.; Grechanovskii, V. A.; Vinogradov, G. V.; Malkin, A. Ya. **Viscous properties of solutions of polybutadienes with different polydispersity.** *Vysokomolekulyarnye Soedineniya, Seriya B: Kratkie Soobshcheniya* (1972), 14(3), 219-23.
75. Slattery, J.C. **Non-newtonian flow about a sphere.** Ph. D. Dissertation, University of Wisconsin (1959).
76. **Rheometer MCR – 500 Instruction Manual, Paar Physice Co.**
77. **Hysitron Triboscope – User Manual, Hysitron Inc.**